ELECTROMAGNETIC ION-CYCLOTRON WAVES OCCURRENCE ON THE VAN ALLEN RADIATION BELTS USING THE VAN ALLEN PROBES MISSION DATASET

Claudia Medeiros

Doctorate Thesis of the Graduate Course in Space Geophysics, guided by Drs. Luis Eduardo Antunes Vieira, Vitor Moura Cardoso e Silva Souza, and David Gary Sibeck, approved in March 20, 2020.

INPE

São José dos Campos

2020

ELECTROMAGNETIC ION-CYCLOTRON WAVES OCCURRENCE ON THE VAN ALLEN RADIATION BELTS USING THE VAN ALLEN PROBES MISSION DATASET

Claudia Medeiros

Doctorate Thesis of the Graduate Course in Space Geophysics, guided by Drs. Luis Eduardo Antunes Vieira, Vitor Moura Cardoso e Silva Souza, and David Gary Sibeck, approved in March 20, 2020.

INPE

São José dos Campos

2020

Aluno (a): **Cláudia Medeiros**

Título: "ELECTROMAGNETIC ION-CYCLOTRON WAVES OCCURRENCE ON THE VAN ALLEN RADIATION BELTS USING THE VAN ALLEN PROBES MISSION DATASET"

Aprovado (a) pela Banca Examinadora em cumprimento ao requisito exigido para obtenção do Título de **Doutor(a)** em

Geofísica Espacial/Ciências do Ambiente Solar-Terrestre

Dra. Lívia Ribeiro Alves

_____
Presidente / INPE / São José dos Campos - SP

(X) *Participação por Vídeo - Conferência*

(X) Aprovado   ( ) Reprovado

Dr. Luis Eduardo Antunes Vieira

_____
Orientador(a) / INPE / São José dos Campos - SP

(X) *Participação por Vídeo - Conferência*

(X) Aprovado   ( ) Reprovado

Dr. Vitor Moura Cardoso e Silva Souza

_____
Orientador(a) / INPE / São José dos Campos - SP

(X) *Participação por Vídeo - Conferência*

(X) Aprovado   ( ) Reprovado

Dr. David Gary Sibeck

_____
Orientador(a) / NASA / Washington, D.C. - USA

(X) *Participação por Vídeo - Conferência*

(X) Aprovado   ( ) Reprovado

Dra. Inez Staciarini Batista

_____
Membro da Banca / INPE / SJCampos - SP

(X) *Participação por Vídeo - Conferência*

(X) Aprovado   ( ) Reprovado

Este trabalho foi aprovado por:

( ) *maioria simples*

(X) *unanimidade*

São José dos Campos, 20 de março de 2020

Aprovado (a) pela Banca Examinadora em cumprimento ao requisito exigido para obtenção do Título de *Doutor(a)* em

Geofísica Espacial/Ciências do Ambiente Solar-Terrestre

Dr. Jean Carlo Santos

_____

Convidado(a) / UTFPR / Curitiba - PR

(X) Participação por Vídeo - Conferência

(X) Aprovado ( ) Reprovado

Dra. Flávia Reis Cardoso Rojas

_____

Convidado(a) / EEL - USP / Lorena - SP

(X) Participação por Vídeo - Conferência

(X) Aprovado ( ) Reprovado

Este trabalho foi aprovado por:

( ) maioria simples

(X) unanimidade

São José dos Campos, 20 de março de 2020

*"God, grant me the **serenity** to accept the things I cannot change, the **courage** to change the things I can, and the **wisdom** to know the difference. Just for today!"*.

*"Concedei-me Senhor, a **serenidade** para aceitar as coisas que não posso modificar, **coragem** para modificar aquelas que posso e **sabedoria** para distiguir umas das outras. Só por hoje!"*.

UNKNOWN AUTHOR
as *" Serenity prayer (Oração da Serenidade)"*

A meu filho amado **Luís Guilherme Medeiros de Farias** *e a meus pais* **Celina Barbara de Miranda** *e* **José Medeiros Filho(in memoriam)**

ACKNOWLEDGEMENTS

É com humildade que entrego esse trabalho inicial de uma jovem cientista. Agradeço a Deus, na forma que eu o concebo, por existir e por permitir viver tudo isso.

A possibilidade de realizar esse trabalho em si me faz a pessoa mais grata desse mundo. Mesmo com todas as dificuldades que a carreira na área científica provê e com algumas limitações inerentes do contexto social que vivo, me sinto privilegiada por estar aqui.

Agradeço ao Instituto Nacional de Pesquisas Espaciais e à Coordenação de Aperfeiçoamento de Pessoal de Nível Superior(CAPES) por fornecer o ambiente e o apoio financeiro para que eu desenvolvesse estudo aqui apresentado. Agradeço também a National National Aeronautics and Space Administration (Nasa/GSFC) e a The Catholic University pelo suporte logístico e financeiro durante o doutorado sanduíche. Estendo o agradecimento à coordenação do centro de controle rastreio pelo apoio institucional.

Nessa jornada que me levou aos Cinturões de Radiação, as portas jamais se abririam se não fosse o profissionalismo e empenho do Dr. Alisson Dal Lago que não mediu esforços para me incluir nesse novo grupo. Assim nasceu essa parceria de trabalho com o "Radiation Belt Group" onde aprendi a amar ir para o INPE e passar horas em frente ao computador extraindo dados e contribuindo de alguma forma minúscula para a ciência. Lígia, Lívia, Paulo, Marchezi, Grazi, Dr. Marlos, Dra. Virgínia, Dr. Odim, a Filomena da secretaria e as mocinhas da limpeza entre outros colegas que estiveram junto dessa turma e são sem dúvida nenhuma, parceiros agradáveis de viagem e, espero eu, de vida. E dessa forma, o Dr. Luis Eduardo Antunes Vieira e se faz admiravelmente meu orientador. muito assertivo e dono de uma inteligência admirável, sonhador inveterado, construindo um projeto de vida e me ajudando a conquistar o meu proprio projeto pessoal. Abriu as portas para minha estadia na NASA entre tantas outras oportunidades que essa porta me abriu. Assim como conhecer o Dr. David Sibeck, com suas camisas festivas e seu olhar alegre, seu perfil indescritível, seu conhecimento que ultrapassa as paredes da ciência e seu carisma inigualável.

E esses dois orientadores ainda me deram mais um co-orientador surpreendente, o Dr. Vitor Souza. Não tenho palavras (e sei que não preciso tê-las) para agradecer meu matraqueado orientador Vitor que se tornou meu grande amigo. De alguma forma a vida colocou essa alma no meu caminho que fez o fardo ficar mais brando,

de viver, são tudo que realmente importa e que faz unir as gerações, faz construir história e fez eu ser uma boa parte de quem eu sou hoje. Minha amada mãe Celina e meu amado filho Luís Guilherme. Amo vocês além do que esse simples agradecimento pode demostrar. Pra vocês só tenho amor.

ABSTRACT

Energetic charged particles trapped in Earth's magnetic field lines constitute the so-called Van Allen radiation belts. The inner most radiation belt is more stable, whereas the outer radiation belt is more dynamic. Plasma waves can propagate either along or across geomagnetic field lines and they can interact with charged particles thereby changing the radiation belt configuration. Among such waves the electromagnetic ion cyclotron (EMIC) waves, are of special interest in this work, since they are responsible for pitch angle-scattering relativistic electrons into the loss cone. Both pitch angle-resolved electron fluxes data and high time-resolution magnetic field measurements acquired from the twin, identically instrumented NASA's Van Allen Probes mission are used here, and they span a time interval of more than 4 years. The focus is to investigate the spatial distribution and the occurrence rate of EMIC waves in the outer Van Allen radiation belt during this period as well as the possible role played by EMIC waves in the reconfiguration of an electron butterfly pitch angle distribution (PAD) shape that resulted in an unusual electron butterfly PAD shape. A case study (MEDEIROS et al., 2019) revealed the likely association between EMIC waves occurrence and such unusual electron butterfly PAD. Then, two machine learning-based techniques have been employed with the first of them, referred to as Bag-of-Features (BoF, Medeiros et al. (2020)), being responsible to find, in a semi-automated way, EMIC wave events in a 4-year span dataset of magnetic field spectrogram images, and the second algorithm, known as Self Organizing Map (SOM, Souza et al. (2016)), would find unusual electron butterfly PAD shapes.By matching both the EMIC waves and the unusual electron butterfly PAD shape surveys the following conclusions are found: (1°) the BoF technique performed nearly as good as the visual classification method with the enormous advantage that the BoF technique greatly expedites the analysis by accomplishing the task in just a few minutes; (2°) for the period of one full Van Allen Probes' orbit precession the unusual electron butterfly PAD shape found by Medeiros et al. (2019) is indeed unusual when considering events wherein there is at least a 10 minutes persistence. These events correspond to only 0.3% of the whole 1.8 MeV energy electron PADs dataset used for the same interval; (3°) persistent unusual electron butterfly PAD events generally occur throughout the nightside region, at L-shell locations larger than about $5\,R_E$, with a slightly higher occurrence rate in the 01:00–02:00 MLT range; (4°) visual inspection of a small subset, that is, 23 events, containing persistent unusual electron butterfly PAD shapes show that they are indeed associated with EMIC waves occurrence for 22 events; (5°) it is argued that EMIC waves can be the dominant factor in the relativistic electron flux reduction at pitch angles $< 45°$ and $> 135°$ which in turn lead to the appearance of such unusual electron butterfly PAD shapes.

Keywords: Earth's magnetosphere. Van Allen radiation belts. Van Allen probes mission. Electromagnetic Ion-Cyclotron waves. neural networks.

ESTUDO DA OCORRÊNCIA E DA DISTRIBUIÇÃO ESPACIAL DAS ONDAS ELETROMAGNÉTICAS ÍON-CICLOTRÔNICAS NO CINTURÃO DE RADIAÇÃO EXTERNO UTILIZANDO DADOS DA MISSÃO VAN ALLEN PROBES

RESUMO

Ondas de plasma podem se propagar ao longo ou através das linhas de campo geomagnético e podem interagir com partículas carregadas, alterando assim a configuração do cinturão de radiação Van Allen. Entre essas ondas, existem as ondas eletromagnéticas ion-ciclotrônicas (EMIC) que são de especial interesse neste trabalho, uma vez que são responsáveis pelo espalhamento de elétrons relativísticos no cone de perda. Para tal são utilizados dados de fluxos de elétrons resolvidos por ângulo de inclinação e medições de campo magnético de alta resolução adquiridas da missão Van Allen Probes da NASA. O foco é investigar a distribuição espacial e a taxa de ocorrência de ondas EMIC no cinturão de radiação Van Allen externo, bem como o possível papel desempenhado pelas ondas EMIC na reconfiguração da distribuição do angulo de arremesso para um formato incomum de borboleta. (MEDEIROS et al., 2019) revelou a provável associação entre a ocorrência de ondas EMIC e a reconfiguração incomum da distribuição do angulo de arremesso em formato borboleta. Duas técnicas baseadas em aprendizado de máquina foram empregadas com a primeira, denominada Bag of Features (BoF, Medeiros et al. (2020)), para encontrar, de maneira semi-automática, os eventos com ondas EMIC em um conjunto de dados de quatro anos de imagens de espectrograma de campo magnético, e o segundo algoritmo, conhecido como Mapa Auto Organizável (SOM, Souza et al. (2016)), aplicado a uma porção menor do conjunto de dados para encontrar formas incomuns de distribuição do angulo de arremesso. Ao combinar as ondas EMIC e as distribuições tipo borboleta, obteve-se as seguintes conclusões: (1°) a técnica BoF teve desempenho quase tão bom quanto o método de classificação visual, com a enorme vantagem de que a técnica BoF agiliza muito o análise realizando a tarefa em apenas alguns minutos; (2°) pelo período de uma precessão total da órbita de Van Allen Probes, a forma incomum de PAD de borboleta encontrada por Medeiros et al. (2019) é realmente incomum ao considerar eventos em que há pelo menos 10 minutos de persistência. Esses eventos correspondem a apenas 0,3 % de todo o conjunto de dados de PADs de elétrons com energia de 1,8 MeV para o mesmo intervalo; (3°) os eventos PAD incomuns e persistentes tipo borboleta ocorrem geralmente em toda a região noturna, em locais $L-shell$ maiores que cerca de 5 R_E, com uma taxa de ocorrência um pouco maior no período de 01-02 MLT; (4°) A inspeção visual de um pequeno subconjunto, ou seja, 23 eventos, contendo formas PAD incomuns e persistentes de borboleta mostra que elas estão realmente associadas à ocorrência de ondas EMIC em 22 eventos; (5°) argumenta-se que as ondas EMIC podem ser o fator dominante na redução do fluxo de elétrons relativísticos com ângulos de arremesso $< 45°$ e $> 135°$, que por sua vez levam ao aparecimento de tais formas de PAD de borboleta.

Palavras-chave: Magnetosfera terrestre. Cinturão de radiação Van Allen. Missão Van Allen Probes. Ondas Eletromagnéticas Íon-ciclotrônicas. Redes neurais.

LIST OF FIGURES

LIST OF TABLES

LIST OF ABBREVIATIONS

AC	–	After Christ
BATS-R-US	–	Block-Adaptive-Tree Solar-wind Roe-type Upwind-Scheme
BC	–	Before Christ
BoF	–	Bag-of-Features
CCMC	–	Community Coordinated Modeling Center
CDF	–	Common Data Format
CIR	–	Corotating Interaction Regions
CME	–	Coronal Mass Ejection
Dst	–	Geomagnetic index
ECH	–	Electrostatic Electron Cyclotron Harmonic
ECT	–	Energetic Particle Composition and Thermal Plasma Suites
ELF	–	Extremely Very Low Frequency
EMIC	–	Electromagnetic Ion Cyclotron
eV	–	eletron-Volt
FEDU	–	Unidirectional Differential Electron Flux
GSM	–	Geocentric Solar Magnetospheric
Hz	–	Hertz
iCME	–	Interplanetary Coronal Mass Ejection
IMF	–	Interplanetary Magnetic Field
LANL	–	Los Alamos National Laboratory
MAG	–	Fluxgate Magnetometer instrument
MagEIS	–	Magnetic ElectronIon Spectrometer instrument
MFA	–	Magnetic field-aligned coordinate system
MHD	–	Magnetohydrodynamic
MLaT	–	Magnetic Latitude
MLT	–	Magnetic Local Time
MSC	–	Tri-axial Magnetic Search Coil magnetometer instrument
PAD	–	Pitch Angle Distribution
PSD	–	Power Spectral Density
NOEMIC	–	Class name
RBSP-A	–	Radiation Belt Storm Probe A
RBSP-B	–	Radiation Belt Storm Probe B
RCM	–	Rice Convection Model
Re	–	Earth radii
REPT	–	Relativistic Electron-Proton Telescope instrument
RGB	–	Reg, Green, Blue colors
SOC	–	Science Operation Center
SOM	–	Self-Organizing Map
SSC	–	Storm Sudden Commencement
STFT	–	Short-Time Fourier Transform

SURF	–	Speeded-Up Robust Features
SWMF	–	Space Weather Modeling Framew ork
ULF	–	Ultra Low Frequency
UT	–	Universal Time
VLF	–	Very Low Frequency

CONTENTS

1 INTRODUCTION

1.1 Motivation

Earth's Van Allen radiation belts are composed by energetic charged particles trapped in the geomagnetic field lines and the processes of transport, acceleration and loss of these particles have been one of the major topics for Space Weather studies. Such energetic particles originated either from cosmic rays or from our Sun can ultimately affect human lifestyle. Nowadays our society is highly dependent on space-based technologies, particularly for communication and navigation systems, thus it is crucial to perform a continuous monitoring of the energetic particle flux in the near Earth environment and more importantly to shed light on the understanding of the physical processes governing the variability of these particle fluxes. *In situ* satellite measurements, specially those from NASA's Van Allen Probes mission, have been providing us enormous amounts of data that allow us to infer the radiation belt dynamics, and in this way this thesis was born: to build analysis tools to contribute in the understanding of the dynamics of relativistic electrons in the Earth's outer radiation belt during the Van Allen Probes era.

Focused on this, it is well known the existence, within the radiation belts, of electromagnetic ion cyclotron (EMIC) waves which are usually generated by ion temperature anisotropies in the ring current. During EMIC waves propagation, they can interact resonantly with particles, particularly with electrons at relativistic energies promoting pitch angle scattering into the loss cone. NASA's Van Allen Probes mission have been measuring particle fluxes and electromagnetic fields in the Earth's Van Allen radiation belts for about 7 years and numerous discoveries have been made and many more await to be found.

The main proposal of this thesis is to investigate EMIC waves occurrence and its spatial distribution in the outer Van Allen radiation belt using magnetic field measurements from the Van Allen Probes mission. It is also analyzed whether or not EMIC waves occurrence is associated with a peculiar electron pitch angle distribution shape recently reported in the literature (MEDEIROS et al., 2019). An outgrowth of this study is the development of a routine that uses a machine learning-based approach to filter the 4-year span dataset in order to find, in a semi-automated way, EMIC wave signatures in spectrogram images (MEDEIROS et al., 2020). This routine was essential to provide us the spatial distribution of EMIC waves which allowed us to infer their impact on the energetic particle flux distribution in the outer Van Allen radiation belt.

1.2 Outline

Chapter 2 presents a historical review from the discovery of magnetospheric phenomena, and the following steps in the direction of the space era in the hope of contextualizing the reader. The next Chapter 3 introduce the Van Allen radiation belts and the major components involved in the dynamical processes that govern the particle flux varibility within it. The dataset description is presented in Chapter 4. Chapter 5 shows a review of the findings of Medeiros et al. (2019) which drives the main ideia of this thesis: the likely association between EMIC waves occurence and an unusual (or peculiar) pitch angle distribution shape for electrons at relativistic energies. Additionally, Chapter 6 presents the results of a submitted paper (MEDEIROS et al., 2020) which introduces a machine learning-based approach, referred to as Bag-of-Features, that has been employed to perform a semi-automated survey of EMIC waves signatures in a large dataset of magnetic field spectrogram images spanning the time interval from September 2012 to December 2016. On Chapter 7 it is described the usage of another machine learning-based technique known as Self Organized Map (SOM) to find, during one Van Allen Probes' orbit precession from January 2014 to October 2015, the unusual (or peculiar) electron butterfly pitch angle distributions similar to those reported by Medeiros et al. (2019). Conclusions are shown in Chapter 8.

2 OVERVIEW OF SOLAR WIND AND MAGNETOSPHERE COUPLING

The most interesting magnet on Earth is the Earth itself. The electric charges located in its core continuously gyrating produce a magnetic field, similar to a dipole, intrinsic to the planet. This study was born in an attempt to understand the physical processes that rely on the Earth's magnetic field. Several actors contributed to the knowledge that precedes this work (KAMIDE; CHIAN, 2007). This section intends to briefly give us a clue for the historical elements that inspired me on this trip.

Nowadays it is well known the existence of a dipole-like geomagnetic field that anyone with a compass can measure it. The needle tends to align with the magnetic field lines pointing to the magnetic field's north pole.

This knowledge was not acquired overnight, but instead it started a long time ago. The first evidence appeared in records dated from 500 BC showing the magnetite, a natural magnet. Around the year 1000 AC, the Chinese found that if they placed magnetite or a piece of magnetized iron floating in a bowl of water, this material would always line up in the north-south (geographic) direction. Thus arose the first magnetic compass which was widely spread as a supporting material for navigation when it was not possible to be guided by the coast or by the stars. Also through the navigation, letters reported by Christopher Columbus in 1498 described the compass variation from west to east when he reached the Haiti island. Years later in 1581, Robert Normam announced the magnetic pole inclination discovery (KAMIDE; CHIAN, 2007).

However, the first conception of the Earth's magnetic field was presented by William Gilbert in 1600 AC in one of his books named "De Magnete". At that time it was believed that the Earth's magnetic field extended from the Earth to infinity. The concept of the solar wind, as we know today, and how it shapes Earth's magnetic field was introduced only in 1958 by Eugene N. Parker.

A few decades later the concept of the Earth's magnetic field was referred to as Geomagnetism by Edmond Halley who sailed across the Atlantic Ocean mapping the magnetic field direction and creating the first geomagnetic contour map. Spurred by Halley's studies, George Graham first suggested that this compass-measured geomagnetic field exhibits diurnal strength fluctuations. Nevertheless, in the 18th century, technological improvement allowed the confirmation of these phenomena (Anders Celsius in 1740) and their association with the auroras observed by him

and his student Olof Petrus Hiorter.

At the same time, several studies from the space environment were being developed and they made it possible to establish a relationship between them. Observation of the Sun using a telescope by Galileo Galilei in 1610 reported the existence of sunspots and their rotation, which subsequently enabled the discovery of the first evidence of the solar cycle by Heinrich Schwabe in 1843. These studies were published in 1851 by Von Humboldt who proposed the construction of a network of magnetometers capable of measuring changes in the magnetic field and auroral phenomena (KAMIDE; CHIAN, 2007).

Carl Friedrich Gauss concurrently developed a mathematical description of the geomagnetic field and made it possible to build a network of simultaneous measurements of that field. From observations, it was found that variations in the magnetic field and its intensity were somehow related to the sunspot cycle, as studied by Edward Sabine in 1852, and the 27-day cycle linked to the rotation of the Sun by Edward Maunder in 1892.

Great advances happened in the 19th century. The electricity and magnetism studies were the protagonists. Hans Christian Oersted observed that the variation in the electric current caused a change in the behavior of the compass and that somehow electricity and magnetism had a mutual influence. This connection was then studied by Andre-Marie Ampere (Ampere's Law), and at the same time by Michael Faraday (Faraday's Law of Induction) who through experiments showed that electric currents varying in time induce magnetic fields and vice versa. In 1864, the concept of electric and magnetic field lines arose, which were then equalized by James Clerk Maxwell who described the relationship between these fields and presented light as an electromagnetic wave.

The electromagnetic waves concept allowed the analysis of the sunlight through its spectrum. The spectroscopy was implemented by George Ellery Hale in 1892. From the beginning of the use of radio waves to study the solar-terrestrial environment, great discoveries were made. The atmospheric layer containing charged particles in a plasma state referred to as the ionosphere (Robert Alexander Watson-Watt and Edward Appleton, 1926) was among such discoveries. By remote-sensing this conductive layer with electromagnetic waves, it was possible to measure its height, and later on to detect substructures within this layer.

In 1923, Irving Langmuir introduced the concept of "plasma". In 1930, Sidney Chap-

man and Vincent Ferraro developed the first geomagnetic storm model. The plasma streaming and comets observations indicated that there should be some material between the Sun and the geomagnetic field, but only with the beginning of the space erain 1957 some of these discoveries began to be properly explained (KAMIDE; CHIAN, 2007).

In 1959, Thomas Gold proposed the formation of the geomagnetic cavity, nowadays known as the magnetosphere. Kristian Birkeland proposed the existence of the polar magnetic storm and associated its occurrence with auroras. Birkeland and Frederick Lindermann, in 1916-1919, also predicted the existence of the solar wind. But, it was better explained by Eugene Parker only in 1958 through the concept of expansion of the solar atmosphere. The solar wind was measured in 1959 by the Luna I spacecraft and by Explorer 10 in 1961, reported by H. Bridge and B. Rossi, respectively.

The space era started in 1957 with the launch of Sputnik satellites 1 and 2 which were fundamental to consolidate the predicted theories and also to present a new context of the space weather. The Explorer 1 and 3 satellites first discovered the existence of the internal radiation belt which was later called the Inner Van Allen radiation belt in honor of James Van Allen.

The idea of charged particles trapped in a magnetic field was first observed by Kristian Bikerland in 1895. He observed the behavior of an electron beam in a vacuum chamber when close to the magnetic poles. The motion was better understood when Frances Henri Poincaré solved the motion equation for a charged particle that spirals around magnetic field lines and is repelled in regions where the magnetic field is most intense. Even with the dedication of scientists and the mathematician Carl Stoermer, everything led them to believe that due to this, the particles would remain trapped in this motion forever. At that time, these motions were not yet possible to be observed, but it was the key point to understand what we now know as radiation belts. Only in 1957, Siegfried Fred Singer proposed the existence of energetic particles trapped in orbits after their injection during magnetic storms, which seemed to explain the creation of particles with such energy. The big surprise was the permanent existence of these radiation belts, known as the Van Allen Radiation Belts, even in periods without magnetic storms.

Radiation belts can be created artificially and it was first suggested and tested by Nicholas Christofilos using an atomic bomb that was launched into the atmosphere near Ecuador and created a temporary radiation belt whose energetic particles remained trapped for weeks. Part of them subsequently precipitated in the form of an

aurora in that region close to the island of Azores, where auroras are not observed. The Explorer 4 probe was developed by the Van Allen group in order to study this artificial phenomenon. What entrapped particle theory involves will be discussed in Chapter 3.

2.1 Solar environment

Before that, we need to talk about the near-Earth space environment. It all started with the concept of plasma proposed by Irving Langmuir in 1927 to define an ionized gas . The heating of matter alters its thermal kinetic energy in order to alter its state. Once the molecule is in a gaseous state and further energy is supplied to promote the dissociation of electrons from the nucleus an ionized gas or plasma is obtained with an approximate equal number of positively and negatively charged particles. Most of the known universe is in the plasma state. Our very star the Sun is a "ball" of plasma. Charged particles trapped in the Earth's magnetic field and the ionosphere itself are environments where plasma is dominant. The Earth's magnetosphere and the interplanetary medium between Earth and the Sun are our study environments.

The Sun itself has no solid surface. The nuclear reactions that occur deep within it keep the solar plasma heated. Due to its properties, the Sun can be divided into basically three layers: photosphere, the chromosphere and the solar corona. The Sun is continuously emitting plasma from its corona to the entire interplanetary medium. This plasma is known as the solar wind and expands to the limits of the Heliosphere (the region where the solar magnetic field predominates). This solar wind is responsible for compressing and shaping the Earth's magnetosphere and continuously interacts with it. In the next sections I will briefly describe the solar wind, its interaction with the magnetosphere and the Van Allen radiation belts region, since.

2.1.1 Solar wind

The solar wind, name attributed by Parker (1958), is the result of an outward expansion of the solar atmosphere, forming a super-alfvénic flow of ionized plasma carrying a residual solar magnetic field that permeates the interplanetary medium (KIVEL-SON et al., 1995). Due to its high conductivity, part of the solar magnetic field is frozen into the solar wind plasma and it is convectively transported out into the interplanetary medium.

The solar wind consists mainly of protons and electrons plus small concentrations

of ionized helium and heavy ions (KAMIDE; CHIAN, 2007). The solar wind can vary between calm and fast. The average speed of the solar wind can vary from 300 to 1000 km/s, carrying particles at a density from 1 to 50 cm^3 and an interplanetary magnetic field (IMF) intensity of about 3 to 30 nT.

Variations in solar activity strongly affect the solar wind, starting with the sun's own rotation that "contorts" the magnetic field lines in an Archimedean spiral, known as the Parker spiral. Figure 2.1 illustrates the spread of the solar wind and the Archimedean spiral formed. The behavior of the solar wind, due to the rotation period of approximately 27 days, is recurrent. However, the solar wind also changes due to the occurrence of coronal mass ejections (CME) and solar flares (Figure 2.2). The fast solar wind is generated in the coronal holes. They are frequent in periods of maximum solar cycle. The solar wind starts in regions close to the heliospheric current sheet at the heliomagnetic equator. When a faster solar wind flow "catchs up" a slower solar wind flow, which usually happens at a certain distance from the Sun, an interaction region develops. Since these structures rotate with the Sun, they are known as corotating interaction regions or CIR's.

Figure 2.1 - The interplanetary magnetic field.
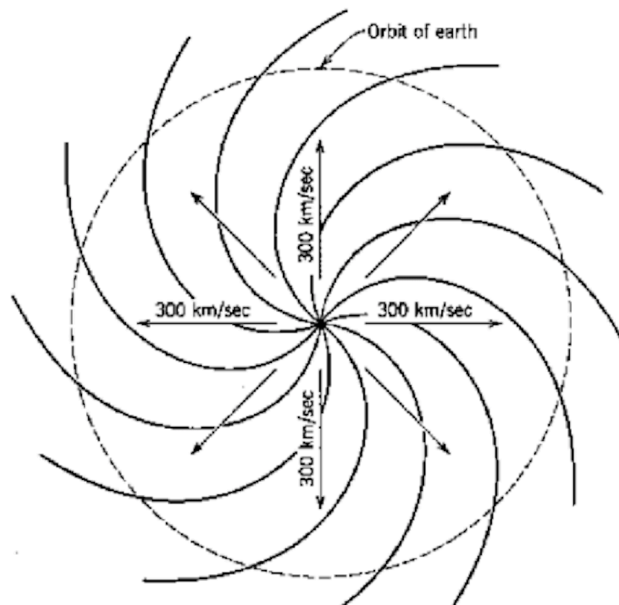
Parker Solar Spiral
SOURCE: Parker (1958).

Figure 2.2 - Slow and Fast Solar Wind.
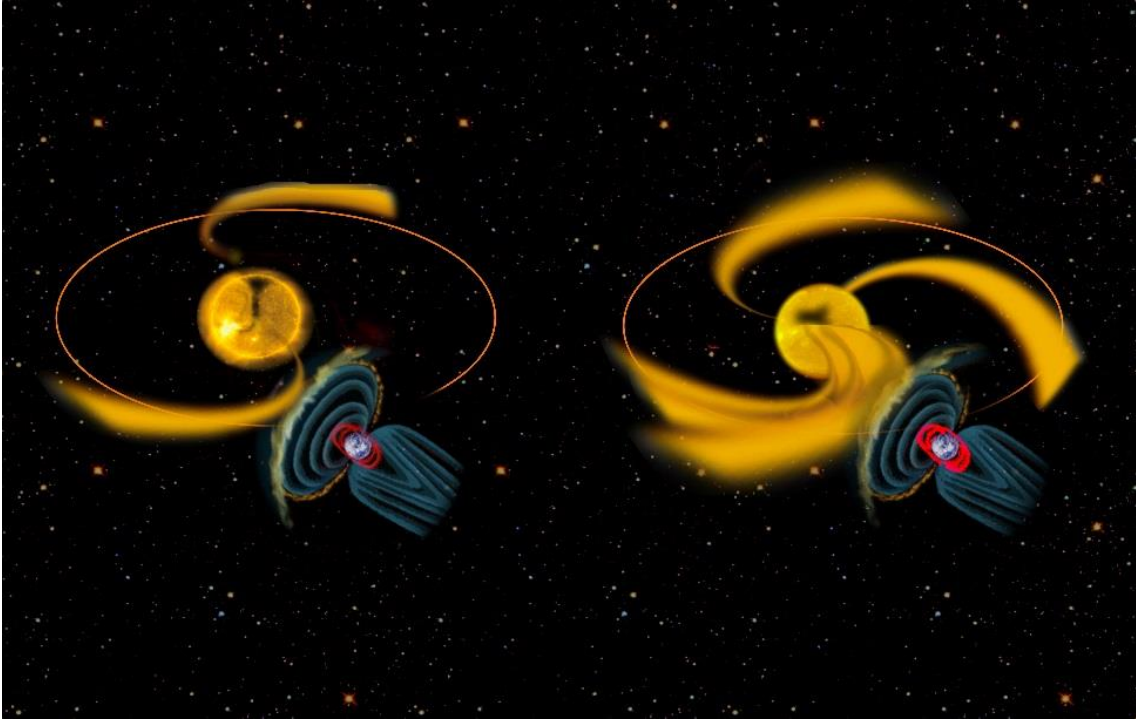
Artist's rendition of both the slow (left) and fast (right) solar wind
SOURCE: Gibson et al. (2009).

In regions farther out from the solar system, the solar wind is slowed by the supersonic interstellar wind and a shock wave is formed. This region is known as the solar wind termination shock. Between this region and the heliopause, there is the heliosphere sheath. The heliopause separates the heliosphere from the interstellar medium. Before reaching the interstellar medium, the solar wind interacts with celestial bodies which may or may not have an intrinsic magnetic field. In the case of Earth, the solar wind is decelerated and deflected around the Earth's magnetic field, forming a cavity called the magnetosphere. The next section describes the Earth's magnetosphere in more details.

2.2 The earth's magnetosphere

The magnetosphere is a region of space in which the Earth's geomagnetic field is confined by the solar wind. The Earth's magnetic field is mainly generated by the currents in the Earth's core and it is quite similar to a magnetic dipole. The Earth's dipole axis is displaced from the Earth's geographic axis of rotation by

approximately 11°. The Earth's magnetic field is responsible for slowing down the solar wind that comes towards Earth. As the solar wind moves with super-alfvénic speeds, a collisionless shock front, namely, the bow shock, is formed in front of the Earth and it helps to deviate the incoming solar wind flow from the magnetospheric obstacle. Downstream of the bow shock the solar wind plasma is decelerated to sub-alfvénic speeds. Due to this interaction, a substantial fraction of solar wind kinetic energy is converted into thermal energy. This heated, turbulent solar wind flow populates the so-called magnetosheath region and it continues its journey towards Earth when it finally reaches the Earth's magnetopause boundary, which is a current sheet separating the colder (a few hundreds of electron-Volt - eV - energy) and denser (~ 20 cm^{-3}) plasma of the magnetosheath from the relatively hotter (a few keV) and tenuous (~ 0.2 cm^{-3}) plasma from magnetospheric origin.

The magnetosphere is oriented by the direction of the solar wind. On the dayside the Earth's magnetic field is compressed by the solar wind, therefore reaching intensities that are usually higher than that of a pure dipole-like field. On the opposite side, named nightside region, the Earth's magnetic field is stretched out on a magnetic tail, or simply the magnetotail. The magnetosphere is filled with plasma composed mainly of electrons and protons, whose main source is the solar wind itself and the ionosphere.

Inside the magnetosphere there are basically two populations of plasma. The first, is a relatively colder (a few eV) and dense ($\sim 10^2 - 10^3$ cm^{-3}) population concentrated mainly in the vicinity of Earth's closed field lines, and it is defined as the plasmasphere.. The second, more energetic (from a few tens of keV up to multi-MeV), but less dense population is trapped by the magnetic field lines and compose the Van Allen radiation belts.

The Van Allen radiation belts are mainly divided in two regions, namely, the inner belt, closer to Earth, being more stable and composed mainly by protons, and, above the so-called slot region, lies the second belt which is named as outer belt. The outer belt is characterized by a higher concentration of higher energy electrons, and also it is more unstable and easily subject to variations of the geomagnetic field. In both radiation belts, the particles describe three main motions: the rotation around the field line, the mirroring between the reflection points on the northern and southern hemisphere and the azimuthal drift around the Earth, and each motion is associated with an adiabatic invariant which is conserved under special circumstances (SCHULZ; LANZEROTTI, 1974). Figure 2.3 illustrates the magnetosphere and

its layers, as described in this section.

Figure 2.3 - Earth's Magnetosphere.
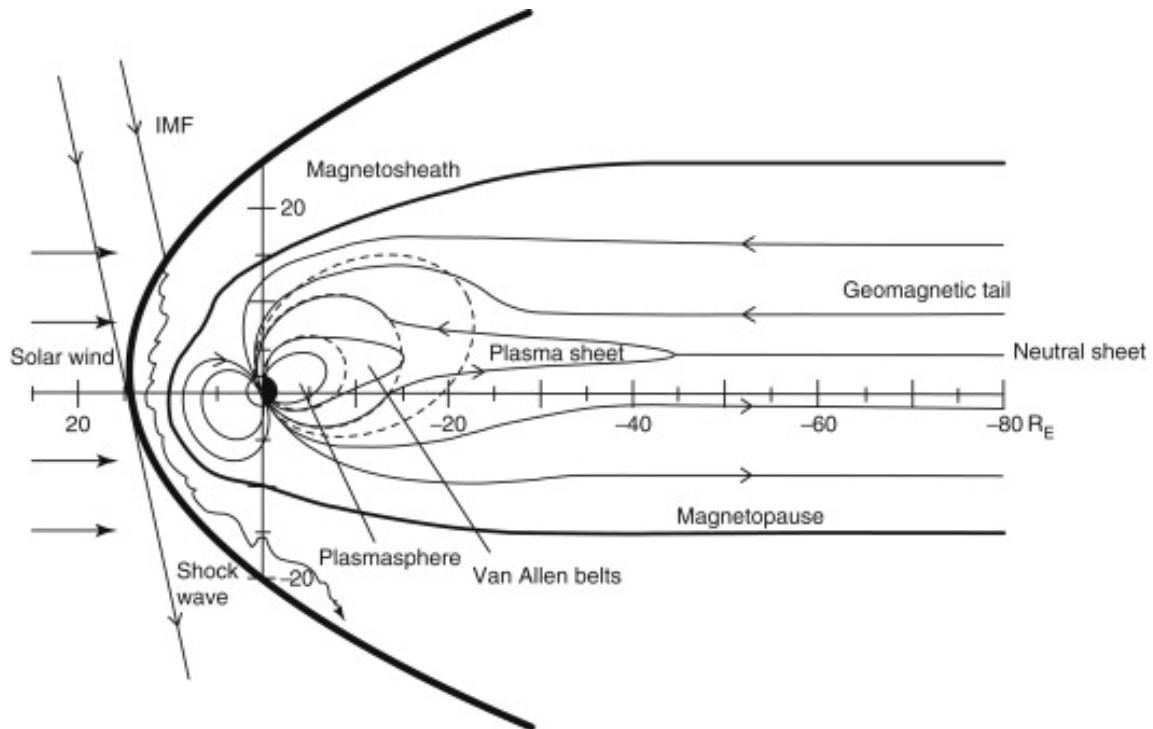
Earth's magnetosphere in the noon–midnight plane. The dashed lines are the original dipole field. The solid lines are magnetic fields modified by external currents. IMF stands for interplanetary magnetic field, which is of solar origin. Major features of the magnetosphere are shown. (RE earth radius.

SOURCE: Parks (2015).

The transition between the neutral atmosphere and the magnetospheric plasma region is a highly ionized plasma known as the ionosphere. The magnetosphere is highly dynamical. Variations in the interplanetary environment or in the current systems within its domain are capable of altering its configuration regarding the flow of currents and particles, thus promoting what we know today by geomagnetic activities.

2.3   Geomagnetic activities

Earth's geomagnetic field fluctuations are generated by several sources. In this work, I will focus on fluctuation that are generated by the solar wind, directly or indirectly.

All currents above the ionosphere are controlled by the solar wind. The main parameters are the dynamic pressure, which depends on the solar wind density, the dusk-dawn component of the electric field, which depends on the solar wind speed, and the IMF.

The main cause of geomagnetic storms on Earth is the strong dawn-dusk electric field associated with the passage of the southward IMF for a sufficiently long time interval that reconnects with Earth's magnetic field and allows the transfer of energy into the magnetosphere (GONZALEZ et al., 1994). These connections are extremely important to the magnetosphere dynamics. This coupling is called the magnetic reconnection (DUNGEY, 1961). The simplified scheme of this coupling is shown in Figure 2.4. Reconnection happens on the day and night sides of the magnetosphere. Reconnection on the day side lead to increased magnetic flux on the night side with plasma injection in the plasmasheet region, which promotes a significant increase in the ring current.

Figure 2.4 - Solar-Earth's magnetic field coupling.
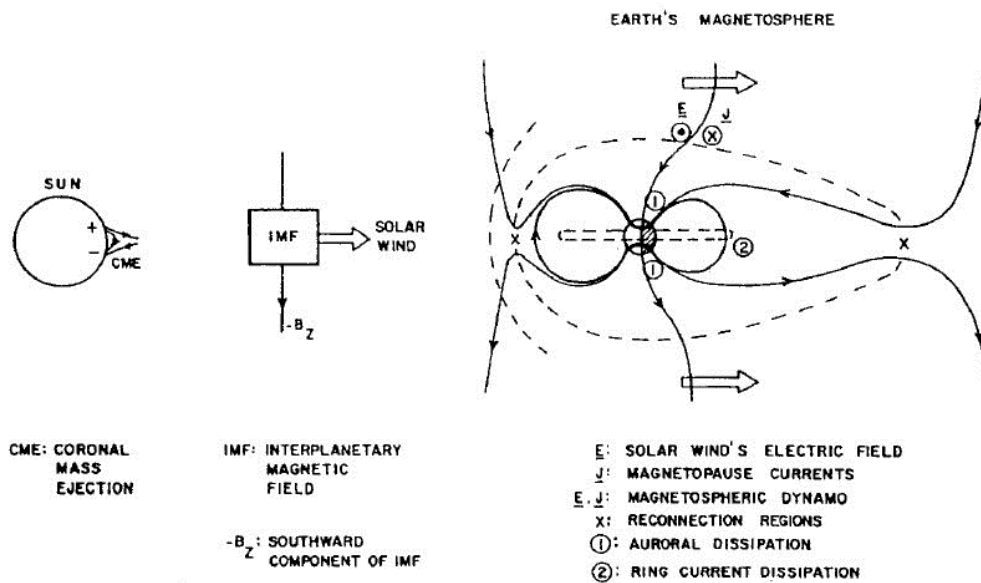
SOURCE: Dungey (1961).

The fluctuation in the solar wind, promotes variations in the currents and consequently is reflected in the measurements on the Earth's surface. When the fluctu-

ations are intense enough, we call them geomagnetic activities (GONZALEZ et al., 1994). Geomagnetic activities are correlated with variations in the Sun since the solar wind is an expansion of solar corona and extends the Solar activities to the interplanetary medium. Variations in the sunspot cycle and in the relative position of the Earth during its orbit around the Sun are observed through geomagnetic indices such as Dst, Kp, aa, ap, AL, AU, AE and Pc. One of the most important indexes monitored on the ground is the Dst index.

The Dst index measures the ring current intensity, which in turn is generated by the growth in the population of trapped magnetospheric particles. These particles undergo drift motion taking ions westwards (midnight-dusk) and electrons eastwards (midnight-dawn).

Through the Dst index it is possible to infer the first effect of the dayside compression due to the flow pressure of the solar wind. This changing on the Dst intensity curve is called storm sudden commencement (SSC). Not every sudden commencement is followed by a storm. The magnetic field, carried by the solar wind, is extremely important to regulate the growth and decay rates of the ring current. The effect of compression on the dayside, when very intense, can denote the occurrence of a magnetic storm, but what defines the storm is the occurrence of the main phase with a significant decrease in the measure of Dst index, being established as a storm when it falls to levels lower than -50 nT (GONZALEZ et al., 1994).

A "perfect" magnetic storm usually starts with the SSC that can last hours, followed by the main phase that is evidenced by the drop in Dst index. The main phase is followed by the recovery phase that can stay for a long time interval. Figure 2.5 showed the Dst index and the three phases. The SSC only represents a beginning of time before the storm but if the IMF is oriented to the north, little energy will be entering the magnetosphere regardless of the speed and particle density of the solar wind.

Figure 2.5 - Dst index during a geomagnetic storm.
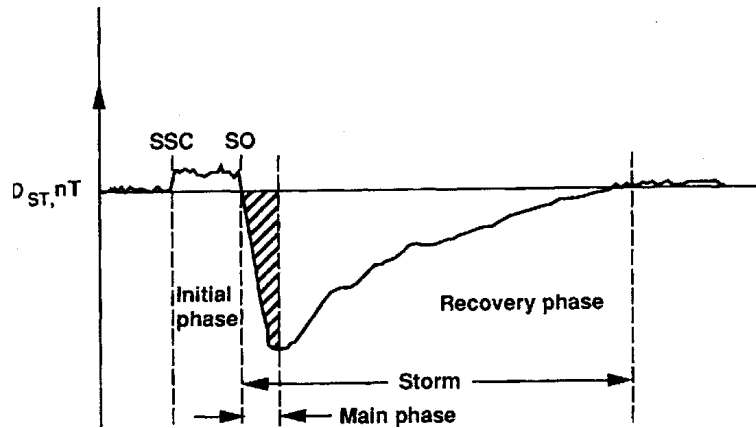
However, when the IMF is southward, antiparallel to the Earth's magnetic field in the equatorial dayside region, the solar wind field is coupled with the magnetosphere and the geomagnetic activities become intense. Figure 2.4 illustrates a storm. The first part is an intense solar activity, in this case a coronal mass ejection (CME). The IMF B_z component is shown as southward. The third part of the figure shows the magnetosphere interacting with the solar wind and the south IMF B_z promoting coupling in the dayside region, followed by magnetic reconnection in the tail, both phenomena corroborate to the intensification of the magnetic storm.

At least two primary mechanisms are responsible for increasing IMF, the speed and density of the solar wind: CMEs and the regions of corotating interaction regions (CIR). CMEs are impulsive generations in the solar corona that normally occur in the phases where the sunspots grow. Whenever they reach Earth's magnetosphere they can be geoeffective and in some cases promote a subset of magnetic cloud injections with IMF oriented North-South.

During the declining phase of the solar activity (decrease or absence of sunspots), the coronal holes dominate the continuous emission of plasmas, expanding from the polar region to equatorial regions of the Sun. This continuous emission of plasma can be accelerated and are known as high speed stream (HSS). If the coronal hole is close to the ecliptic, the Earth's magnetosphere can be reached by this flow. They are low intensity with radial orientation, they are unstable in IMF North-South. However,

this faster front flow meet the slower and denser speed plasma. The solar rotation promotes a field deflection. This region is the CIR. The CIRs are bounded on the rear and front edges by the forward and reverse compression waves, respectively. Storms due to CIR's rarely show Dst index lower than -100 nT and generally do not have the sudden onset (SSC) that are common in CME storms. In addition to the CMEs and CIR there are other modulating factors that increase or decrease the geo-effectiveness, namely, the solar cycle, mentioned earlier by the increase in the number of sunspots, and also the seasons.

2.3.1 Magnetosphere during magnetic storms

The magnetosphere suffers significant changes during magnetic storms: the magnetic field lines compression/expansion, the magnetic reconnection and the particle precipitation into the polar regions among others. The auroral electrojet current can change the direction during the geomagnetic storm and can reach high latitudes of 50° to 80° on the nightside and its intensity can reach tens of thousands of Amperes. It can be said that the auroral electrojet rate of change towards the equator grows at the same rate as the intensity of the storm (FELDSTEIN et al., 1997). The latitudes of auroral precipitation also decrease with the development of storms. The higher occurrence rate of auroras is usually at latitudes of 6°to 10°on calm days advancing to lower latitudes on moderate or more intense days, thus having a good correlation with the advance of the auroral region towards the equator (FELDSTEIN; STARKOV, 1970).

The magnetosphere and magnetopause configuration are altered by the solar wind and its intensification, mainly due to the dynamic pressure (ROELOF; SIBECK, 1993). During the compression, at the dayside region, the magnetopause stand-off distance can reach values as lower as the geosynchronous distance of 6.6 R_E or even lower. In this new configuration, the magnetic field strength isocontours where equatorially mirroring charged particles are trapped in a drift motion (SIBECK et al., 1987, for more details) can be intercepted by the magnetopause boundary which has been pushed inwards, and as a result the charged particles following this isocontour can be lost to the adjacent magnetosheath region. This effect is called magnetopause shadowing (SIBECK et al., 1987; MEDEIROS et al., 2019). Figure 2.6 shows an example of a sudden relativistic electron flux reduction referred to as dropout that occurred in the outer Van Allen radiation belt following a strong magnetopause compression. Magnetopause shadowing has been invoked in this case as the main mechanism to explain the relativistic electron flux decrease (ALVES et al., 2016). The upper

panel shows the (color-coded) flux of trapped electrons throughout the radiation belts as a function of the L-star parameter and time. After September 12, 2014 the electron flux measured by the Relativistic Electron Proton Telescope (REPT) instrument (BAKER et al., 2013) onboard the RBSP-A spacecraft at distances higher than 4 Earth radii were lost. The middle panel shows the magnetopause's stand-off position according to the empirical model of Shue et al. (1998) which reinforces the strong magnetopause compression, i.e., reaching geosynchronous orbit, at the same time when the electron flux dropped abruptly. Notice that in the bottom panel the compression and the dropout were coincident with the most intense phase of the geomagnetic storm identified by the Dst index.

Figure 2.6 - Relativistic Electron flux dropout.
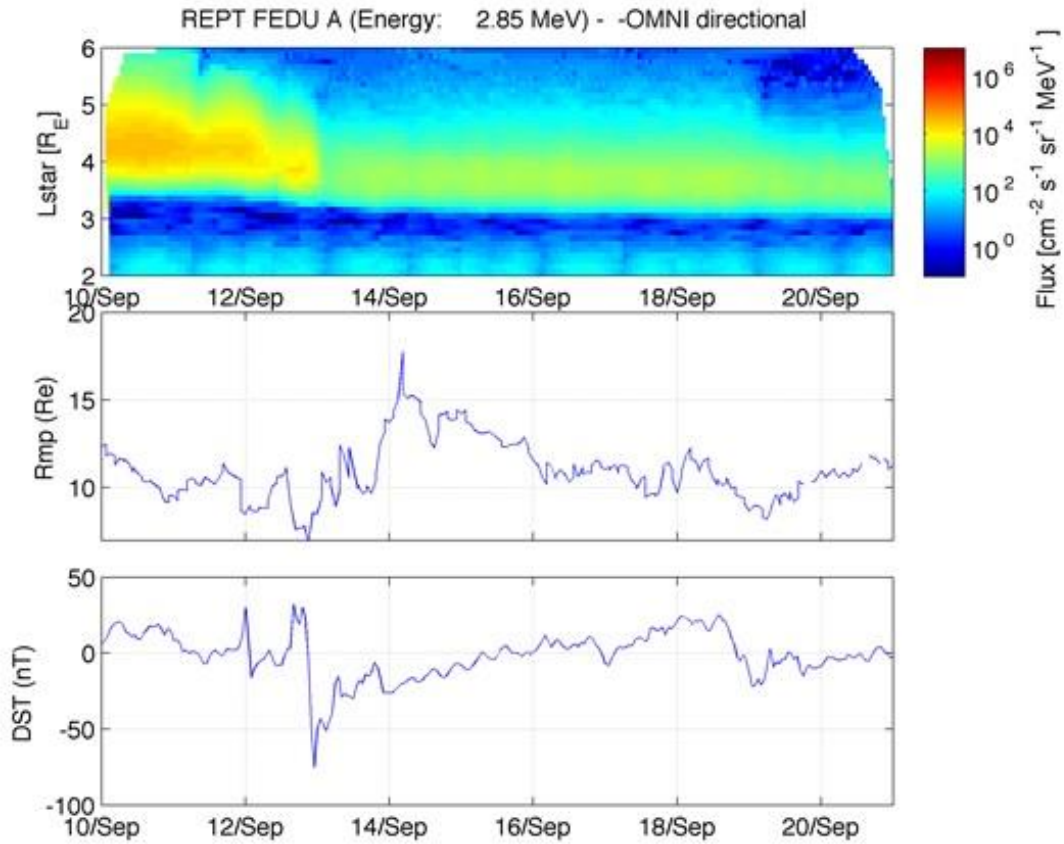
The dropout was caused by magnetopause shadowing after a geomagnetic storm. The top panel shows omnidirectional electron flux at 2.85 MeV energy channel at L-star during September 12-21, 2014. The colorbar represents the electron flux. The middle panel shows the magnetopause contour during the compression according to Shue et al. (1998). The magnetopause contour seemed to reach 6 Re. The bottom panel shows the Dst measured during the same period. The strongest compression are denoted by the Dst value lower than -50nT.

SOURCE: Silva (2015).

There are several other processes excited by magnetic storms and relevant to alter the magnetosphere conditions that will not be treated here. In this study the focus will be magnetospheric waves, specifically the role played by electromagnetic ion cyclotron waves on the relativistic electron flux variability in the outer Van Allen belt. Firstly, let's introduce the particle dynamics on the Van Allen radiation belts.

3 VAN ALLEN RADIATION BELTS

The Van Allen Radiation Belts are formed by energetic particles in a plasma state guided by the Earth's magnetic field (JORDANOVA et al., 2008). Due to their composition, stability and proximity to the Earth's surface, it is conventional to define the existence of two main belts, one more internal, named inner radiation belt and another more external, named outer radiation belt. They normally coexist separated by a region known as slot, but during intense geomagnetic storm intervals they can even compress into one single belt or divide to form up to 3 belts, depending on the conditions of the magnetosphere (BAKER et al., 2014). The innermost radiation belt is more stable, so our attention will be given in a special way to the outermost belt.

The particles trapped in the radiation belts perform three main motions (see Table 3.1 for some details) and each one of them are associated with an adiabatic invariant: gyration (with a typical time scale of milliseconds for electrons) around magnetic field lines; bounce motion (seconds to minutes) along field lines between the magnetic mirror points in each hemisphere, and the drift motion (minutes to hours) around the Earth (ROEDERER; SCHULZ, 1971; ELKINGTON, 2013). These three adiabatic invariants are presented in more details in the next section. Figure 3.1 illustrates these three motions.

Figure 3.1 - The magnetic trapped charged particle motion.
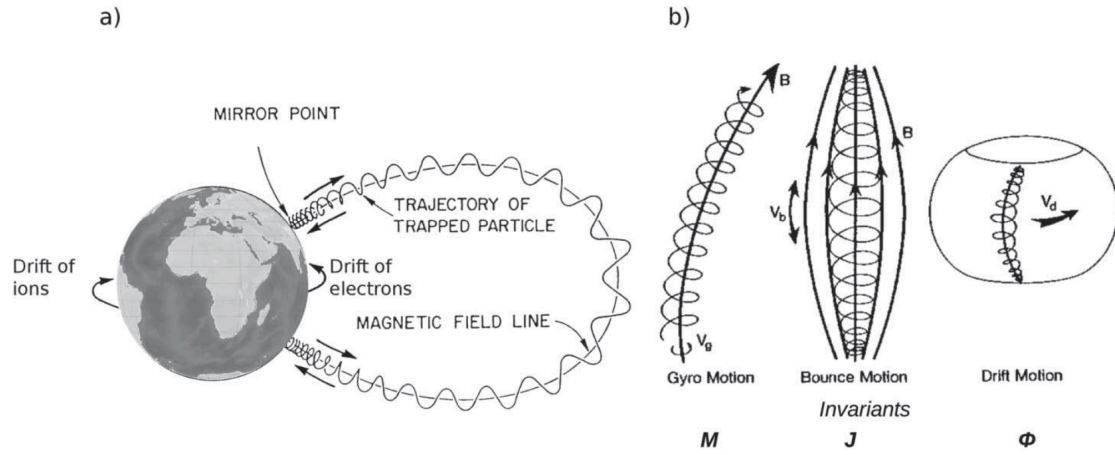
(a) Charged particle motion in a dipolar-like magnetic field line; (b) three adiabatic invariants M, J, and Φ associated, respectively, with: gyro (M), bounce (J), and drift (Φ) motions. The drift motion is eastward for electrons and westward for ions.

SOURCE: Regi (2016).

The electrons trapped in the outer Van Allen radiation belt are originally from two major sources: the solar wind and the ionosphere. Their thermal energy is low, tipically from 1 up to 10 eV, but it grows a few orders of magnitude reaching multi-MeV energies.

The radiation belt dynamics is affected by complex interaction mechanisms and local processes that rules the source and loss of particles (SHPRITS et al., 2009; THORNE,

Table 3.1 - Typical time scales of particle motion

Motion	Invariant	Electron period(s)	Proton period (s)
Gyro	M	$10^{-3} - 10^{-4}$	$10^{-1} - 10^{-2}$
Bounce	J	10^{-1}	10^{0}
Drift	Φ	$10^{2} - 10^{3}$	10^{2}

SOURCE: Author production.

2010). The adiabatic invariants govern their motions and they can be violated once the particles are exposed to fluctuations inherent to the magnetosphere environment. One of these fluctuations are magnetosphere's electromagnetic field waves. They can violate at least one of the three, inclusive all three adiabatic invariants simultaneously (SCHULZ; LANZEROTTI, 1974). Wide wave frequency bands are detected in the near space. CMEs and the disturbed solar wind interact with the Earth's magnetosphere contributing to plasma instabilities that in turn give rise to plasma waves. These waves interact with local energetic particles being either enhanced or damped, changing particles' energy and even promoting their precipitation into the atmosphere (PARKS, 2003).

The ultra-low frequency (ULF) waves ($\sim 2 - 5000$ mHz) can violate the third adiabatic invariant (Φ) promoting either outward or inward radial diffusion. They can be enhanced during geomagnetic storms playing an important role in particle acceleration (ROSTOKER et al., 1998; ELKINGTON, 2013; HUDSON et al., 2013; O'BRIEN et al., 2001; SHPRITS; THORNE, 2004) or particles loss (SHPRITS et al., 2006; JORDANOVA et al., 2008; LOTO'ANIU et al., 2010). Another example are the extremely-low frequency (ELF) waves and very-low frequency (VLF) waves that can violate the first (M) and second (J) adiabatic invariants promoting loss of particles to the atmosphere (THORNE; KENNEL, 1971; LYONS; THORNE, 1972; ABEL; THORNE, 1998) or energy diffusion (HORNE; THORNE, 1998; SUMMERS et al., 1998; HORNE et al., 2005; MIYOSHI et al., 2003). Figure 3.2 illustrates the major magnetospheric waves and their favorable propagation regions. Whistler mode chorus waves can induce small bursts and local acceleration between midnight and noon local time sectors. Magnetosonic equatorial waves contribute locally to electron acceleration. Pitch angle scattering can be driven by electromagnetic ion-cyclotron (EMIC) waves (USANOVA et al., 2014) and whistler mode chorus waves as well (THORNE, 2010).

Figure 3.2 - Schematic illustration of waves in the inner magnetosphere
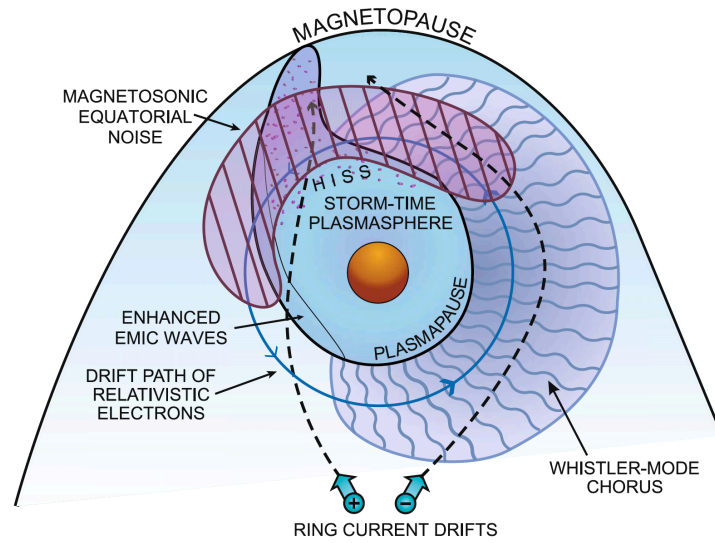
The spatial distribution of important waves in the inner magnetosphere. Drift paths of both ring current particles and relativistic electrons as well as relevant plasma boundaries such as plasmapause and magnetopause are also sketched.

SOURCE: Thorne (2010).

The frequency range of mostly of the magnetospheric waves are illustrated in Figure 3.3. The next sections present a brief overview of waves in space plasmas.

Figure 3.3 - Nomenclature of electromagnetic waves and frequency ranges.
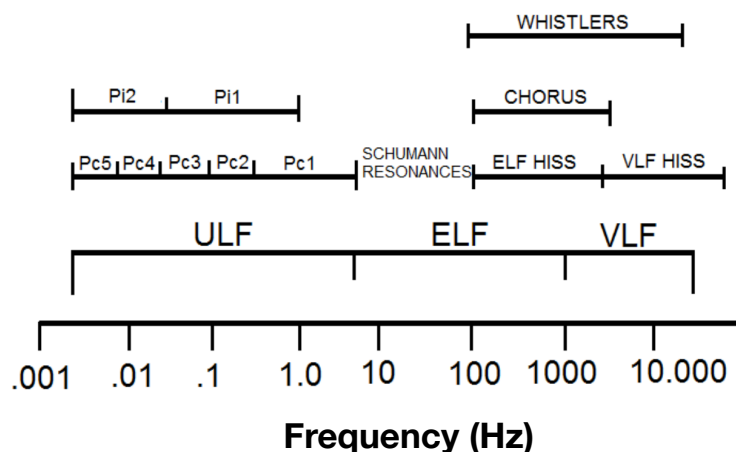
Typical magnetosphere's electromagnetic waves and their frequency ranges. Ultra-Low Frequency (ULF), Extremely-Low Frequency (ELF), Very-Low Frequency (VLF), continuous pulsations (Pc), and irregular pulsations (Pi). Schumann resonances are set up in the Earth-ionosphere wave guide.

SOURCE: Parks (2003).

3.1 Basic concepts of wave-particle interactions

The following review is mostly based on the paper by (TSURUTANI; LAKHINA, 1997) which tries to explain some fundamental concepts of wave particle interactions, which is our main target here. More details can be obtained from, e.g., (KENNEL; PETSCHEK, 1966; LYONS; WILLIAMS, 1984; PARKS, 2003; BITTENCOURT, 2004).

A plasma environment can sustain wave phenomena, thus Earth's magnetosphere can be used as natural laboratory to understand waves propagating in plasmas. An example of space plasma waves is the Alfvén wave, i.e., transverse (to the local magnetic field direction) magnetic field fluctuations propagating along the local magnetic field direction without corresponding changes in plasma density. Such waves may arise from, e.g., magnetospheric's magnetic field fluctuations due to solar wind dynamic pressure variations. Wave-particle interactions play a role for the formation of magnetopause boundary layer, generation of electromagnetic outer zone chorus and plasmaspheric hiss emissions, precipitation of particles promoting auroras, etc

(TSURUTANI; LAKHINA, 1997). Low frequency waves can interact with charged particles thereby transporting energy from one region to another. Ion cyclotron waves and whistler mode waves can pitch angle-scatter energetic particles into the loss cone causing the decay of the ring current during the recovery phase of a magnetic storm. These particles can cause diffuse aurorae, enhanced ionization in the ionospheric D and E regions, and bremsstrahlung X-rays (TSURUTANI; LAKHINA, 1997). Since the space plasma collision time is very long when compared with the characteristic timescales of the system, the plasma can be treated as collisionless. The interaction between a wave and a charged particle becomes strong when the streaming particle velocity is such that the particle senses the Doppler-shifted wave frequency and its cyclotron frequency harmonics.

The resonant interaction between electromagnetic waves and particles are dominated by the Lorentz force. The electron plasma frequency $\Omega_{pe} = (4\pi N q^2 m^{-1})^{\frac{1}{2}}$ is greater than the electron cyclotron frequency (Ω^-), where N is the electron number density, q the elementary charge, and m is the electron rest mass. The force F_L (in centimeter-gram-second cgs units) acting in a charged particle q, moving with velocity V across the magnetic field of strength B_0 is given by:

$$F_L = \frac{q}{c} V \times B_0 \tag{3.1}$$

where c is the speed of light. In a uniform magnetic field B_0, the force acts only in the direction perpendicular to both the particle's perpendicular velocity vector $V_\perp$ and the local magnetic field direction then forcing the particle to perform a circular motion about the local magnetic field direction. Figure 3.4 illustrates this. The circular orbit radius r is referred to as the gyroradius, and the particle's cyclotron frequency Ω can be calculated according to the following equations. The Lorentz and centrifugal forces can be written as

$$F_{centrifugal} = m \frac{V_\perp^2}{r} \tag{3.2}$$

The Lorentz F_L is the centrifugal force, then:

$$F_L = q\frac{V_\perp B_0}{c}$$

$$m\frac{V_\perp^2}{r} = q\frac{V_\perp B_0}{c} \qquad (3.3)$$

The Larmor radius can be obtained by:

$$r = m\frac{V_\perp c}{qB_0} \rightarrow \text{Gyroradius}$$

$$\frac{d\theta}{dt} = \frac{V_\perp}{r} \qquad (3.4)$$

Thus,

$$\Omega = \frac{qB_0}{mc} \rightarrow \text{Cyclotron Frequency} \qquad (3.5)$$

Figure 3.4 - The Lorentz force acting in a proton in a uniform magnetic field.
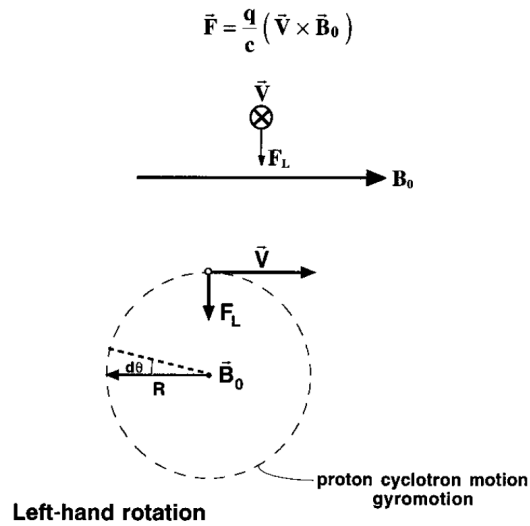
SOURCE: Tsurutani e Lakhina (1997).

Considering a positively charged particle whose motion in a uniform magnetic field is depicted in Figures 3.4 and 3.5, one can define the local pitch angle α as the angle the particle's velocity vector makes with the local magnetic field vector. Figures 3.4 the magnetic field line $\overrightarrow{B_0}$ is pointed out to the plane. The particle's velocity vector can be decomposed into two orthogonal components: one parallel to B_0 and denoted by $V_\parallel$, and the other perpendicular ($V_\perp$) to B_0 such that $\overrightarrow{V} = V_\parallel(\overrightarrow{B_0}/|\overrightarrow{B_0}|) + V_\perp$. The pitch angle is defined as shown in Figure 3.5

Charged particle motion in a non-uniform magnetic field is somewhat more complex, and depending on the magnetic field's spatial configuration the charged particle can be effectively trapped in the magnetic field, as it is the case for a "magnetic bottle" configuration, as depicted in the upper part of Figure 3.6. The field strength varies along the axial direction of the "bottle", being minimum at the center and having two local maxima at the regions where the field lines are converging. The Lorentz force in these two local maxima regions is directed to the center of the "bottle", and depending on their pitch angles in the lowest field strength region, i.e., at the center of the "bottle", the particle's can be effectively mirrored and bounce back and forth between both magnetic field lines converging regions, and thus become trapped. Particles with pitch angles near 0° will mirror at extremely high field strengths and may be lost to the loss cone. The loss cone is the value of the pitch angle where particles can be lost to the atmosphere, as seen in Figure 3.7(a). It can be calculated by assuming the first adiabatic invariant $\mu = E_\perp/B_0$ is conserved, where $E_\perp$ is the particle's kinetic energy associated with the gyro motion, and considering that the magnetic field spatial variation is small within a Larmor radius. Considering that the total kinetic energy E_T is conserved, since the Lorentz force as given by Equation 3.1 produces no work on the particle, it can be compared with the kinetic energy at the equator, thus $\frac{E_T}{B_{mirror}} = \frac{E_\perp}{B_{equatorial}}$ by constancy of the first adiabatic invariant. Since $E_\perp = \frac{1}{2}m(V^2 \sin\alpha_0^2)$, where α_0 is the pitch angle at the equator which defines the loss cone, and $E_T = \frac{1}{2}mV^2$, one can easily find:

$$sin^2\alpha_0 = \frac{B_{equatorial}}{B_{mirror}.} \tag{3.6}$$

Figure 3.5 - Pitch angle

$$\sin \alpha = \frac{V_\perp}{V}$$

Left-hand corkscrew
motion spiral
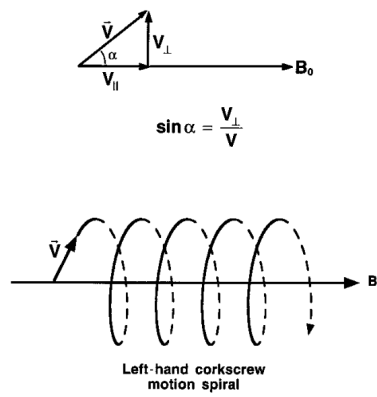
(upper) Pitch angle α definition, and (lower) helicoidal motion of a positively charged particle in an uniform magnetic field. The ion gyrates in a left-handed sense following the left-hand corkscrew rule. Negatively charged particles, on the other hand, follow the right-hand corkscrew rule.

SOURCE: Tsurutani e Lakhina (1997).

Figure 3.6 - Gyro and bounce motion.

Magnetic Bottle

$$\mu = \frac{E_\perp}{B} = \text{constant}$$

(first adiabatic invariant)
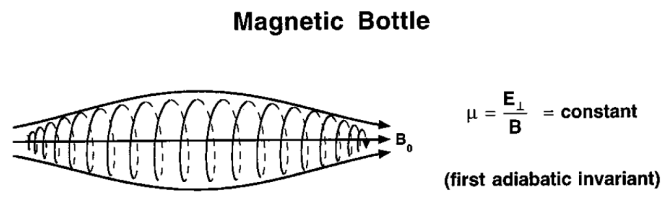
Earth's Radiation Belts
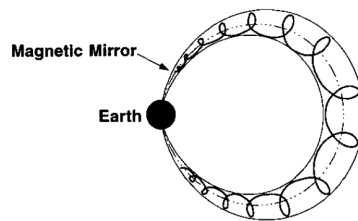
First and second adiabatic invariant representation: magnetic bottles for plasma particles and the magnetic mirror on the Earth's radiation belts.

SOURCE: Tsurutani e Lakhina (1997).

Figure 3.7 - Loss cone.

Loss Cone

a)

$V_\perp$

α } "loss cone"

$V_\parallel$

Aurora Borealis and Australis

b)

B_{mirror}

$B_{equator}$

atmosphere
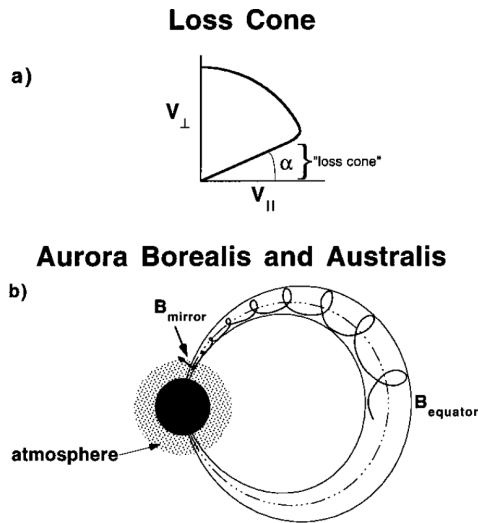
(a) Equatorial loss cone, and (b) auroras associated with particle pitch angle scattering into the loss cone.

SOURCE: Tsurutani e Lakhina (1997).

This framework of trapping and loss of particles can be used in the context of the Van Allen radiation belts (ALLEN, 1991). Particles undergo a gyro motion about the magnetic fields and a bounce motion where the particles move back and forth between the mirror points on the Northern and Southern hemispheres, as depicted in the bottom half of Figure 3.7. Near the equatorial region of the magnetosphere, electrons and ions drift in opposite directions due to their charge, with the electrons drifting eastward and ions drifting westward. The ring current is constituted in this way, and it is very sensitive to magnetic storms, since they inject and energize the ring current particles. Particles performing these three motions form the Van Allen radiation belts. Perturbations in the magnetic field or wave-particle interactions can change their configuration and the Van Allen radiation belt particles can be either lost, transported or accelerated.

3.1.1 Resonant wave-particle interactions

The resonant wave-particle interactions happens when the condition below is satisfied:

$$\omega - \overrightarrow{k} \cdot \overrightarrow{\mathcal{V}} = n\Omega, \tag{3.7}$$

where ω are the wave frequency and $\overrightarrow{\mathcal{V}}$ wave vector, respectively, and n is an integer corresponding to the harmonics.

Considering, for illustration purposes, $n = 1$ for the fundamental resonance condition, and also considering electromagnetic waves propagating either parallel or antiparallel to the magnetic field direction, i.e. $\overrightarrow{k} = k_{\parallel}\hat{b}$, we have $\omega - k_{\parallel}V_{\parallel} = \Omega$. This way, the parallel phase velocity can be obtained as follows:

$$\omega - k_{\parallel}V_{\parallel} = \Omega \tag{3.8}$$

Then,

$$V_{\parallel R} = \frac{(\omega - \Omega)}{k_{\parallel}} \tag{3.9}$$

The parallel kinect energy of particles can be described as

$$E_{\parallel R} = \frac{1}{2}mV_{\parallel R}^2 \tag{3.10}$$

Thus,

$$\frac{1}{2}m\frac{(\omega - \Omega)^2}{k_{\parallel}^2} = \frac{1}{2}mV_{ph}^2(1 - \frac{\Omega}{\omega})^2 \tag{3.11}$$

Where $V_{ph} = \omega/k_{\parallel}$ is the wave parallel phase velocity. When the resonant waves frequency are much less than the ion cyclotron frequency, the phase velocity can be approximated by the local Alfvén speed $V_A = [B^2/4\pi\rho]^{\frac{1}{2}}$ where ρ is the plasma density.

The polarization of waves is defined by the sense of rotation of the wave field with time at a fixed location. The sense is with respect to the ambient magnetic field and is independent of the direction of propagation (TSURUTANI; LAKHINA, 1997). Figure 3.8 illustrates two fundamental polarization: left-handed and right-handed. They can be elliptical or linear polarized as a combination of these two fundamental polarization.

Figure 3.8 - Wave propagation.

Electromagnetic Wave Polarizations
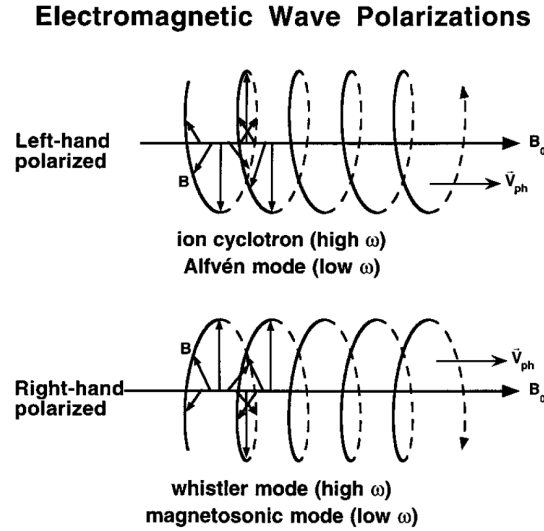
Left-hand and right-hand polarized waves propagating parallel to the magnetic field B_0.

SOURCE: Tsurutani e Lakhina (1997).

When the plasma is magnetized and $\Omega_{pe} > \Omega^-$, left-hand polarized waves can exist at frequencies up to the ion cyclotron frequency. Waves at the high end of these frequencies are named as ion cyclotron waves. At low frequencies this mode maps into the Alfvén mode branch. Right-hand mode waves can exist up to the electron cyclotron frequency. They are dispersive, which means they can suffer damping and ceases to propagate. When these right-hand waves travel any substantial distance, the highest-frequency component arrives first (TSURUTANI; LAKHINA, 1997). An example is the whistler mode generated by electromagnetic radiation emitted by Lightning. They start at high frequencies and descend to lower frequencies. They also can be magnetosonic mode when they reach lower or magnetohydrodynamic frequencies.

3.1.2 Normal resonance

For the normal cyclotron resonance between waves and charged particles, the waves and particles propagate towards each other, as shown in Figure 3.9. In this case, left-hand positive ions interact with left-handed waves, and correspondingly, right-

29

hand electrons interact with right-hand waves. The relative motion of the waves and particles causes a Doppler shift of the wave frequency ω up to the particle cyclotron frequency Ω.

Figure 3.9 - Wave mode propagation.

(Normal) Cyclotron Resonance

ions

$V_{\parallel}$ V_{ph} B_0

ion   Left-hand wave

$$\omega - \bar{k} \cdot \bar{V} = \Omega^+$$

$$\omega + k_{\parallel}V_{\parallel} = \Omega^+$$

The relative motion between the wave and particle Doppler shifts the wave up to the ion cyclotron frequency.

electrons

$V_{\parallel}$ V_{ph} B_0

electron   Right-hand wave

$$\omega + k_{\parallel}V_{\parallel} = \Omega^-$$
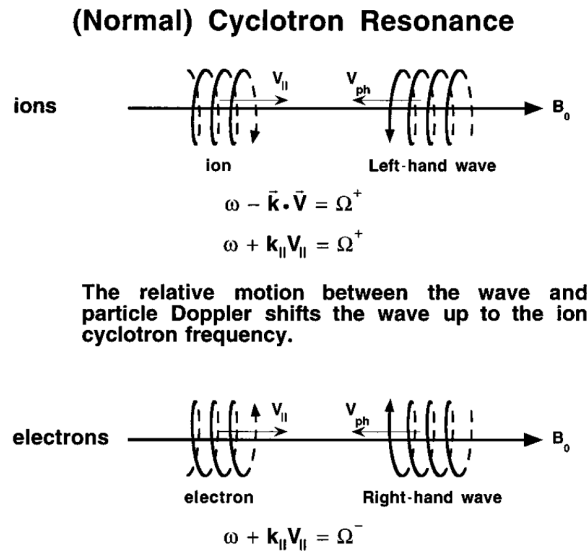
Normal first-order cyclotron resonance between electromagnetic circularly polarized waves and charged particles.

SOURCE: Tsurutani e Lakhina (1997).

In the magnetosphere, such waves are known to be generated by a plasma instability referred to as the "loss cone instability". These waves can interact with Van Allen radiation belt particles changing their composition. The loss cone instability occurs when the particle's perpendicular temperature $T_{\perp}$ is higher than the particle's parallel temperature $T_{\parallel}$, i.e., $T_{\perp}/T_{\parallel} > 1$, assuming the plasma has a "bi-Maxwellian" distribution. Both whistler mode chorus waves and "plasmaspheric hiss" can be generated by electron loss cone instabilities.

Extremely low frequency (ELF) chorus waves is a common naturally occurring, intense electromagnetic emission observed in the Earth's magnetosphere. Many observed features of chorus waves can be explained by the cyclotron resonance condi-

tion between the whistler mode waves and energetic (10 keV up to 100 keV) electrons injected by substorm electric fields. For more details on chorus waves the reader is referred to, e.g., (TSURUTANI; LAKHINA, 1997) and references therein.

3.1.3 Anomalous resonance

Another type of resonance is called anomalous cyclotron resonance. An example of it is when positive left-hand ions interact with right-hand waves. It happens because the ions overtake the waves ($V_\parallel > V_{ph}$) so that the ions sense the waves as left-hand polarized. In this case, the Doppler shift decreases the wave frequency to the cyclotron frequency. The same anomalous cyclotron resonant interactions occur between electrons and left-hand polarized waves. The difference is that resonant electrons are typically relativistic ($E_\parallel > \text{MeV}$).

Particle pitch angle scattering via interaction with electromagnetic waves is associated with the Lorentz Force. At cyclotron resonance the particle feels the wave magnetic field gyrating in phase with it. The resonant wave-particle interaction occurs on smaller time-scales in comparison with the cyclotron period, and as a result the first adiabatic invariant is not conserved. A highly anisotropic pitch angle distribution with, say, $T_\perp \gg T_\parallel$, stimulates wave growth via the loss cone instability. It means that in turn waves scatter the particles to "fill" the loss cones until one gets to the stably trapped limit. For more details see, e.g., (TSURUTANI; LAKHINA, 1997).

As for the wave electric field it can either increase or decrease particle's perpendicular kinetic energy, and therefore changing the pitch angle, depending on the phase of the wave with respect to the particle (TSURUTANI; LAKHINA, 1997).

3.1.4 Pitch angle scattering

Based on Section 4 from (TSURUTANI; LAKHINA, 1997) we derive the pitch angle scattering rates below. If $\tan \alpha = V_\perp / V_\parallel$ and considering that for large pitch angle particles $V_\perp \cong V$, then:

$$\Delta \alpha = -\frac{\Delta V_\parallel}{V_\perp}. \tag{3.12}$$

The maximum change in the charged particle parallel velocity interacting with an electromagnetic wave is given by:

$$\Delta V_\parallel = \left(\frac{q V_\perp B}{m} \right) \Delta t,$$

$$\Delta \alpha = \frac{e V_\perp}{mc} B \Delta t \frac{1}{V_\perp} = \frac{B}{B_0} \Omega \Delta t. \tag{3.13}$$

The pitch angle diffusion rate is:

$$D \approx \frac{(\Delta \alpha)^2}{2 \Delta t} \cong \frac{\Omega^2}{2} \left(\frac{B}{B_0} \right)^2 \Delta t, \tag{3.14}$$

where Δt is the time needed for a particle $\Delta k/2$ out of resonance to change its phase by 1 rad or $\Delta t \cong 2/\Delta k V_\parallel$. Thus:

$$D \approx \Omega \frac{B^2/\Delta k}{B_0^2} \frac{\Omega}{V \cos\alpha} = \Omega \frac{B^2/\Delta k}{B_0^2} \frac{k}{\cos\alpha} \tag{3.15}$$

Assuming large pitch angle particles,

$$D = \Omega \left(\frac{B}{B_0} \right)^2 \eta, \tag{3.16}$$

where $\eta = (\Omega/\Delta k V_\parallel)$ is the fractional amount of time that particles are in resonance with the waves. Particle transport across the magnetic field can be calculated once the mobility of the charged particles in the direction perpendicular to the ambient magnetic field is known. The Pederson mobility $\mu_\perp$ of particles in the direction perpendicular to B_0 is:

$$\mu_\perp = (c/B_0)\Omega\tau_{eff}/[1 + (\Omega\tau_{eff})^2], \tag{3.17}$$

where τ_{eff} is the effective time between wave particle interactions. The maximum cross-field diffusion occurs when the particles are scattered at a rate equal to their gyrofrequencies, or $\tau_{eff}^{-1} \approx eB_0/mc$. A spatial diffusion coefficient derived by Rose e Clark (1961):

$$D_\perp = \langle \Delta x_\perp \rangle^2 /2\Delta\tau = m(V_\perp^2/2e)\mu_\perp \tag{3.18}$$

For conditions where $\Omega\tau_{eff} \gg 1$ and $\tau_{eff} \approx 1/D$, Tsurutani and Thorne (1982) have used 3.15 and 3.18 to determine the cross-field diffusion rate due to the magnetic component of electromagnetic waves by:

$$D_{\perp,B} = \frac{E_\perp}{e}\frac{c}{B_0}\frac{1}{\Omega\tau_{eff}} = 2\eta(B/B_0)^2 D_{max} \qquad (3.19)$$

Similarly for electrostatic waves, we obtain:

$$D_{\perp,E} = 2\eta(E/B_0)^2(c/\upsilon)^2 D_{max} \qquad (3.20)$$

Figure 3.10 shows the process of cross-field diffusion due to resonant wave-particle interactions. B_0 is the original guiding center magnetic field line. After pitch angle scattering, the guiding center lies on the B_0^{ι} magnetic field line. The particle has diffused across magnetic field lines.

Figure 3.10 - Particle diffusion.
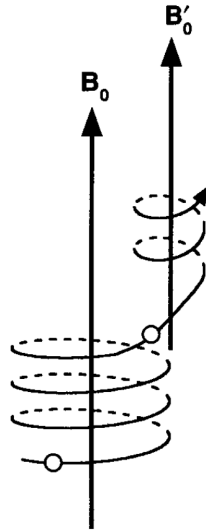
Particle cross-field diffusion by resonant interactions with waves.
SOURCE: Tsurutani e Lakhina (1997).

This chapter is a simple explanation with illustrations to explain the fundamentals of wave-particle interactions; more details can be found elsewhere, e.g., (STIX; SCOTT, 1963; KENNEL; PETSCHEK, 1966; ROEDERER; SCHULZ, 1971; KURTH; GURNETT, 1991; PARKS, 2003; BITTENCOURT, 2004) and references therein. The next section presents the principal magnetospheric waves.

3.1.5 Waves in space plasmas

Several waves propagate in the Van Allen radiation belts and they promote relevant effects on particles. The wave propagation modes can be characterized by their dispersion relation, which is a functional relation between the wave frequency ω and the wave number k, and by its polarization, as described in Section 3.1. Table 3.2 presents the dispersion relation for a given propagation mode for a number of waves commonly found in space plasmas. For more details on how to find dispersion relations of plasma waves see, e.g., (PARKS, 2003).

Table 3.2 - Principal waves, their dispersion relation and propagation mode.

WAVES	Dispersion Relation	Propagation mode
Langmuir	$\omega^2 = \omega_p^2 - 3k^2 V_{th}^2$	$B_0 = 0 \vee k \parallel B_0$
Ion Acoustic	$\dfrac{\omega^2}{k^2} \approx \dfrac{kBT_e}{(m_i(1 + k^2\lambda_D^2))}$	$B_0 = 0 \vee k \parallel B_0$
Upper Hybrid	$\omega^2 = \omega_p^2 - \omega_c^2$	$k \perp B_0, k \parallel E$
Ion Cyclotron	$\omega^2 = \Omega_c^2 + k^2 C_s^2$	$k \perp B_0, k \parallel E$
Lower Hybrid	$\omega^2 = \omega_c \Omega_c$	$k \perp B_0, k \parallel E$
Bernstein	$\omega_n^2 = n\omega_c^2(1 + \alpha_n)$	$k \perp B_0, k \parallel E$
Light	$\omega^2 = \omega_p^2 + k^2 c^2$	$B_0 = 0, k \parallel E$
Ordinary	$\omega^2 = \omega_p^2 + k^2 c^2$	$k \perp B_0, k \perp E$
Whistlers (right hand polarized)	$n_R^2 = 1 - \left[\dfrac{\dfrac{\omega_p^2}{\omega^2}}{1 - \dfrac{\omega_c}{\omega}} \right]$	$k \parallel B_0, k \perp E$
Whistlers (left hand polarized)	$n_L^2 = 1 - \left[\dfrac{\dfrac{\omega_p^2}{\omega^2}}{1 + \dfrac{\omega_c}{\omega}} \right]$	$k \parallel B_0, k \perp E$
Alfven	$V_{ph}^2 = V_A^2$	$k \parallel B_0, k \perp E$
Magnetosonic	$V_{ph}^2 \approx V_A^2 + C_s^2$	$k \perp B_0, k \perp E$

SOURCE: Parks (2003).

3.1.5.1 Chorus waves

Chorus waves are whistler modes of coherent emission often found in two distinct bands, namely, between 0.5 $\Omega_{ce} < f < 0.8$ Ω_{ce} (upper band) or 0.1 $f\Omega_{ce} < f < 0.5$ Ω_{ce} (lower band) (TSURUTANI; SMITH, 1974). For parallel (to the magnetic field) propagation, they are right-hand circularly polarized.

Chorus waves are important because they can cause both the loss and the acceleration of electrons in the radiation belt (BORTNIK; THORNE, 2007) and are the dominant process in the precipitation of particles in the auroral region due to diffusion (NI et al., 2008; THORNE, 2010). The intensity of the chorus wave is highly variable as is the way it responds to geomagnetic activities. It is intensified in a large spatial region beyond the plasmapause associated with gyro-resonant excitations during the electron injections via plasma sheet into the magnetosphere (LI et al., 2009; HWANG et al., 2007). On the nightside, chorus are intensified at $L = 8$ and confined to latitudes below 15° due to the Landau damping effect of oblique waves during their propagation towards high latitudes (BORTNIK; THORNE, 2007). In contrast, on the dayside region, chorus waves are found at various latitudes, being more intense close to $L = 8$ and less dependent on geomagnetic activities (TSURUTANI; LAKHINA, 1997). Thus, it has been a challenge to understand its excitation since it occurs even in geomagnetically calm periods and when the electrons flux is low (THORNE, 2010).

Chorus can also be an efficient mechanism of energy transfer between populations of electrons injected with low energy, which generate waves, and electrons trapped with high energy already in the radiation belt. This occurs through the energy diffusion process (HORNE; THORNE, 2003). This acceleration can accelerate electrons to relativistic energies on time scales of the order of a day (HORNE et al., 2005). Simulations show that the diffusion of energy by chorus, for some events, increased the electrons fluxes in the outer radiation belt and may be associated with constant geomagnetic activity during the recovery phase and during a replenishment of the slot region during a storm (THORNE, 2010). Several 2-D and 3-D energy diffusion and pitch angle simulations have been used to demonstrate the importance of local stochastic processes in the loss and electron flux acceleration. Statistically, the interaction of electrons with such intense waves tends to pitch angle-scatter electrons into the loss cone more than stochastic diffusion. Thus, they can be associated with sudden electron flux dropout (ONSAGER et al., 2007). Electron trapping in the nonlinear phase in which chorus waves have high amplitude can also lead to non-diffusive acceleration

in relativistic energies (THORNE, 2010).

3.1.5.2 Electrostatic electron cyclotron harmonic waves

Electrostatic electron cyclotron harmonic (ECH) waves are electrostatic emissions that occur in the bands between the multiple harmonics of the electron's gyro frequency. These waves are confined to regions of low plasma density outside the plasmapause and have their maximum values during enhanced magnetic activities and are always close to the magnetic equator. Predominantly they spread electrons with energies on the order of keV and can affect the seed populations of relativistic electrons, but not the electrons on the order of MeV energies. They are excited by the loss cone instability of electrons injected into the plasma. Its performance is similar to that caused by chorus, but for lower energy electrons on the order of keV, and can contribute to auroral precipitation, however in an almost insignificant way compared to chorus (THORNE, 2010).

3.1.5.3 Plasmaspheric hiss

Plasmaspheric Hiss is an incoherent emission (whistler), in the range of 100 Hz to several kHz (ELF), confined in the dense plasmasphere and in the plasmaspheric plume on the dayside magnetopshere region. The plasmaspheric hiss is mainly responsible for the slot region formation in the Earth's Van Allen belts. It propagates preferentially along the magnetic field line near the geomagnetic equator and it is more oblique at high latitudes. It is right-hand circularly polarized. Their amplitude is typically on the order of 10 pT or less during quiet geomagnetically conditions to greater than 100 pT during the storm recovery phase (MEREDITH et al., 2004). Hiss waves originate from chorus emissions that escape from Landau damping during its propagation from the equatorial region to high latitudes. These waves also propagate at low L where they are trapped in the plasmasphere, where a discrete chorus-like emission merges to the incoherent hiss mode. The hiss characteristics are used to estimate the life span of the electron in the plasmasphere and the contribution to the slow decay of the external radiation belt after its increase in the storm period. Hiss waves are also observed during a storm and they are intense enough to contribute significantly to scatter electrons in the outer zone (THORNE, 2010). Emissions are also present on quiet days and/or in the presence of storms.

3.1.5.4 Magnetosonic equatorial waves

Magnetosonic equatorial waves, or equatorial magnetosonic waves, are highly oblique, whistler-excited wave emissions within a few degrees of the equator plane at frequencies between the proton's gyro frequency and the lower hybrid frequency band ($< f_{lh}$). These waves are observed both inside and outside the plasmapause and are excited by a resonant cyclotron instability with ions injected by the ring current. They are also influenced by Landau resonance with the electrons from the radiation belt (100 keV to a few MeV), and the spectral properties of the observed magnetosonic wave intensity are used to demonstrate the diffusion of energy in a time scale of days and can be comparable to those due to spreading by chorus.

The power spectral density below (Figure 3.11) shows the different types of waves present in the magnetosphere according to their frequency. It is possible to observe the presence of the plasmapause boundary, the electron cyclotron frequency f_{ce} and the upper hybrid frequency f_{UHR}, as well as the enhancement of the power spectral density at characteristic frequencies from the ECH, whistler mode chorus, plasmaspheric hiss and equatorial magnetosonic waves, correlated with their frequency band propagation and in relation to the L-shell position. The data were extracted from the CRRES (Combined Release and Radiation Effects Satellite) satellite on September 12-13, 1990 for the period 17:42 UT to 02:48 UT, corresponding to an orbit around the Earth.

Figure 3.11 - The wave spectrogram observed by the CRRES satellite.
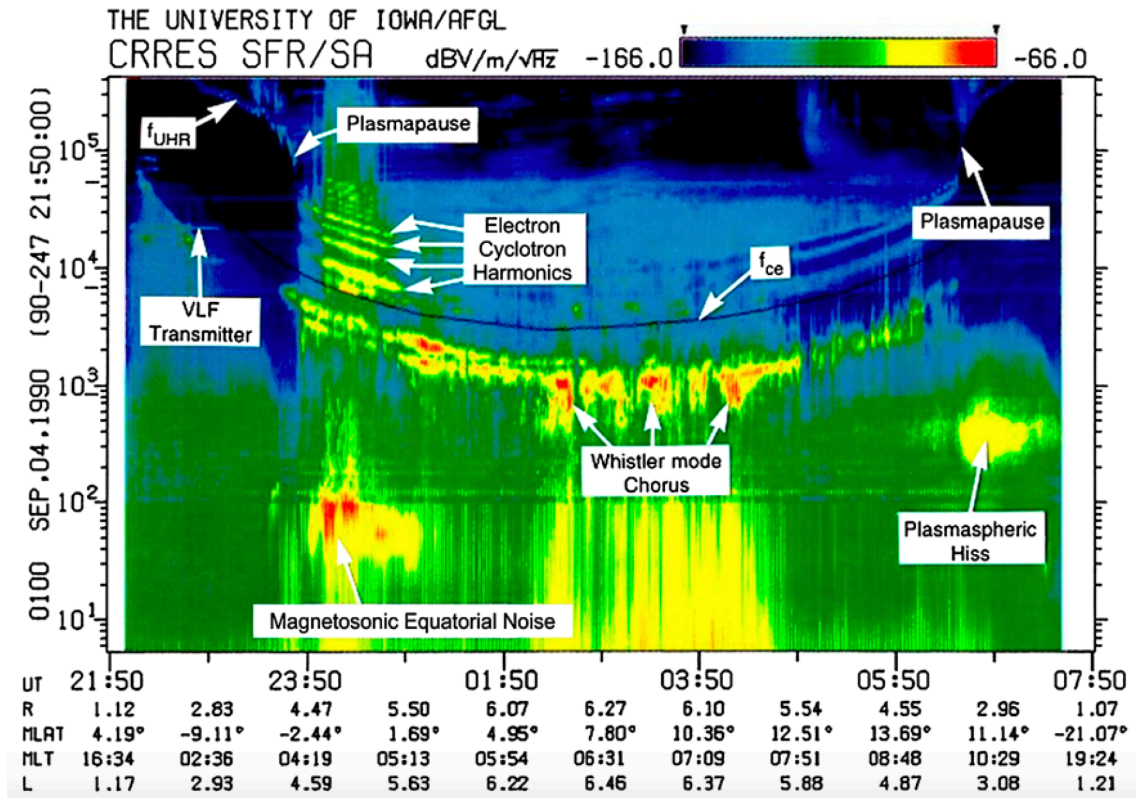
The presence of ECH waves, magnetosonic equatorial waves, plasmaspheric hiss, and whistler mode chorus. The black line delimits the electron cyclotron frequency f_{ce}. The intensity of the frequency spectrum of the electric field is given as a function of UT time for the date of September 12, 1990. The local magnetic latitude, the magnetic latitude and the L value are given in hourly intervals.

SOURCE: Kletzing et al. (2013).

3.1.5.5 Ultra low frequency waves

Ultra Low Frequency (ULF) waves are in the frequency range of 2 to 5000 millihertz (mHz), as shown in Table 3.3. They are excited at the magnetopause contours in response to shear velocity (CLAUDEPIERRE et al., 2008) or dynamic pressure fluctuations of the solar wind (CLAUDEPIERRE et al., 2009; UKHORSKIY et al., 2006). They can also be excited by natural instabilities in the magnetospheric plasma (THORNE, 2010). ULF wave measurements can be made by equipment on board satellites or monitored on the ground by magnetometers. The characteristics of the

wave spectrum are used to analyze its occurrence, intensity and to determine the radial diffusion coefficients (BRAUTIGAM et al., 2005). Resonance with the field line is a particular class of ULF waves. The waveform is quasi sinusoidal and persists for long periods and is considered continuous. They may be associated with the constant presence of Alfvén waves traveling along geomagnetic field lines. The magnetosphere edges oscillate coherently with disturbances in the azimuthal direction. Toroidal waves have been associated with an electric field induced in the radial direction. The poloidal mode oscillation is characterized by magnetic compression disturbances and electric field induced in the azimuthal direction (HUGHES, 2013).

Table 3.3 - ULF waves frequency range

Regular		
Notation	**Period(sec)**	**Frequency**
Pc1	0.2 - 5	200mHz a 5Hz
Pc2	5 - 10	100 mHz a 200 mHz
Pc3	10 - 45	22 mHz a 100 mHz
Pc4	45 - 150	7 mHz a 22 mHz
Pc5	150 - 600	2 mHz a 7 mHz
Irregular		
Pi1	1 - 40	25mHz a 1Hz
Pi2	40 - 150	7mHz a 25mHz

SOURCE: Adapted from Jacobs et al. (1964).

ULF waves can be both broadband and quasi sinusoidal, and can be caused by either internal processes, that is, within the magnetosphere, or external processes occurring in the solar wind (ELKINGTON, 2013).

Examples of an internal source are instabilities in the drift of the cold plasma population in the internal magnetosphere and also anisotropy in the ring current. The velocity shear along the magnetopause boundary also promotes the occurrence of ULF waves in the magnetosphere. The external source is related to the solar wind in the form of transmission of variations in the solar wind dynamic pressure to the magnetosphere, allowing the flow of energy in the form of compression waves that can be coupled with poloidal or toroidal resonance mode in the inner geomagnetic field lines. Another form of ULF waves generation is related to changes in the large-scale convective movement of the magnetosphere associated with global rates of

reconnection and solar flux around the magnetopause.

More important than the generation of ULF waves is their effect on the radiation belts. Wide amplitude oscillations in the Pc-5 range are associated with an increase in the relativistic electrons flux when compared to low amplitude events.(MATHIE; MANN, 2000) evaluated 17 storms and observed that the electron flow increased only where ULF waves were sustained at high levels for days after the geomagnetic storm. They found a strong correlation between the speed of the solar wind above 450 km/s and the long duration of Pc-5 wave activity during the recovery phase as a determining factor for the production of relativistic electrons.

ULF waves can cause transport by radial diffusion. The rate of radial transport is dependent on the power density of the wave spectrum and tends to be much faster in the outer magnetosphere (KLETZING et al., 2013). MHD simulations as well as observational data have been important to determine the radial diffusion rates.

Electromagnetic ion cyclotron waves are considered to be Pc1-2 ULF waves but they are discussed in detail in the next section 3.1.5.6.

3.1.5.6 Electromagnetic ion cyclotron waves

Electromagnetic ion cyclotron (EMIC) waves are discrete electromagnetic emissions in distinct frequency bands separated by multiple ion gyro frequencies. They are often observed on the ground and in *in situ* satellites measurements in the ULF Pc1-2 frequency range, that is, from 0.1 up to 5 Hz. EMIC waves source region is typically confined to ~ 11 degrees of latitude about the geomagnetic equatorial plane and they shown bidirectional propagation. The high latitude propagation wave can be determined by the Poynting vector which is always in reverse direction towards the equator (LOTO'ANIU et al., 2005).

EMIC waves usually propagate in three bands below the proton gyrofrequency (Ω^+): H^+-band between Ω_{He+} and Ω_{H+}, He^+-band between Ω_{O+} and Ω_{He+} and finally O^+-band below Ω_{O+}. The hot (10-100 keV) and anisotropic ($T_\perp > T_\parallel$) ions are responsible for their generation (KENNEL; PETSCHEK, 1966). The composition of ions and their anisotropy, together with the activity levels of the geomagnetic field, influence which bands will be excited. EMIC waves are traditionally transverse fluctuations, left-hand polarized about the magnetic field line. Eventually, EMIC waves can be observed linearly polarized and right-handed polarized, containing a weak parallel component. The multi-ion plasma affects the dispersion relation and results in dif-

ferent wave polarization which led them to also become oblique (RAUCH; ROUX, 1982; THORNE; HORNE, 1997; FRASER et al., 1989; HU et al., 2010; SAIKIN et al., 2015, e.g.). They can propagate away from their source region of minimum magnetic field strength to areas of high magnetic field (MAUK; MCPHERRON, 1980).

The resonant interaction with electrons requires intense Doppler shift, which can even change the direction of the electron propagation. At zero pitch angle, resonance can occur at energies less than 0.5 Mev. However, at high energies, a high pitch angle is necessary, therefore, the increase in the resonance range is proportional to the increase in energy. Resonant pitch angle scattering and proton precipitation from the ring current by EMIC waves on the plasma plume at the dayside region are directly associated with observations of sub-auroral proton arcs (SAKAGUCHI et al., 2008). EMIC waves are also responsible for the resonant scattering of relativistic electrons leading to rapid loss during the main storm phase (BORTNIK et al., 2006; LYONS; THORNE, 1972; SUMMERS; THORNE, 2003; SUMMERS et al., 2007; JORDANOVA et al., 2008) and they are intensified during geomagnetic storms.

EMIC waves can cause pitch angle scattering and loss of ring current ions (JOR-DANOVA et al., 2001) and relativistic electrons (above 0.5 MeV) during the phase propagation. (THORNE; KENNEL, 1971; LYONS; THORNE, 1972; SUMMERS; THORNE, 2003; SUMMERS et al., 2007; JORDANOVA et al., 2008; SAIKIN et al., 2016; HALFORD et al., 2016). Regions favorable to EMIC excitation include the overlap between the ring current and the plasmasphere, the dayside of the drainage plume, and the outer side of the magnetosphere in association with fluctuations in solar wind dynamic pressure (THORNE, 2010). They can be found in several MLT and *L*-shells regions (ANDER-SON et al., 1992; HALFORD et al., 2010; MIN et al., 2012; USANOVA et al., 2012; SAIKIN et al., 2015; HALFORD et al., 2016). Their peak occurrence rate has been reported to be around the afternoon MLT sector between ~ 12 and ~ 18 MLT (ANDERSON et al., 1992; KASAHARA et al., 1992; HALFORD et al., 2010; MIN et al., 2012; USANOVA et al., 2012; USANOVA et al., 2013; KEIKA et al., 2013; MEREDITH et al., 2014; WANG et al., 2015; SAIKIN et al., 2015).

Figure 3.12 shows the presence of EMIC waves observed by the EMFISIS instrument on board the Van Allen Probes A on September 24, 2013. The XYZ components of the magnetic field in GSM coordinates were measured at high resolution (64 Hz) over UT time, MLT, magnetic latitude and the *L*-shell location. The wave power is given in units of nT^2/Hz. The white lines show the gyro frequency for Helium ions (above) and Oxygen (below). The fourth frame shows the geomagnetic index

SYM-H and in the last frame, the magnetic field strength obtained from the same equipment. The blue dashed line shows the start of the EMIC waves.

Figure 3.12 - EMIC wave spectrogram.
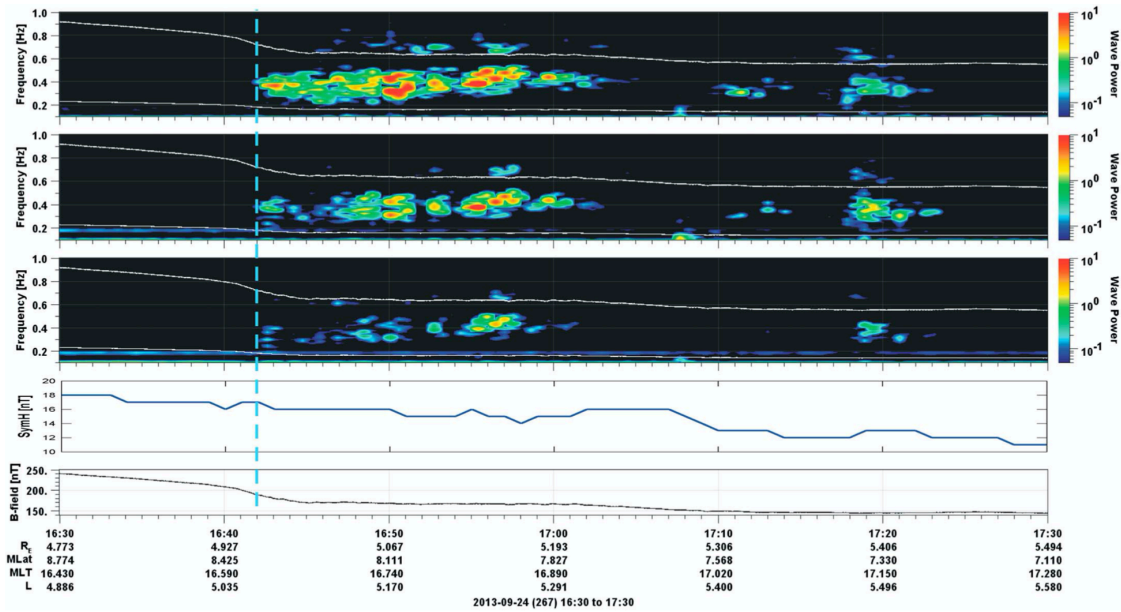
The first three panels show the spectrogram of the three components of the magnetic field in GSM coordinates obtained from the EMFISIS instrument on board the Van Allen Probes A on September 24, 2013. The wave power is given in units of nT^2/Hz. The white lines show the Helium gyrofrequency (above) and Oxygen gyrofrequency (below). The fourth panel shows the geomagnetic index SYM-H and the bottom panel presents the magnetic field. The blue dashed line shows the beginning of the EMIC waves.

SOURCE: Rodger et al. (2015).

Meanwhile, EMIC waves cause a huge impact on the particle populations in the inner magnetosphere especially on relativistic electrons in the Van Allen radiation belts. It has been intriguing to the scientific community to understand the dynamics of energetic electrons (above 1 MeV) (BAKER et al., 2013; SHPRITS et al., 2016; XIAO et al., 2015). Long-term modeling has shown the needs of EMIC waves to be included in the simulations since the electron fluxes above 3.6 MeV appeared to be overestimated without EMIC waves scatter contribution (DROZDOV et al., 2015; SHPRITS et al., 2016). Observational studies confirmed that energetic electron (above 0.5 MeV)

precipitation into the atmosphere can occur due to EMIC waves. They were based on EMIC waves detection on ground and *in situ* satellites associated with measurements of ultrarelativistic electrons detected by ballons, polar satellites and riometers (BLUM et al., 2015; CLILVERD et al., 2017; CLILVERD et al., 2015; MIYOSHI et al., 2008; RODGER et al., 2008; RODGER et al., 2015). Usanova et al. (2014) and Aseev et al. (2017) showed the contribution of EMIC waves to change the pitch angle distribution of relativistic electrons trapped on the Van Allen radiation belt using Van Allen Probes measurements and ground-based observations. They suggested a correlation between the occurrence of EMIC waves and narrowing of the normalized pitch angle distributions, near 0° up to 30°, which is a signature of EMIC wave-induced precipitation. It provided a pitch angle distribution shape on which the peak , not so pronounced, became pronounced at 90° and the flux vanished when approaching 0°.

Medeiros et al. (2019), on the other hand, suggested that EMIC waves could change the regular electron butterfly PAD shape, which is characterized by two local maxima commonly found nearby 45° as 135° and a local minimum at 90°, to a peculiar electron butterfly PAD shape wherein the just mentioned two local maxima are displaced toward pitch angles near 90°. In fact, this thesis work is mostly concerned about how frequent such peculiar electron butterfly PAD shapes are and if they are indeed associated with EMIC waves occurrence. More on that in the following chapters. As mentioned before, geomagnetically disturbed times can contribute to EMIC waves occurrence (BORTNIK et al., 2006; LYONS; THORNE, 1972; SUMMERS; THORNE, 2003; SUMMERS et al., 2007; JORDANOVA et al., 2008; SAIKIN et al., 2016; HALFORD et al., 2016) and references therein).

One of the well known phenomena usually present during geomagnetic storms is the dayside magnetopause compression and drift-shell splitting (SIBECK et al., 1987). When the magnetopause compression is stronger enough to provide loss of particles to the adjacent magnetosheath region, breaking the third adiabatic invariant, the electron pitch angle distribution generally presents a butterfly shape (WEST JUNIOR et al., 1973; HORNE; THORNE, 2003; GANNON et al., 2007). Butterfly PAD shape is usually explained in terms of drift shell splitting due to local time asymmetry in the Earth's magnetic field (ROEDERER; SCHULZ, 1971; SIBECK et al., 1987). On the nightside region particles at 90°pitch angle move inward to lower geocentric distances, leaving a deficit of 90°pitch angle particles which is not rectified by particles moving inward from greater radial distances due to the negative radial flux gradient (SIBECK et al., 1987). Medeiros et al. (2019), argued the attributed the loss of particle noticed by PAD reduction near 0° and 180° to EMIC waves occurrence immediately

after the stronger compression of the magnetopause on September 12, 2014, in addition to magnetopause shadowing and drift shell splitting. A reconfiguration of the butterfly PAD shape in which both peaks seemed to move from close to 45°(150°) to approximately 35°(135°) resulting in a peculiar butterfly PAD shape, as already mentioned above.

It was necessary to investigate properly how recurrent the peculiar butterfly PAD shape appears. This study was born in this sense: to find evidence of peculiar electron butterfly PADs associated with EMIC waves.

3.2 Summary

The presence of waves in the magnetosphere has been studied for decades and recent technological advances as well as the development of models have improved our knowledge about how they interact with particles within the Van Allen radiation belts. Different types of waves are excited in the magnetosphere during geomagnetically active periods promoting changes in the radiation belt by either adiabatic or non-adiabatic processes. EMIC, chorus and plasmaspheric hiss waves can cause pitch angle scattering and loss to the Earth's atmosphere. Interactions with chorus waves can also promote local electron acceleration. ULF waves can cause radial diffusion and energize particles by radial transport to the inner magnetosphere. ECH waves scatter electrons in the low density region of the plasmapause. The evolution in the study of wave-particle interaction relies on the improvement of instruments on board satellites in addition to the development of models that can reproduce the behavior of the magnetosphere. An excellent advance in the study of waves in the Van Allen belts occurred in the last 7 years with the launch of the Van Allen Probes mission, which was formerly known as Radiation Belts Storm Probes. This dataset mission is used in this thesis and it will be presented in the next chapter.

4 DATASET DESCRIPTION

In situ data at the Van Allen Belts region were provided by the twin Van Allen Probes designed to observe both the inner and outer radiation belts from 1 Re to nearly 5.8 Re. In this Chapter, it is briefly presented the Van Allen Probe mission, three major instruments onboard the spacecraft, and their dataset which support the thesis development.

4.1 Van Allen probes mission

The main goal for the Van Allen Probes mission was *"Provide understanding, ideally to the point predictability, of how populations of relativistic electrons and penetrating ions in space form or change in response to variable inputs of energy from the Sun"*(MAUK et al., 2012).

Therefore, it was developed two satellites in such a way to obtain measurements namely distant temporal and spatial simultaneously in a high quality operational system onboard satellites. The named Van Allen Probes mission were two similar satellites containing identical equipment, following the same geocentric orbit, with perigee near 600 km and apogee around 5.8 Earth radii. Their inclination orbit was about 10 degrees and during it, they crossed the entirely Van Allen radiation belts inclusive the slot region. The precession orbit was clockwise from the polar north view and, from this point of view, from the apogee location rounds 210 degrees per year, thus a total precession in about 18 months. Their lifetime was estimated in two years in order to cross the nightside at the apogee at least 2 times in this interval. Fortunately the satellite reached the duration of more than seven years. They were launched on August 30, 2012 and both RBSP-B and RBSP-A were moved to de-orbiting on July and on October, 2019, respectively. Each 75 days they overpass each other and during these intervals they could vary their distance from 100 km to 5 Earth radii. On average, both measured the same region with a time difference from minutes to 4.5 hours. The orbital cadence was nine hours which meant they developed up to three orbits per day. Particles trapped $\pm 21°$ magnetic latitude could be covered due to Earth orbit inclination and the spacecraft orbit inclination itself (MAUK et al., 2012).

The spin axis was nominally sunward oriented at five rotation per minutes (5RPM) and their position, near the magnetic equator of the quasi-dipolar magnetic configuration, allowed the particle detectors to obtain an overview of the complete pitch angle distribution twice for every spin orbit as well as to measured the dawn/dusk

electric field. In order to guarantee it, the spacecraft were realigned each 21 days leading the spin axis is always maintained to lie within 27 of the sun's direction (MAUK et al., 2012).

4.1.1 The relativistic electron-proton telescope

The REPT instrument was built to measure, in detail, the directional intensities and energy spectra of near 1 up to 10 MeV electrons along the slot region and the outer Van Allen radiation belt. The REPT sensors contained a large geometric factor to distinguish the higher energy from the background noise at the same it needed to not saturate at the lower energies. It was also designed to measure very high-energy proton populations. In this sense, it was possible to obtain detailed pitch angle information and directional electron intensity at each spatial location near-equatorial. More details about the instrument designer can be obtained in (BAKER et al., 2013). The ECT Science Operation Center (SOC) at the Los Alamos National Laboratory (LANL) is responsible for the processing and disseminating the data, including post processing dataset into higher level products which combines several informations together. In this study was used Level 3 data which incorporates the geomagnetic field direction and thus provides the pitch angle information. The REPT instrument provides pitch angle–resolved differential electron fluxes in 12 energy levels (1.80 up to 59.45 MeV) in 17 different pitch angle bins (5.3°, 15.9°, 26.5°, 37.1°, 47.6°, 58.2°, 68.8°, 79.4°, 90.0°, 100.6°, 111.2°, 121.8°, 132.4°, 142.9°, 153.5°, 164.1°, 174.7°). The REPT dataset, for a small interval (September 12,2014) is present in the case study, Chapter 3.1.5.6, in order to investigate the magnetopause shadowing, drift-shell splitting, and EMIC waves effects on the pitch angle distribution for these energy ranges. The dataset is also used, in Chapter 7.2.1, to explore a long time interval (January 2014 to October 2015), to investigate the pitch angle distribution shapes.

4.1.2 The magnetic electron ion spectrometer

The Magnetic Electron Ion Spectrogram(MagEIS) instruments were onboard both the Van Allen Probes. They were four magnetic spectrometer units: one low-energy(20-240 keV), two medium energy(80-1200 keV), and a high energy (800-4800 keV). In addition there was a proton telescopy (55 keV-20 MeV). The main target was to measure the differential fluxes, energies, and angular distributions of electrons from 20 keV to 5 MeV. More details about the instrument designer can be obtained in (BLAKE et al., 2013). The ECT Science Operation Center (SOC) at the Los Alamos National Laboratory (LANL) is responsible for the processing and disseminating the data, including post processing dataset into higher level products which combines

several informations together. MagEIS instrument provided us electron observations for 25 energy levels (20 keV up to 4.80 MeV) in 11 different pitch angle bins (8.2°, 24.6°, 40.9°, 57.3°, 73.6°, 90.0°, 106.4°, 122.7°, 139.1°, 155.5°, 171.8°). The MagEIS dataset is present in Chapter 3.1.5.6 in order to investigate the magnetopause shadowing, drift-shell splitting and EMIC waves effects on the pitch angle distribution for these energy ranges.

4.1.3 Electric and magnetic field instrument suite and integrated science

The EMFISIS instrument measures DC magnetic fields and a comprehensive set of wave electric and magnetic fields. It covers the frequency range from 10Hz up to 12 Hz (for single-axis electric field it reaches 400 kHz). There are two similar instruments and each one of them is onboard the Van Allen Probes spacecraft. They comprise two sensors: a tri-axial fluxgate magnetometer (MAG) and a tri-axial magnetic search coil magnetometer (MSC). The magnetometer boom sensors are mounted 3 m far from the spacecraft body in order to minimize interferences. More details about the instrument design can be obtained in (KLETZING et al., 2013).

The dataset time-resolution used here is 64 samples (vectors) per second, or 64 Hz. All dataset is publicly available online and in different coordinate systems, and in this study it is used the geocentric solar magnetospheric (GSM) coordinate system. They are time-tagged in daily packets and are associated with spacecraft location. Figure 4.1 shows an example of 1 hour and 10 minutes of high resolution magnetic field data from October 31, 2013 for RBSP-A spacecraft near the apogee. The three components are in the GSM coordinate system. Also, information of the spacecraft's geocentric distance (R_E), magnetic latitude (MLat), magnetic local time (MLT), and L-shell (L) are shown.

Figure 4.1 - RBSPA/EMFISIS Magnetometer vector.
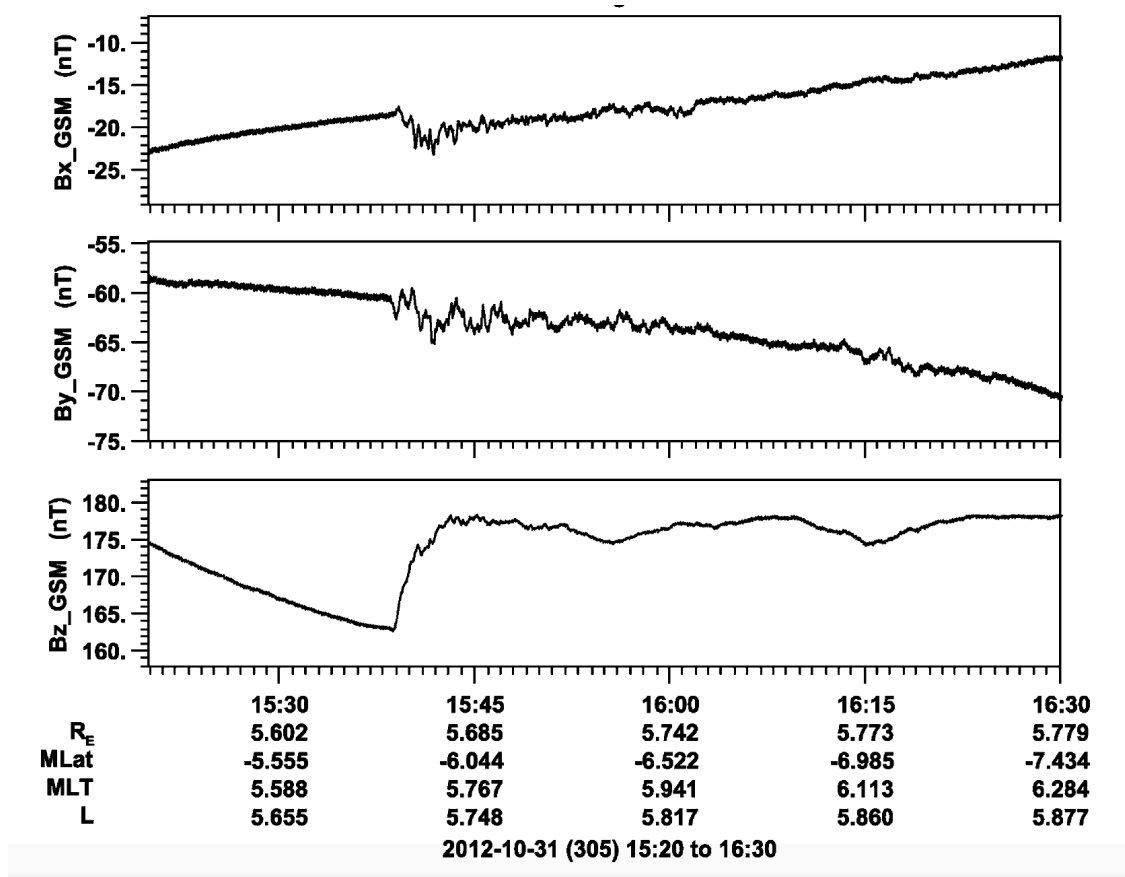
Example of MAG data from the RBSP-A spacecraft on October 31, 2012 in GSM coordinates.

SOURCE: Kletzing et al. (2013).

The primary method of access to the EMFISIS data is the web server located at http://emfisis.physics.uiowa.edu/. All data products are in the ISTP-compliant Common Data Format (CDF) format. More details can be found at the NASA Space Physics Data Facility website https://spdf.gsfc.nasa.gov/. The EMFISIS dataset is present in Chapters 3.1.5.6 and 6.1 in order to support EMIC waves surveys.

5 REVIEW: ON THE CONTRIBUTION OF EMIC WAVES TO THE RECONFIGURATION OF THE RELATIVISTIC ELECTRON BUTTERFLY PITCH ANGLE DISTRIBUTION SHAPE ON 2014 SEPTEMBER 12 - A CASE STUDY

In this chapter it is presented a review from the paper *"On the Contribution of EMIC Waves to the Reconfiguration of the Relativistic Electron Butterfly Pitch Angle Distribution Shape on 2014 September 12—A Case Study"* (MEDEIROS et al., 2019). This paper is the starting point to the thesis proposed here.

On September 12, 2014 a long-term electron flux dropout was observed by the twin Van Allen Probes. It occurred concomitantly with the arrival of two interplanetary coronal mass ejections (ICMEs) that strongly compressed the dayside magnetopause promoting the loss of relativistic electrons in the outer radiation belt as investigated by Jaynes et al. (2015), Alves et al. (2016), Ozeke et al. (2017). The major cause for the dropout, according to these authors, is magnetopause shadowing followed by drift-shell splitting and wave-particle interactions mediated by coherent whistler mode chorus and ULF waves. Electromagnetic ion cyclotron (EMIC) wave, has not been considered for this event by the aforementioned studies even noticing that it is an important mechanism to scatter relativistic electrons into the loss cone (SUMMERS et al., 2007; SHPRITS et al., 2009; USANOVA et al., 2014; LI et al., 2014; ZHANG et al., 2016a; CLILVERD et al., 2017).

5.1 Electron flux dropout

Medeiros et al. (2019) presented similar findings according to the iCME's magnetic field and plasma parameters and the dropout of the relativistic electrons. Figure 5.1(a), shows relativistic electron flux at 2.00 MeV in a 48 hr interval from 12:00 UT on September 11 up to 12:00 UT on September 13, 2014. RBSP-B spacecraft apogee was located between nightside and dawnside region. Figure 5.1 also presents: (b) IMF north–south B_Z and east–west B_Y (xzGSM) components, (c) the solar wind's proton speed, (d) solar wind's dynamic pressure, and (e) the geomagnetic Dst index. On September 12, two interplanetary shocks reached the magnetosphere, as seen by the increase in the solar wind parameters (00:00 UT and 16:00 UT). The second shock was stronger and preceded the major relativistic electron flux decrease. The dropout started about one hour after the major increase in the dynamic pressure, accompanied by a sudden enhancement in the solar wind speed V_{SW} and number density (not shown), with the latter reaching around $20 cm^{-3}$. The Dst index, as shown in Figure 5.1(e) confirmed the geomagnetic disturbances, as shown by the

two abrupt positive increases followed by the corresponding negative decreases that
reached around −40 and −85 nT.

Figure 5.1 - Radiation belts and interplanetary conditions during 2014 September 11–13.
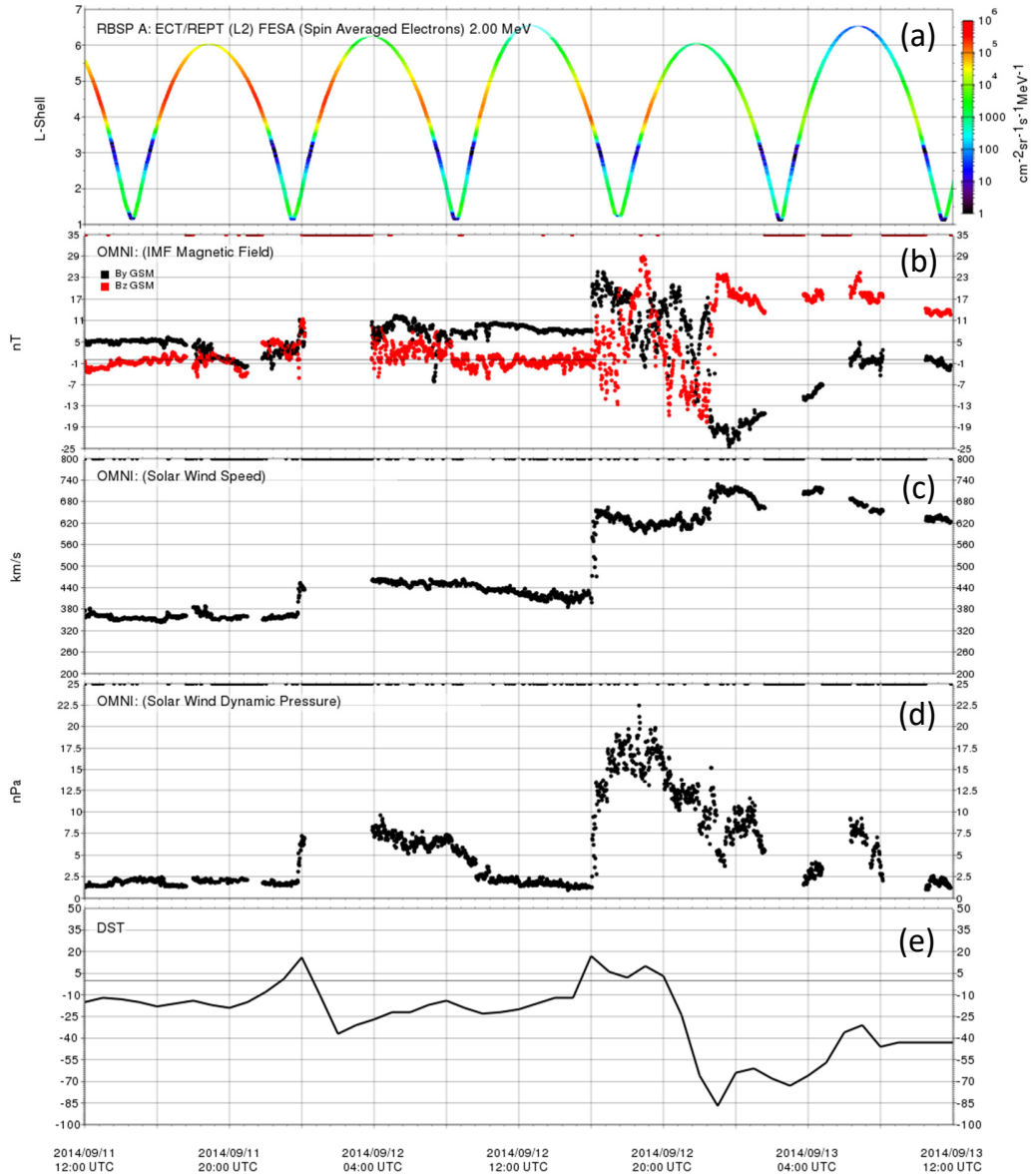
(a) Relativistic Electron Flux at 2.00 MeV channel according to L-shell during the period,
(b) Interplanetary magnetic field components B_Z (red dots) and B_Y (black dots). (c) Solar
wind proton speed component V_X, (d) dynamic pressure, and (e) Dst index.

SOURCE: Medeiros et al. (2019).

5.1.1 Investigating the dropout using global MHD simulation

The geomagnetic field response to solar wind variations was investigated using the Space Weather Modeling Framework/Block-Adaptive-Tree Solar-wind Roe-type Upwind-Scheme (SWMF/BATS-R-US) global MHD code (TÓTH et al., 2012) coupled with the Rice Convection Model (RCM) (ZEEUW et al., 2004; MEDEIROS et al., 2019). The results show a dayside magnetopause compression when the ICME reached the Earth's magnetopause. Figures 5.2(a), (c), and (e) present the SWMF/BATS-R-US current density magnitude in the xzGSM plane, and the (b), (d), and (f) panels show an equatorial view of the Earth's magnetosphere. The black line in panels (b), (d), and (f) indicate the dayside magnetopause boundary. It was obtained by taking the first maximum along radial profiles of modeled current density magnitude. The color-coded lines represent contours of constant magnetic field strength ranging from 100 to 300 nT (red to blue). They are quite similar to drift paths of equatorially mirroring electrons.

Before the interaction with the ICME there is no significant change on the magnetopause contour in comparison with the isocontour lines (5.2 a and b). The maximum compression occurred at 16:15 UT (panels (e) and (f)). Figure 5.2(f) shows the intersection of the red isocontour of 100nT equatorial magnetic field strength by the magnetopause (black line), suggesting that equatorially mirroring particles drifting along the outer-most magnetic field strength contour reach the dayside magnetopause boundary, therefore favoring the magnetopause shadowing scenario.

Figure 5.2 - Global (MHD) simulation of the Earth's magnetosphere on the arrival of the ICME on September 12, 2014.
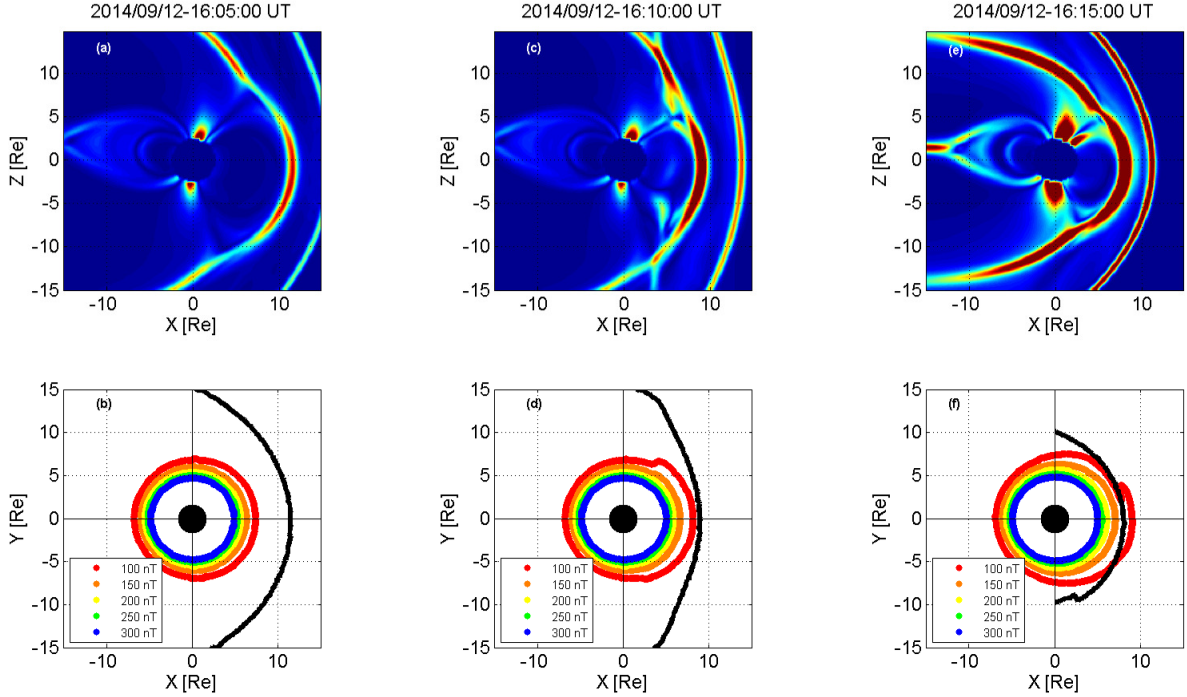
Instantaneous images of magnetospheric current density magnitude values (in units of $\mu A/m^2$) extracted from the SWMF/BATS-R-US coupled with RCM model at the X-Z_{GSM} in the meridional plane (a,b) prior to the ICME arrival, (c,d) at the ICME arrival, and (e,f) during the maximum magnetosphere compression. Panels (b,d,f) show equatorial (X-Y_{GSM}) cuts of the modeled magnetosphere at these instants of time. Color-coded lines in panels (b), (d), and (f) indicate magnetic field strength isocontours for different intensities (100 up to 300 nT) as extracted from the SWMF/BATS-R-US output. The black line on those panels represents the location of the magnetopause boundary in the dayside equatorial region (see text for details).

SOURCE: Medeiros et al. (2019).

5.1.2 The dropout according to the PAD shape

Magnetopause shadowing and drift shell splitting are usually associated with a butterfly PAD-shape, since they are expected to promote a local minimum flux at 90° pitch angle and two local maxima usually at pitch angles 45° and 135° (WEST JUNIOR et al., 1973; SIBECK et al., 1987; SELESNICK; BLAKE, 2002; HORNE; THORNE, 2003; GANNON et al., 2007). Following this issue Medeiros et al. (2019) investigated

pitch angle-resolved electron fluxes from both MagEIS and REPT instruments. Figures 5.3 and 5.4 show a 2.5 hr interval of electron PADs spanning a wide range of energies ($\sim 32- \sim 3400$ keV) as provided by both the MagEIS-B and REPT-B instruments. The presence of butterfly-shaped PADs is clearly evident for electron energies above 170 keV at around 18:30 UT. For higher energies the butterfly-shaped PADs are detected earlier, since they are expected to be lost sooner (either to the magnetopause boundary or the Earth's upper atmosphere).

5.1.2.1 Drift shell splitting

The permanent solar wind pressure and the magnetotail plasmasheet distort the magnetic field which led the magnetic field strengths to be greater than the magnetic field in the same radial distance in the nightside region. Considering a spacecraft measuring particles in a constant radial distance. The particle fluxes measured were lower in the same radial distance if you are in the nightside region than in the dayside region. It happens to conserve the adiabatic invariant for the drift particle motion that are trapped near the equator. Particles move radially outward while drifting from midnight to noon and radially inward when drift from noon to midnight (SIBECK et al., 1987; ROEDERER, 1967). Particles that are far from the equator developed a more circular paths because they do not follow the same constant magnetic field strength. Due to these differences, the measurements of particle fluxes on the nightside region can reproduce a butterfly PAD shape promoting the flux decrease near 90°and increase in pitch angles far from 90°. Kennel e Petschek (1966) noticed the favorable region for butterfly is the nightside once interaction with ion cyclotron waves were barely reported in this region. If so, the particles at pitch angles near the loss cone would be scattered to the loss cone and the 90-degree PAD shape will be predominant. Nevertheless, this thesis provides some evidences of the interaction of EMIC waves can indeed scatter particles into loss cone even in this region but keeping the butterfly PAD shape, in an unusual reconfiguration.

Figure 5.3 - MagEIS-B pitch angle distribution.
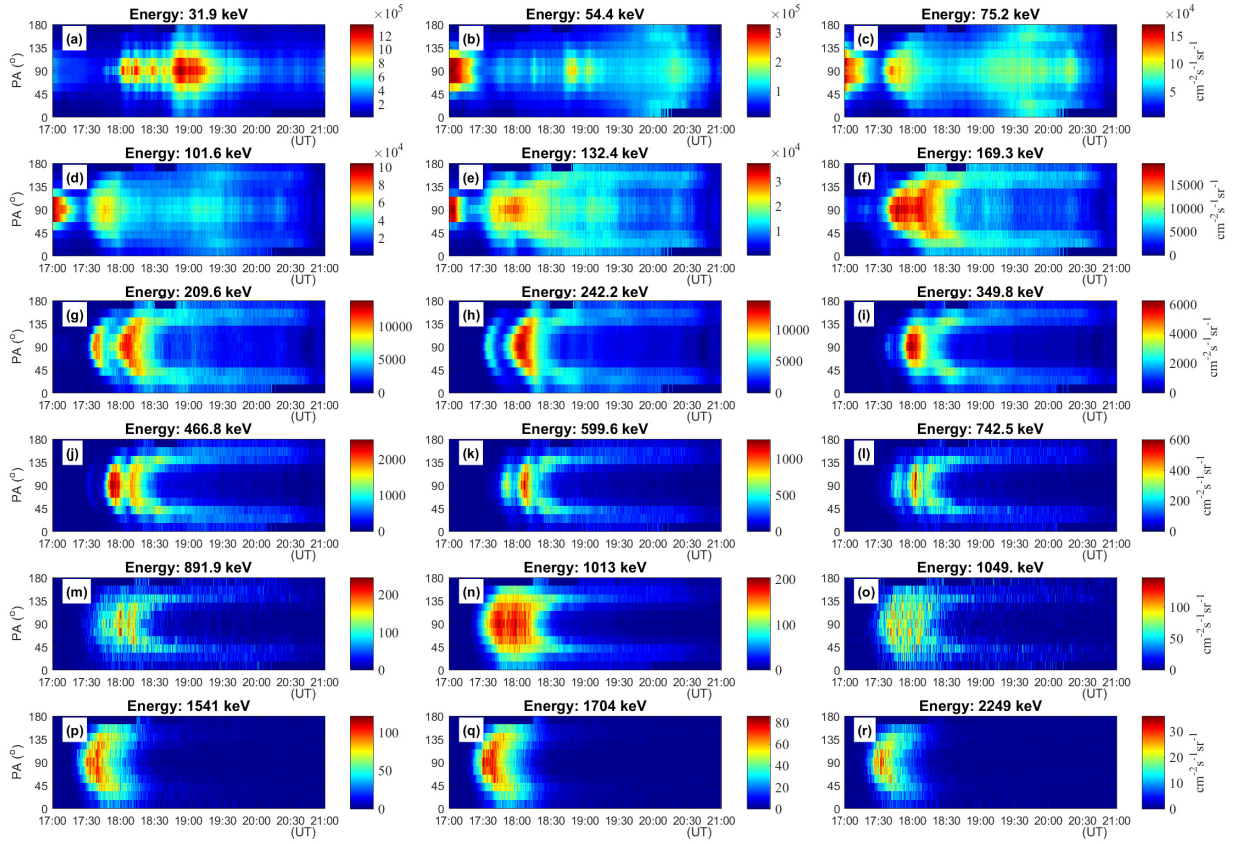
MagEIS-B pitch angle distribution on September 12, 2014 from 17:00 to 21:00 UT at 31.9 keV to 2249 keV energy channels. Before the magnetopause compression (∼17:30 UT), all energy levels presented 90°-peaked PAD shapes. Afterwards, only energies above ∼132 keV presented butterfly PAD shape shown here as the dropout in the electron flux at 90° pitch angle.

SOURCE: Medeiros et al. (2019).

Figure 5.4 - REPT-B pitch angle distributions.
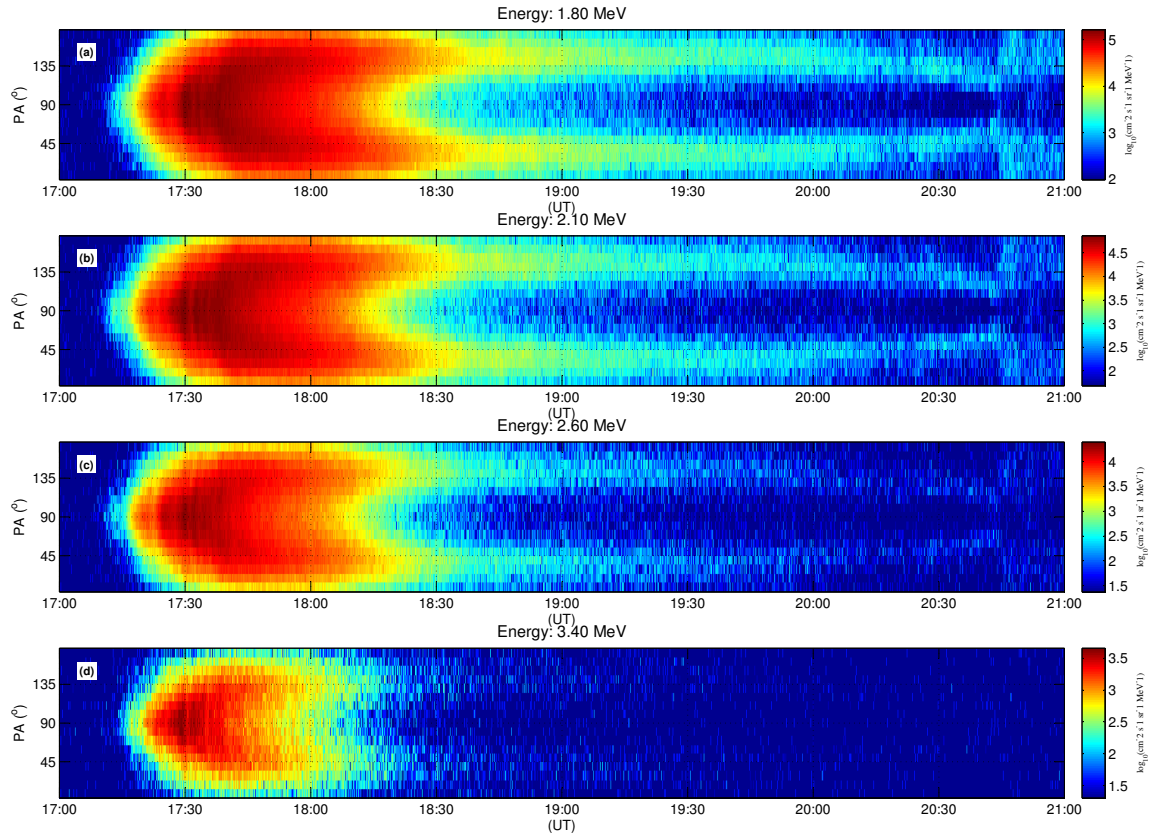
REPT-B pitch angle distributions on September 12, 2014 from 17:00 to 21:00 UT at 1.80 MeV to 3.40 MeV energy channels. Before the magnetopause compression (~17:30 UT), all energy levels presented 90°-peaked PAD shapes. Afterwards, as the magnetopause compression progressed, the PAD shapes gradually changed to butterfly-like shapes which are evidenced here by a local minimum flux at 90° pitch angle.

SOURCE: Medeiros et al. (2019).

There is evidence for a transition in the PAD shape, and it can be determined quantitatively by the dimensionless r parameter presented in Equation 5.1. Such a parameter has been used by Gannon et al. (2007) to classify distinct PAD shapes. The r parameter 5.1:

$$r = \frac{flux_{90°}}{\left(\dfrac{flux_{\sim 45°} + flux_{\sim 135°}}{2}\right)}. \tag{5.1}$$

To calculate the r parameter, one uses the measured particle flux at pitch angle bins closest to 90°, 45°and 135°. Medeiros et al. (2019) used the REPT (MagEIS) instrument that provides differential pitch angle-resolved fluxes in 17 (11) pitch angle bins. We used the REPT pitch angle bins at 90°, 47.6°and 132.4°, and the MagEIS bins at 90°, 40.9°and 139.1°to calculate r from Equation 5.1. To classify distinct PAD shapes, we used the criteria: whenever $0.9 \leq r \leq 1.1$ the PAD is considered to have a flattop shape, whereas when $r > 1.1$ ($r < 0.9$) it has a 90°-peaked (butterfly) shape (GANNON et al., 2007). Figures 5.5 and 5.6 show electron PADs acquired from MagEIS-B and REPT-B data, respectively, where the suffix "-B" refers to instruments onboard RBSP-B. The r parameter is calculated in two time instants T_1 and T_2 (detailed in each panel) to show that the electron PAD shape indeed underwent a transition from 90°-peaked ($r > 1.1$) to butterfly ($r < 0.9$), as seen in panels (e)–(h), (m)–(p), and (u)–(x) of Figure 5.5, and panels (e-h) in Figure 5.6. Such a transition has been observed for a wide energy range, which confirms electron loss via magnetopause shadowing (MEDEIROS et al., 2019). To determine instants T_1 and T_2, time series of electron fluxes at 90° pitch angle have been used. T_2 corresponds to the time when the maximum flux intensity prior to the dropout decreased by 80% (roughly $1/e^2$). In what follows, it is described how to select the times T_1 and T_2 . The blue circles in Figures 5.5 are the pitch angle–resolved differential electron fluxes from MagEIS-B at different energy levels (from 169.3 to 1,704 keV). A black line was overplotted on each of these panels, and each black line corresponds to the fitted curve obtained by the 3-Gaussian function shown in Equation 5.2 below:

$$f(t) = \sum_{i=1}^{3} a_i \exp\left[-\left(\frac{t - t_i}{c_i}\right)^2\right], \tag{5.2}$$

where a_i, t_i and c_i are the fit parameters, and subscript i indicates the number of peaks to fit. There are two distinct time instants denoted by T_1 and T_2. The former corresponds to the time when the fitted flux achieves a global maximum within the analyzed interval, and the latter to the time when this maximum fitted flux decreased 80% . Figure 5.7 presents the times T_2 when electron fluxes at 90°pitch angle drop by 80% as a function of energy. The electron flux dropout at a 90°pitch angle occurs

first for higher-energy electrons, as also shown in Figures 5.5(e)–(r) and 5.6. It is pointed out that only electrons at energies equal to or above ~ 160 keV exhibit an expressive decrease in the electron flux, while at lower energies a sustenance in the measured fluxes was detected, particularly at 90°pitch angles (5.5(a)–(d)).

Figure 5.5 - MagEIS-B before and during the electron flux dropout.
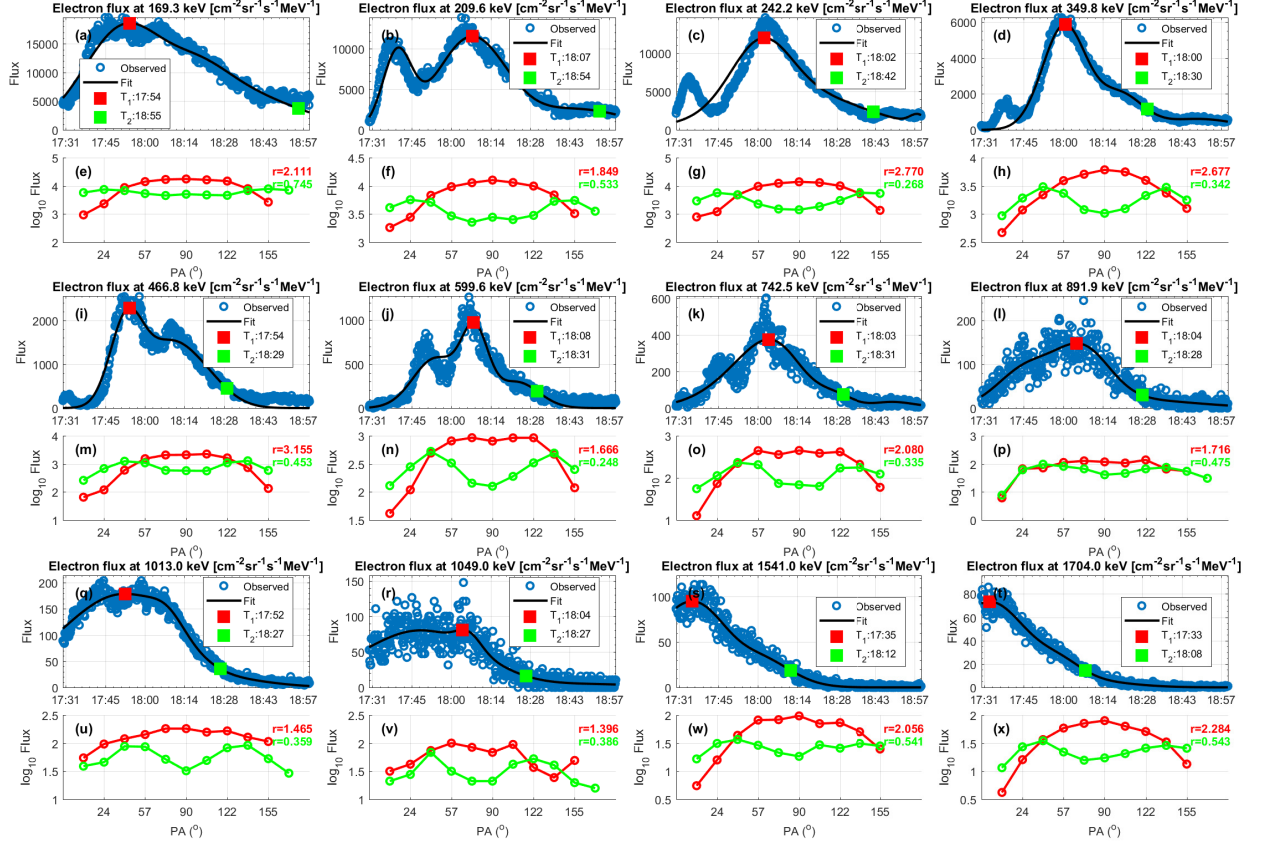
Comparison between pitch angle-resolved electron fluxes before (T1) and during (T2) the electron flux dropout on September 12, 2014. Panels (a-d), (i-l), and (q-t) present a 90 minutes interval (17:30 UT to 19:00 UT) of MagEIS-B electron fluxes (blue circles) at 90° pitch angle for several energy channels ranging from 169.3 keV to 1704.0 keV. A Gaussian-like fit (see text for details) was also superposed (black curve) onto these plots. The time T1 corresponds to the maximum fitted flux value, whereas T2 when the flux drops to 80% (roughly $1/e^2$) of this maximum value. The corresponding electron pitch angle distributions (PADs) at these two time instants are shown as red and green curves, respectively, in panels (e-h), (m-p), and (u-x). At T1 (T2) the electron PADs have a 90°-peaked (butterfly) shape, as evidenced by the r parameter which provides the ratio between the flux at the 90° pitch angle bin to the average flux at both 40.9° and 139.1° pitch angle bins. It is defined that whenever r>1.1 (r<0.9) the analyzed electron PAD has a 90°-peaked-like (butterfly-like) shape (see text for details).

SOURCE: Medeiros et al. (2019).

58

Figure 5.6 - REPT-B before and during the electron flux dropout.
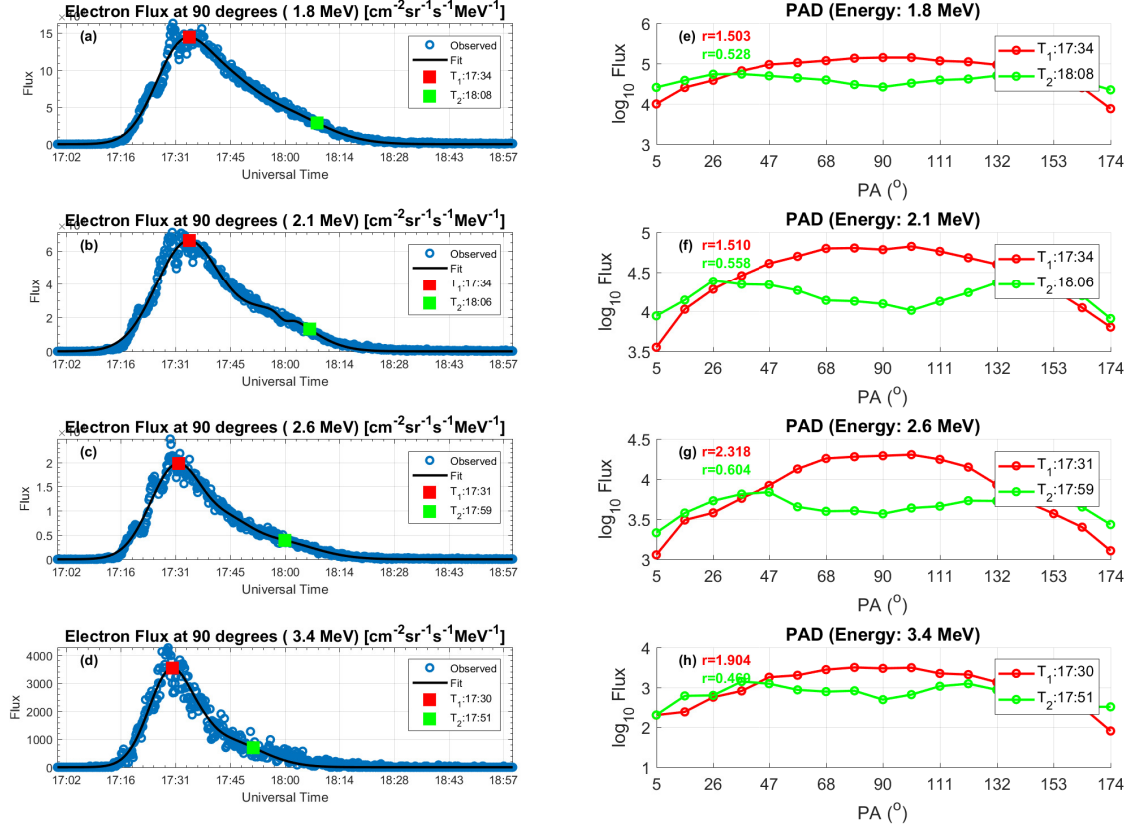
Comparison between pitch angle-resolved electron fluxes before (T1) and during (T2) the electron flux dropout on September 12, 2014. Panels (a-d) present a 2 hours interval (17:00 UT to 19:00 UT) of REPT's B electron fluxes (blue circles) at 90° pitch angle for several energy channels ranging from ~1.80 MeV to ~3.4 MeV. A Gaussian-like fit (see text for details) was also superposed (black curve) onto these plots. The time T1 corresponds to the maximum fitted flux value, whereas T2 when the flux drops to 80% (roughly $1/e^2$) of this maximum value. The corresponding electron pitch angle distributions (PADs) at these two time instants are shown as red and green curves, respectively, in panels (e-h). At T1 (T2) the electron PADs have a 90°-peaked (butterfly) shape, as evidenced by the r parameter which provides the ratio between the flux at the 90° pitch angle bin to the average flux at both 47.6° and 132.4° pitch angle bins. It is defined that whenever r>1.1 (r<0.9) the analyzed electron PAD has a 90°-peaked-like (butterfly-like) shape (see text for details).

SOURCE: Medeiros et al. (2019).

Figure 5.7 - The electron flux dropout time instant.
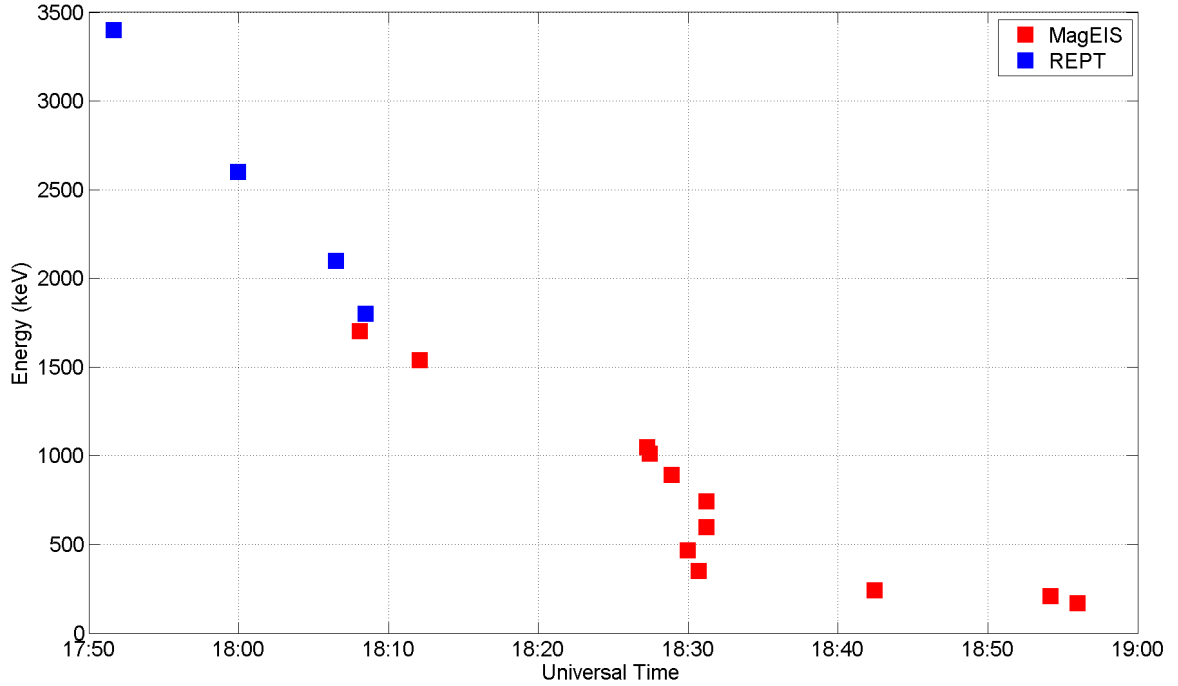
Time instant where the pitch angle-resolved electron flux drops significantly (about 80% of the maximum value) for energy channels ranging from ∼200 keV to ∼2250 keV by MagEIS(red squares) and from ∼1.8 keV to ∼3.4 MeV by REPT (blue squares).

SOURCE: Medeiros et al. (2019).

5.1.3 Investigating electron drift path using magnetic field model

For this event radiation belt particles with different energy levels could be lost to the magnetosheath since the magnetopause reached around $L \sim 7$, as far as our MHD simulation is concerned (for more details, see the outputs of the simulation under the run number Vitor_Souza_062816_1 at the Community Coordinated Modeling Center, CCMC website at: https://ccmc.gsfc.nasa.gov/). For lower-energy (up to 160 keV) electrons, even if they are lost to the magnetosheath during storm conditions, they could be resupplied by injections in the nightside region, which could explain the electron flux increase at lower energy levels. A deeper analysis about such a flux increase during this event is out of the scope of this study. At higher energies, however, the flux dropout at 90°developed and persisted for the remainder of the period shown (Figures 5.8 3(e)–(r) and 4). This indicates that equatorially mirroring

particles may have been lost from the distribution, and there was no considerable enhancement to repopulate the radiation belt during the interval of interest. The drift path for equatorially mirroring particles, considering the conservation of the first and second adiabatic invariants, can be determined using the following equation 5.3 (Min et al. 2013; Kang et al. 2016):

$$H = \gamma m_e c^2 + e(V_{con} + V_{cor}) = \sqrt{m_e c^2 (m_e c^2 + 2\mu B_m)} + e(V_{con} + V_{cor}), \qquad (5.3)$$

where, $\gamma = (1 - v^2/c^2)^{1/2}$ is the Lorentz factor, v is the electron velocity, e is the electron charge, m_e is the electron rest mass, c is the speed of light, μ is the first adiabatic invariant (magnetic moment), B_m is mirror point magnetic field strengths at given second adiabatic invariant and, $V_{con}(V_{cor})$ is the electric convection (corotation) potentials (MIN et al., 2013b; MIN et al., 2013a; KANG et al., 2016)

Figure 5.8 - The convective potential and the electron drift paths.
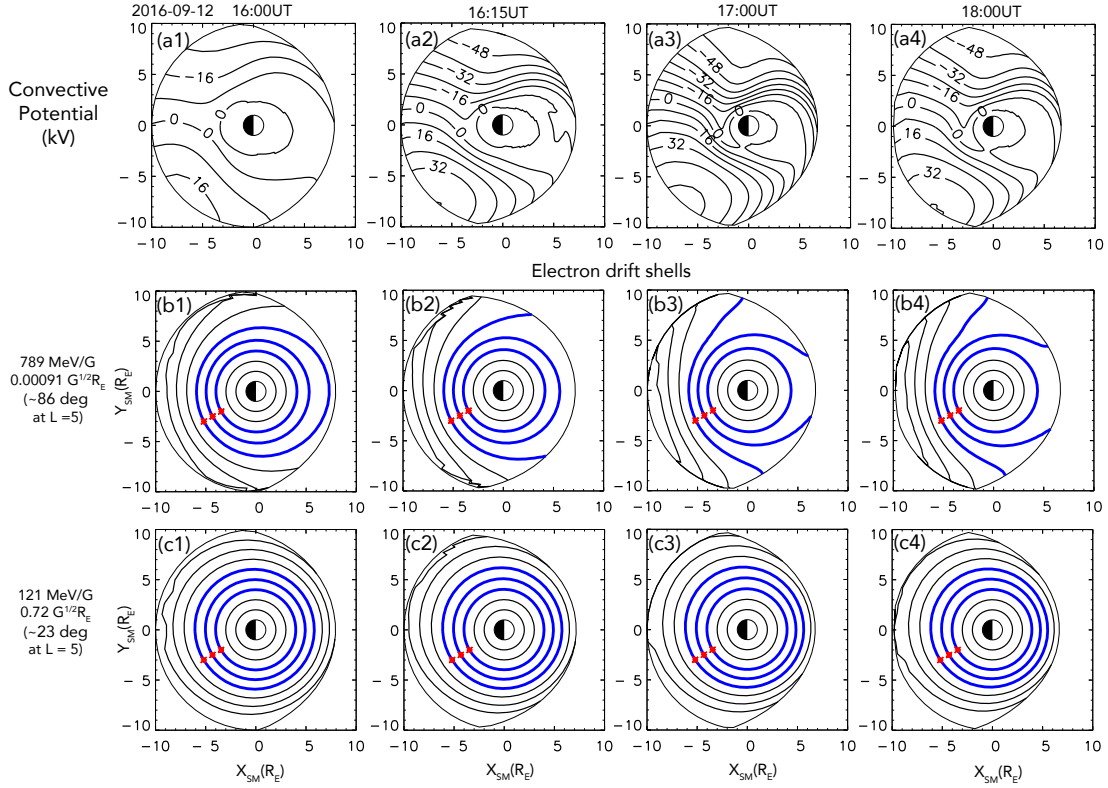
The convective potential and the electron drift paths calculated using the W2k model during September 12, 2014, in an equatorial plane, for L-shell 2 to 7. The three reds stars represent the L-shell positions 4, 5 and 6 at MLT = 2. The upper panels show isocontours of convective potential [kV] at (a1) 16:00 UT, (a2) 16:15 UT, (a3) 17:00 UT and, (a4) 18:00 UT. Drift paths at $\alpha_{eq} \sim 86°$ at (b1) 16:00 UT, (b2) 16:15 UT, (b3) 17:00 UT, and (b4) 18:00 UT for M = 789 MeV/G and k= 0.00091 $G^{1/2}R_E$ at L=5. The $\alpha_{eq} \sim 23°$ at (c1) 16:00 UT, (c2) 16:15 UT, (c3) 17:00 UT, and (c4) 18:00 UT for M = 121 MeV/G and k= 0.72 $G^{1/2}R_E$ at L=5 (see text for details).

SOURCE: Medeiros et al. (2019).

For relativistic ($\gtrsim$ 1 MeV) electrons, Equation 5.3 becomes $H \sim \gamma m_e c^2$, which means that the field-line curvature and grad B drifts dominate over the $E \times B$ drift (KANG et al., 2016). However, for electrons with lower energies ($\leq$ 100 keV), the $E \times B$ drift is dominant as it can be shown in the Appendix section of Medeiros et al. (2019). To investigate electron drift paths at different pitch angles, we used the empirical TS04 magnetic field model (TSYGANENKO; SITNOV, 2005) and the W2k electric field model (WEIMER, 2001). Figures 5.8(a1)–(a4) show isocontours of convective potential (in

units of kV) calculated using the W2k model. The electron drift shells are calculated through Equation 5.3 at fixed first μ and second K adiabatic invariants, as shown in Figure 5.8. The values of μ and K are chosen in such a way to correspond to ~ 1 MeV energy electrons, with equatorial pitch angles $\alpha_{eq} \sim 86°$ (Figure 5.8(b1 - b4)) and $\alpha_{eq} \sim 23°$ (Figures 5.8(c1 - c4)) at $L = 5$, i.e., $\mu = 789$ MeV/G and $K = 0.00091 G^{1/2} R_E$, $\mu = 121$ MeV/G and $K = 0.72 G^{1/2} R_E$, respectively. The Sun is on the right, and the rightmost curve indicates the magnetopause in each plot. Because convective potentials are well below 1 MeV, the drift paths of electrons with ~ 1 MeV energies are nearly independent from the convective potential contours. The electron drift paths passing L=4, 5, and 6 at MLT=2 (blue lines in Figure 5.8) are totally closed at 16:00 UT, and after 15 minutes, the drift paths at $L \geq 6$ are intersected by the magnetopause, as presented in Figures 5.8(b2)–(b4). It explains the transition in the electron PAD shapes at relativistic energies from 90°-peaked to butterfly.

5.1.4 Investigating EMIC waves effect on the electron flux pitch angle distribution

In addition, Medeiros et al. (2019) suggested that EMIC waves measured in situ by the EMFISIS instrument on board the Van Allen Probes B are responsible to scatter relativistic electrons above 1.2 MeV (as detailed below) via resonant interaction. For the dropout event being analyzed by Medeiros et al. (2019) , in order to explore the EMIC waves occurrence, the power spectral density (PSD) was calculated based on the magnetic field perturbation $\delta B = B - B_{avg}$, where B_{avg} is a 100 seconds time average of the B field, as done by Wang et al. (2015). We performed a Short-Time Fourier Transform with a window length of 3750 samples (~ 1 minute), and an overlap of 1875 samples ($\sim$30 s). The EMIC-wave frequency range (0.1–2 Hz) is shown in Figure 5.9 (Figure 5.10) for RBSP-A (RBSP-B) measurements along the three orbits on 2014 September 12. The panels show (a) the power spectral density, (b) the electron PAD at the 2.1 MeV energy channel, (c) MLT, and (d) the L-shell parameter.

Figure 5.9 - RBSP-A Magnetic field magnitude's power spectral density.
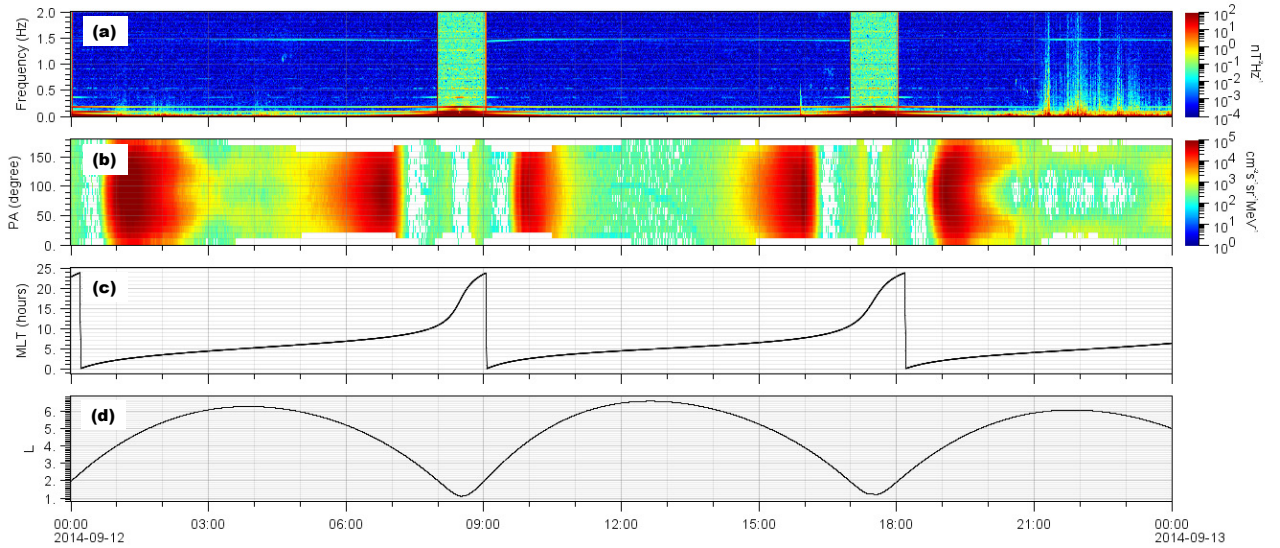
(a) Magnetic field magnitude's power spectral density (PSD), (b) pitch angle distribution at 2.10 MeV energy channel, (c) MLT and (d) L-shell parameter obtained by the Van Allen Probe A on September 12, 2014. We note that the PSD signal at around 1.5 Hz corresponds to the satellite spin tone.

SOURCE: Medeiros et al. (2019).

Figure 5.10 - RBSP-B Magnetic field magnitude's power spectral density.
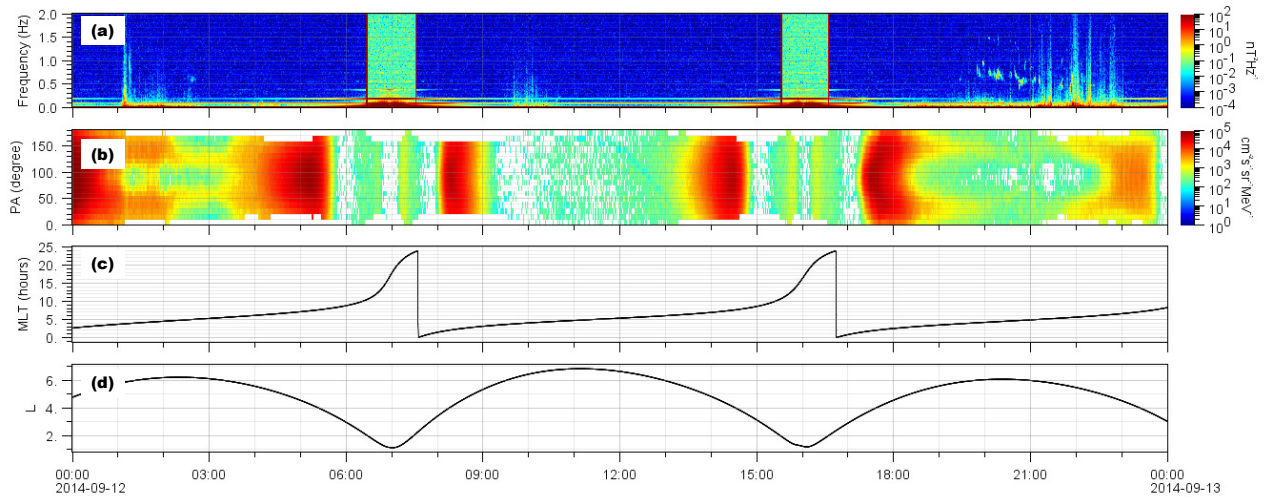
(a) Magnetic field magnitude's power spectral density, (b) pitch angle distribution at 2.10 MeV energy channel, (c) MLT and (d) L-shell parameter obtained by the Van Allen Probe B on September 12, 2014.

SOURCE: Medeiros et al. (2019).

At the time when EMIC waves are observed at RBSP-B location, EMIC waves at the RBSP-A position are not observed. It seems to be that the EMIC wave activity did not cover a large area to reach both spacecraft positions. On the other hand, the EMIC wave activity was not long enough to be observed by both spacecraft even when, one hour later, RBSP-A crossed the same MLT region (see Figures 5.9(c) and (d)). The magnetic PSD from both RBSP showed broadband, impulsive vertical streaks that will not be treated here. The dawnside sector is a slightly less favorable local time region for EMIC waves occurrence (SAIKIN et al., 2015). Still, the importance of the local in situ observations are relevant because EMIC waves are a very localized and sporadic phenomena (ZHANG et al., 2016b). The Van Allen Probes mission provides us with an unique opportunity to disentangle spatial from temporal features in the observations. All measured magnetic field components, i.e., parallel, azimuthal, and radial, showed similar signatures of EMIC

65

waves with essentially equal power in all three components (not shown). EMIC waves are generally transverse, with little or no compressional component, thus such observations are somewhat unusual. The impact of this unusual nature is not clear, so further investigation on this matter might be worthwhile pursuing, but this issue is not treated by Medeiros et al. (2019), nor it is going to be dealt with in this thesis.

Figure 5.11 - Occurrence of EMIC waves observed by Van Allen Probe B.
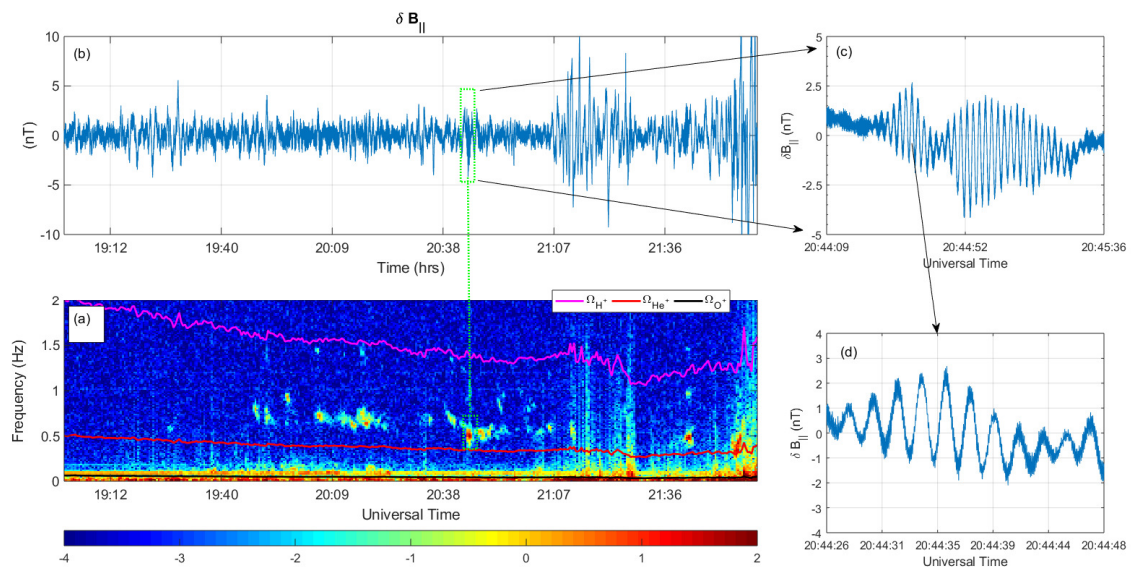
(a) Wave power spectrogram in the range of 0.1 to **2** Hz for the 18:00 to 23:00 UT period on September 12, 2014. The magenta, red and black lines correspond to ion gyrofrequencies for Hydrogen, Helium and Oxygen, respectively. (b) Time series of the variation (relative to a 100-sec local average of the background) parallel magnetic field component in the MFA coordinate system. The most intense oscillations in the magnetic field correspond to EMIC waves. (c) Detailing of an intensified magnetic field variation during the analyzed event shows EMIC wave packets. (d) An Interval of 22 seconds of data showing a wave packet in detail. The central frequency is about 0.6 Hz and the maximum amplitude of the disturbance is approximately 2 nT.

SOURCE: Medeiros et al. (2019).

The parallel ($B_{\parallel}$) component was chosen as an example of the EMIC wave occurrence on 2014 September 12 after 19:00 UT. The spectrogram is plotted in Figure 5.11(a), and the H+, He+, and O+ gyrofrequencies are overplotted. Hydrogen band (H+)

EMIC waves have been observed. Figures 5.11(c)–(e) present successive zoom-ins of a given EMIC wave packet. The Y-axis shows the magnetic field perturbation ($\sigma B_\parallel$), and from it has been estimated the peak wave amplitude which is ~ 2 nT, and the frequency varies from ~ 0.5 up to 1 Hz. The minimum resonance energy E_{min} was calculated following Equation 5.4 (KANG et al., 2016; SUMMERS; THORNE, 2003):

$$E_{min} = [[1 - (\frac{v_\parallel^2}{c^2})]^{-1/2} - 1]m_e c^2 = [(1 - \beta_\parallel^2)^{-1/2} - 1]m_e c^2, \tag{5.4}$$

where,

$$\beta_\parallel = \frac{v_\parallel}{c} = \frac{xy + |s|n(n^2 - x^2 + y^2)^{1/2}}{(n^2 + y^2)},$$

$$x = \frac{\omega}{|\Omega_e|}, y = \frac{ck}{|\Omega_e|}, \tag{5.5}$$

$v_\parallel$ is the electron velocity paralell to the field line, m_e is the electron rest mass, ω and k are the angular frequency and wave number of EMIC waves, respectively, Ω_e is the electron gyrofrequency, n is the resonance harmonic number (assumed to be 1), and finally s is set to be -1 for the left-hand mode. The minimum resonant energy is strongly dependent on the plasma composition, the wave frequency and the background magnetic field B_0 (KANG et al., 2016; SUMMERS; THORNE, 2003). We assumed $H^+ = 75\%$, $He^+ = 20\%$ and $O^+ = 5\%$ (SUMMERS; THORNE, 2003).

It was used cold plasma dispersion and assumed to be $0.8\Omega_{H+}$ and the electron number density is given by the spacecraft potential. The minimum resonance energy is 1.2 MeV, which strengthens the claim that the EMIC wave packets observed in this event can resonantly interact with ≥ 1.2 electrons and scatter them into the atmosphere.

5.1.5 Peculiar butterfly PAD shape

However, the major result found by Medeiros et al. (2019) is the PAD shape reconfiguration. During this event it is possible to observe a reconfiguration of the peaks of the butterfly PAD shape, that seemed to move from close to $30°(150°)$ to approximately $\sim 45°(\sim 135°)$ resulting in a peculiar butterfly PAD shape as shown in Figure 5.12. Such a pitch angle transition of the two peak fluxes suggests that some physical mechanism favored pitch angle scattering into the loss cone and Medeiros

et al. (2019) attributed it to EMIC waves, since they are present during the peculiar PAD measurement, and they are known to effectively pitch angle scatter relativistic electrons (SUMMERS et al., 2007; SHPRITS et al., 2009; LI et al., 2014; USANOVA et al., 2014; ZHANG et al., 2016a; CLILVERD et al., 2017). A summary of some of the physical mechanisms acting on the outer belt electrons during the electron PAD shape reconfiguration event analyzed by Medeiros et al. (2019) is presented in Figure 5.13 . The initial dropout of relativistic electron fluxes resulted initially from magnetopause shadowing. The relativistic electrons with equatorial pitch angles near the loss cone remained, in part, trapped until the occurrence of EMIC waves at around 19:30 UT. After this time, likely precipitation into the atmosphere was intensified by gyroresonant interactions with EMIC waves, resulting in the peculiar PAD. Investigations regarding the appearance of such unusual PADs in RBSP data will be addressed in this thesis.

Figure 5.12 - PAD at different energy levels from the REPT and MagEIS.
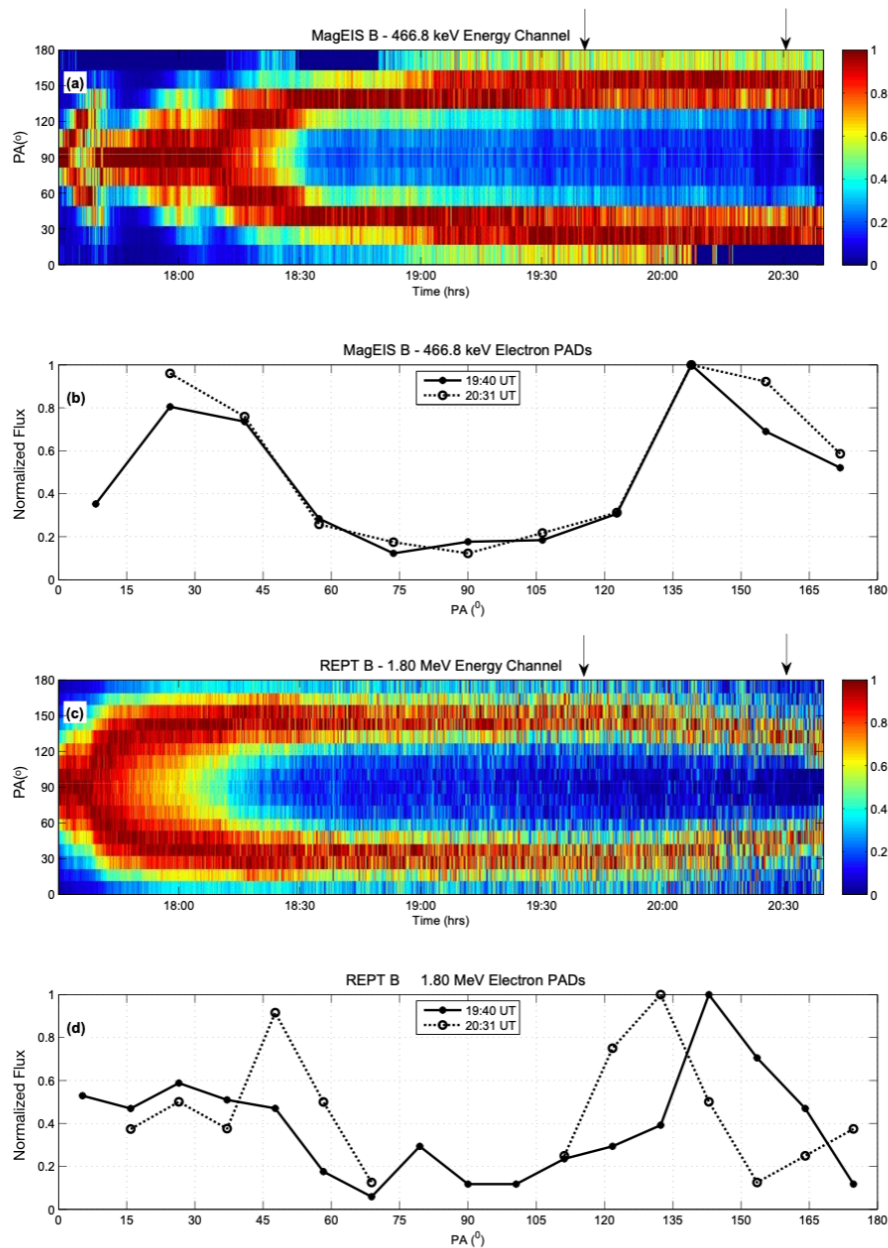
Comparison of electrons PAD at different energy levels from the REPT and MagEIS instrument onboard RBSP-B on September 12, 2014 from 17:00 to 21:00 UT. (a) Normalized PAD electron flux at the 466.8 keV energy level. (b) Sequences of PAD during the interval selected in the black box above (19:40 to 20:31 UT) representing the begining of EMIC waves. (c) Normalized PAD electron flux at the 1.80 MeV energy level. Butterfly PAD at (d) 1.80 MeV energy channel. The solid line represent the instant before EMIC waves and the dotted line during EMIC waves showed in (c) as black arrows.

SOURCE: Medeiros et al. (2019).

Figure 5.13 - Pitch angle omnidirectional electron flux spectrogram.
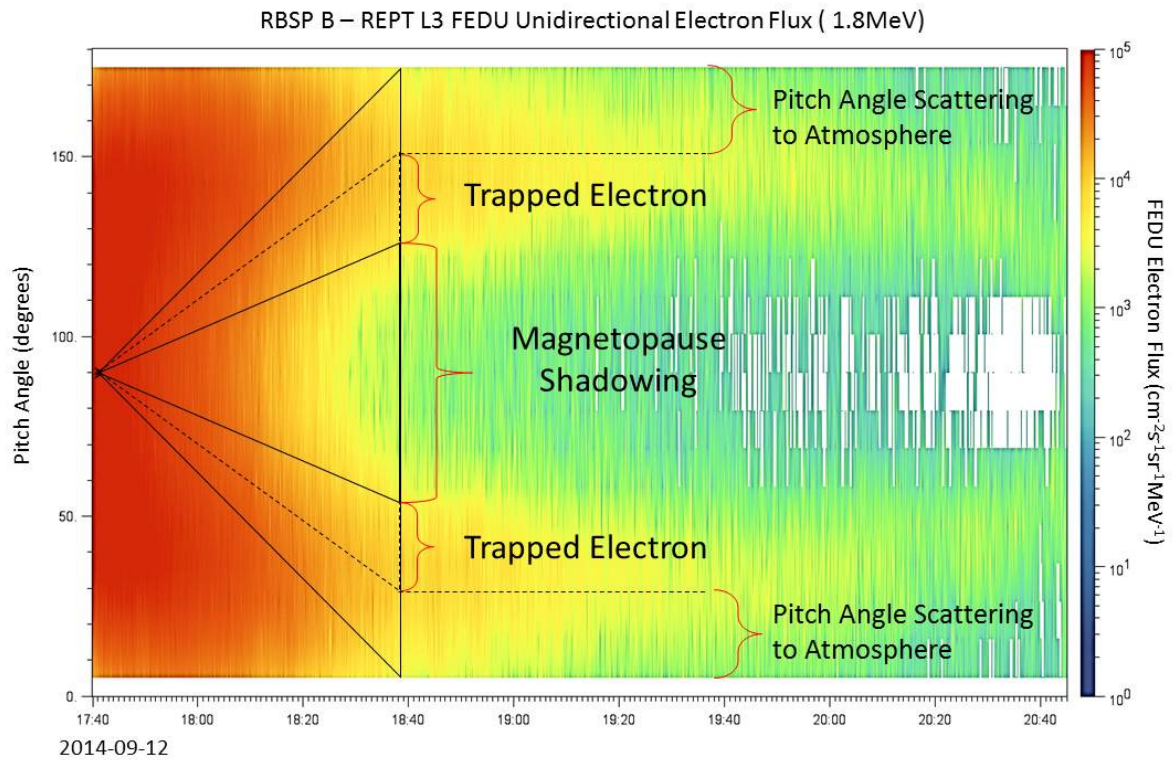
Pitch angle omnidirectional electron flux spectrogram in 1.8 MeV energy channel during September 12, 2014 between 17:40 and 21:00 UT. The electron flux dropout observerd after 18:30 UT in pitch angles close to 90° seems to be due to magnetopause shadowing. The dropout in pitch angles lower than 30° and higher than 150° after 19:00 UT corresponds to pitch angle scatter into atmosphere.

SOURCE: Medeiros et al. (2019).

5.2 Summary

On September 12, 2014, the Earth's magnetosphere was impinged by an ICME. The twin Van Allen Probes measured an electron flux dropout at several energy levels. The global MHD SWMF/BATS-R-US model coupled with the RCM module to self-consistently model the Earth's magnetospheric field for the period encompassing the ICME arrival at Earth. The MHD simulation showed that the ICME-related

compression "opened" the previously closed and outermost electron drift paths, i.e., the magnetic field strength isocontours. The empirical TS04 magnetic field model (TSYGANENKO; SITNOV, 2005) and W2k electric field model also showed the higher-energy (up to 2 MeV) electron's drift paths at L-shells commensurate to those at Van Allen Probes reached the magnetopause, thus confirming the magnetopause shadowing scenario. This event showed an electron flux dropout for electron energies above 132 keV, with the loss of higher energy electrons being observed before the lower-energy ones. The observed PADs had butterfly shapes with two peaks around 30°and 150°after the magnetopause compression, while electrons at energy levels $\leq$ 132 keV exhibit a 90°-peaked or pancake PAD shape throughout the analyzed period. The two peaks in the butterfly PAD, which had previously been around 30°and 150°pitch angles, moved to $\sim 45°$ and $\sim 135°$, resulting in a peculiar butterfly-like PAD shape. The next step is investigating how unusual are the electron butterfly PAD shapes reported by Medeiros et al. (2019). Their occurrence rate is estimated for a time interval corresponding to one full precession of Van Allen Probes' orbit as will be shown later on in chapter 7. But firstly, a survey of EMIC wave event candidates is performed in Van Allen Probes data, since these peculiar electron PADs have been observed in association with them. The next chapter details the methodology employed to the survey.

6 EMIC WAVES SURVEY: A MACHINE LEARNING-BASED APPROACH

The machine learning-based algorithm used here to perform a semi-automated survey of EMIC waves in spectrogram images is the focus of a paper submitted to AGU's Space Weather journal, and this chapter summarizes the main results found in this paper.

6.1 Bag of features technique

Bag of features is based on a visual categorization using Bag of keypoints (CSURKA et al., 2004; O'HARA; DRAPER, 2011). The idea is to extract information from an image and use them as a group of characteristics that better describe the image itself. In this study there is a huge dataset of images. The identification of objects in an image required a definition of patterns. It meant it was necessary to establish what information to search on the dataset. It was possible to find EMIC waves by its signatures. To do that It was necessary to codify each one of the 66,204 images characteristics. In appropriation of these characteristics(features), it was possible to find those which are common in images containing EMIC waves and distinguish them for those that are not. A MATLAB routine was developed to improve this. All images were described as a matrix containing horizontal and vertical axis revealing the resolution of the image. The pixel image intensity was defined by the value attributed to the pixel. In a grayscale image monochrome these values ranges from 0 to 256 were the lower corresponds to black pixels (weakest) and 256 in white pixels (strongest). The values between them were shades of gray. The correlation between the colors and the image itself is the weighted combination of frequencies(or wavelengths) captured.

6.2 Methodology

To detect Electromagnetic Cyclotron waves(EMIC) on the Radiation Belts it was necessary to obtain the magnetic field measured in situ during the interval of interest from September, 2012 to December, 2016. It was chosen to use the high resolution magnetic field from EMFISIS onboard on both spacecraft RBSP-A and B. The power spectral density (PSD) was calculated based on these magnetic field measurements. A MATLAB routine were developed following these steps:

Level 3 high resolution GSM coordinates CDF files downloaded from the website https://emfisis.physics.uiowa.edu/data/index for each day from both space-

crafts. Thus, each file was opened and extracted Epoch, the location and the magnetic field for all components. To select the Outer Radiation Belt region, it was calculated the Earth radii (Re) orbit and selected only measurements in location above 3 Re considering 1 Re = 6371 km. The day orbit interval had more than one orbit per day. It was necessary to separate all orbits intervals which resulted in 2 to 4 orbits intervals per day. In some cases it was merged the interval started at the end of the day with its end on the day after. Thus, the total orbit intervals were cut in small time intervals regions according to Table 6.1 and Figure 6.1.

Table 6.1 - Regions along Van Allen Probes orbit

Region	1	2	3	4	5	6	7	8
Geocentric Distance (Re)	3-4	4-5	5-5.5	5.5 to Apogee	Apogee to 5.5	5 - 5.5	4 - 5	3 - 4
Direction		OUTWARD			INWARD			

They are used to obtain the spectrogram. The Earth radii distance is considered to be 1 Re = 6371 km.

SOURCE: Author production.

Figure 6.1 - Earth Radii divisions
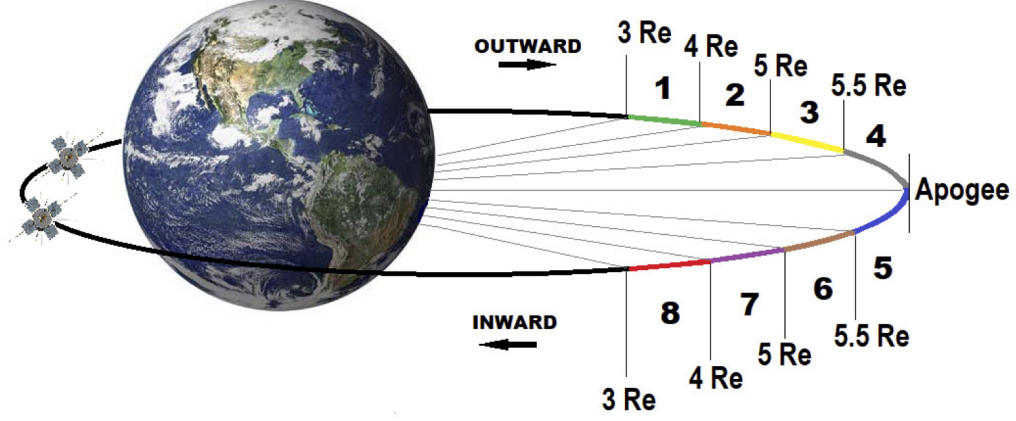
Sketch of regions along Van Allen Probes orbit where spectrogram images are obtained. These numbered regions (from 1 to 8) are selected according to the satellites' radial distance in Earth radii. The time it takes for the satellites to cross each region is around 50 minutes.

SOURCE: Medeiros et al. (2020).

Afterwards, the PSD is obtained via Fourier analysis. We performed a Short-Time Fourier Transform (STFT) of the B_i time series with a window length of 3750 samples (~ 1 minute), and overlap of 1875 samples (~ 30 seconds). The δB_i magnetic field component perturbation according to the equation:

$$\delta B_i = B_i - B_{avg,i}, \tag{6.1}$$

where $i = x, y, z$ GSM magnetic field components and $B_{avg,i}$ is a 100 sec time average of the magnetic field component B_i as done by Medeiros et al. (2019).

For each time interval we obtained three PSD, one for each GSM magnetic field component. Each spectrogram performs a x axis(horizontal) corresponding to time range (in seconds), and was defined according to Table 8.1. The y axis(vertical) was the frequency range and was set from 0 to 5 Hz. Afterwards, it was increased

the lower frequency limit from 0 to 0.2 to exclude small frequencies in this range that posed a problem during the feature extraction algorithm overestimating the EMIC waves occurrence. All images analyzed here are generated in the same way, and they all have the same color bar range, namely, from 10^{-4} to 10^2 nT^2/Hz. The spectrograms for each component were stacked up to perform a single image. An example is shown in Figure 6.2

Figure 6.2 - Spectrogram and stacked up images
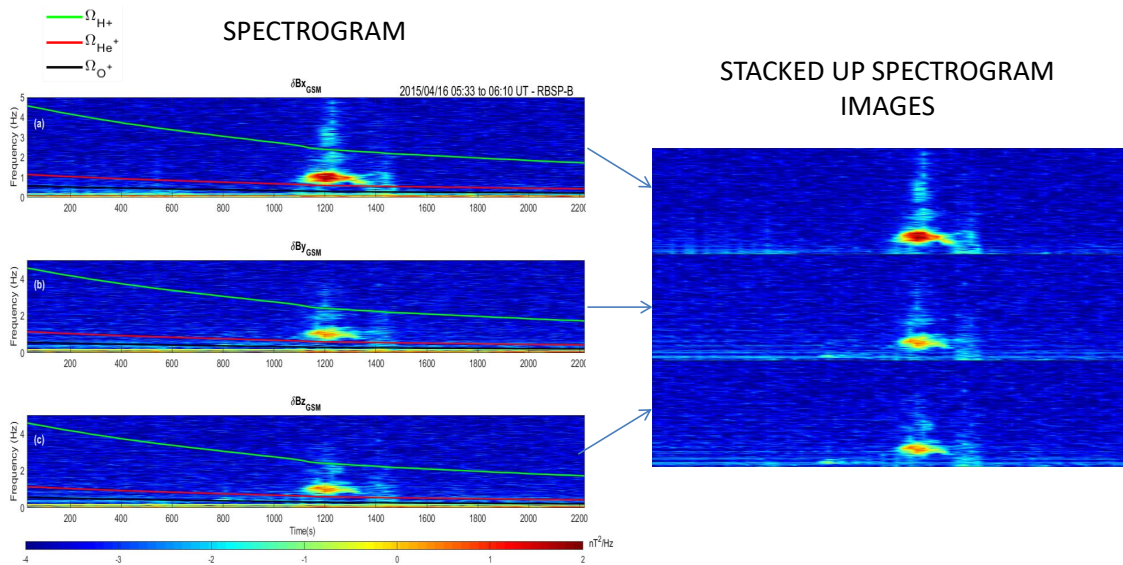
Power spectral densities (PSDs), in units of nT^2/Hz, obtained from a Fourier analysis of the time series of three magnetic field components measured by the EMFISIS instrument on April 16, 2015 from 05:33 to 06:10 UT. The y axis ranges from 0 to 5 Hz on the left-hand side panels, whereas it goes from 0.2 to 5 Hz on the right-hand side image. Panels a, b, and c contain the PSDs of δB_x, δB_y, and δB_z, respectively, along with the gyrofrequencies of ions of Hydrogen (green line), Helium (red), and Oxygen (black line). These panels show a typical EMIC wave signature found in our dataset. On the right-hand side, all three PSDs were stacked up to form a single image containing only the PSD information, so it can be used as input to the BoF technique. See text for details.

SOURCE: Medeiros et al. (2020).

It provided us 66,204 time intervals to be analysed. Vizually identifying EMIC waves in this huge dataset would take a lot of time and we decided to automatize this process. The images from the spectrogram (PSD) were in RGB and they were converted to grayscale. After this point, I will treat the stacked up spectrograms as images.

76

Images containing EMIC waves signatures presented regions where a group of pixels were brighter than the pixels around, as shown in Figure 6.2. In an unsupervised classifier, these patterns could be found in an automatic way. But, Bag-of-features were a semi supervised classification process. It meant I needed to provide the patterns as a reference to the classifier. A reference meanned images with characteristics that defined an image class pattern. After providing images according to each class, the algorithm selected, in an automatic process, the features, and grouped them according to their pattern. It was chosen, in this case, to split in two classes: EMIC and NOEMIC.

The first step was to build the dataset. It will be used as input to the feature extractor. These features were used to classify the images according to the class EMIC or NOEMIC. Before it was necessary to validate the classifier. The next sections show how the algorithm works.

6.2.1 Feature extraction

Bag of features routine from MATLAB was setup to use Speeded-Up Robust Features (SURF) detector to extract the features. The features were selected according to points of interest in an image. It could spend time and machine resources but SURF's application presented an advanced technique to process images in a faster way as well as accurately (BAY et al., 2008). The image dataset was exposed to SURF detector and returned a vector descriptor for each feature.

The SURF's approach to perform the interest point used a Hessian Matrix approximation (BAY et al., 2008). The interesting point was the location were the pixel suffer the strongest variation in its intensity related to its neighborhood. Another improvement is the concept of integral images to accelerate the computational process time (VIOLA; JONES, 2004). An element of an integral image I(x) at a location r=(x,y) represents the sum of all pixels in the input image I of a rectangular region formed by the point r and the origin. Each pixel on the image were filled by their integral value and a new integral image were built following the equation:

$$I_\Sigma(\mathbf{r}) = \sum_{i=0}^{i\leq x} \sum_{j=0}^{j\leq y} I(i,j).$$

(6.2)

Given a point $\mathbf{r} = (x, y)$ in an image I the Hessian matrix is defined as follows:

$$\mathcal{H}(\mathbf{r}, \sigma) = \begin{bmatrix} D_{xx}(\mathbf{r}, \sigma) & D_{xy}(\mathbf{r}, \sigma) \\ D_{xy}(\mathbf{r}, \sigma) & D_{yy}(\mathbf{r}, \sigma) \end{bmatrix}, \tag{6.3}$$

where $D_{xx}(\mathbf{r}, \sigma)$ is the convolution of the approximate second order Gaussian derivative with the image I at point r, and likewise for $D_{xy}(\mathbf{r}, \sigma)$ and $D_{yy}(\mathbf{r}, \sigma)$. The determinant of the Hessian matrix provides us with a quantitative information about pixel intensity variation in the immediate neighborhood of a given pixel and at a given scale . The scale parameter effectively enters as a smoothing parameter, that is, the higher its value, the higher the degree of smoothing of the original image.

All images in this dataset were 520 x 420 pixels. The first 8 scale values are used which translate into 8 box type convolution filter sizes of 9×9, 15×15, 21×21, 27×27, 39×39, 51×51, 75×75, and 99×99 pixels. Further increasing would only make the computational time for feature selection to grow without bringing newer information that has not been already found in the aforementioned eight scales.

Once the interest point was detected, a vector descriptor was created to define the feature and a new interest point started to be calculated. Each single image contained more than one stronger feature. The number of interest points in each image depends on the quantities of the pixel intensities variations. In our case, all intense variation on the spectrogram provided an interesting point. A group of strongest features defines an image. The image itself was not processed but the vector descriptor was used to classify the images. The vector descriptor was a 64 element array containing the Haar wavelet response. The features were split into smaller 4 x 4 square sub-region. For each square a 2 x 2 subdivisions carried the wavelet response (BAY et al., 2008).

Figure 6.3 illustrates the steps above. The panel on the left shows a 3D RGB color coded image as the input dataset. The horizontal and vertical axis corresponds to the time and frequency ranges from the spectrogram, respectively. Once this image was submitted to the SURF algorithm the interest point was selected. The stronger feature was denoted on the middle panel by a red circle. It was consistent with a small region where EMIC waves signature was present. This feature was explored on the right panel to show their intensities. The interesting point is the central point the size of the box correspond to the scale. The boxes were divided regularly in 4×4 square sub regions as mentioned before. A Haar wavelet filter were applied and their responses were summed in $v = (\sum dx, \sum |dx|, \sum dy, \sum |dy|)$. Concatenating all the 4×4 vectors a unit descriptor was defined as described by Bay et al. (2008).

Figure 6.3 - Example of Feature Selection
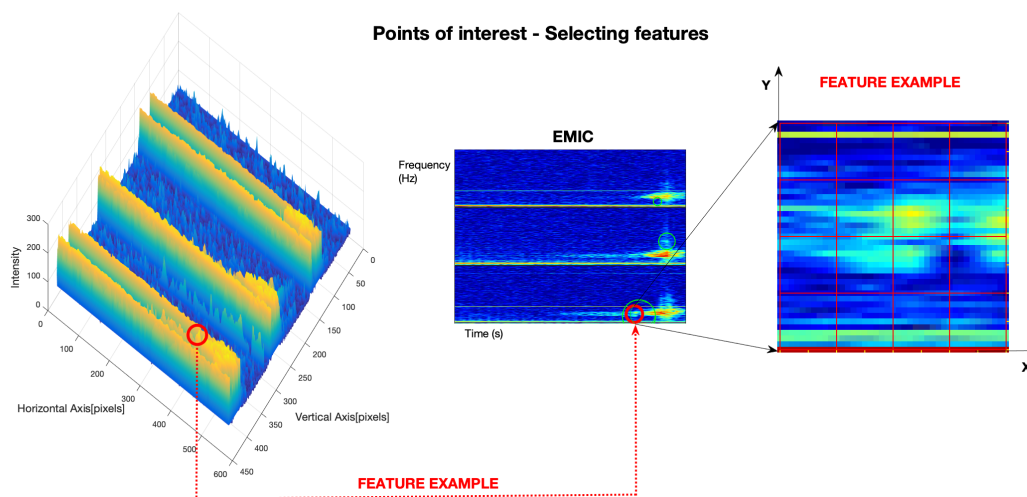
An example of the feature selection. A location from the image contained the interest point, interpreted by the SURF detector as the stronger feature, were selected and the region were mapped in 4×4 small regions. Each small region provided one of the 2 elements $(\sum dx, \sum |dx|, \sum dy, \sum |dy|)$ to the vector descriptor. This vector was grouped with other point of interest's vectors from the same image to build the set of vectors that describes the image.

SOURCE: Medeiros et al. (2020).

6.3   Classification process

The classification process was needed to separate our dataset in cases containing EMIC waves from those where there weren't EMIC, which meant NOEMIC cases. It was defined as two classes: EMIC and NOEMIC. Bag-of-features required training images which were used as references to the classifier. Also it was necessary a Validation dataset, i.e. images visually classified to be submitted to the classifier and evaluate it.

6.3.1   Training and validation process

These training and validation images were selected from the main dataset and they were visually classified as EMIC and NOEMIC class. Starting from September 2012, it was selected an interval corresponding to more than an entire precession orbit re-

lated to the position at the Apogee which means until August 2014. It corresponded to 30,190 images. All images were visually classified and disposed of in 5,980 EMIC cases and 24,210 NOEMIC cases. From these subset it was randomly selected 2,000 images (1,000 each class) to be used as training dataset.

The validation dataset contained 28,190 images (2,490 EMIC and 25,700 NOEMIC). Figure 6.4 shows 4 examples of images and how they were classified. The upper panel (a) and (b) show EMIC cases. Panel (a) was not so clear EMIC signatures but it was impossible to exclude that EMIC waves were not present only visually classifying. Panel (b) shows clear evidence of EMIC waves in all magnetic field components. The lower panel (c) and (d) were visually classified as NOEMIC. Panel (c) shows no EMIC signatures, only a persistent signal well known as spin tone, persistente in EMFISIS RBSP-A data at 1.5 Hz. Panel (d) presented pattern artifacts consistent with noisy where it was clearly impossible to distinguish EMIC waves from them. It led us to classify it as NOEMIC cases.

Figure 6.4 - Example of Images and their classification
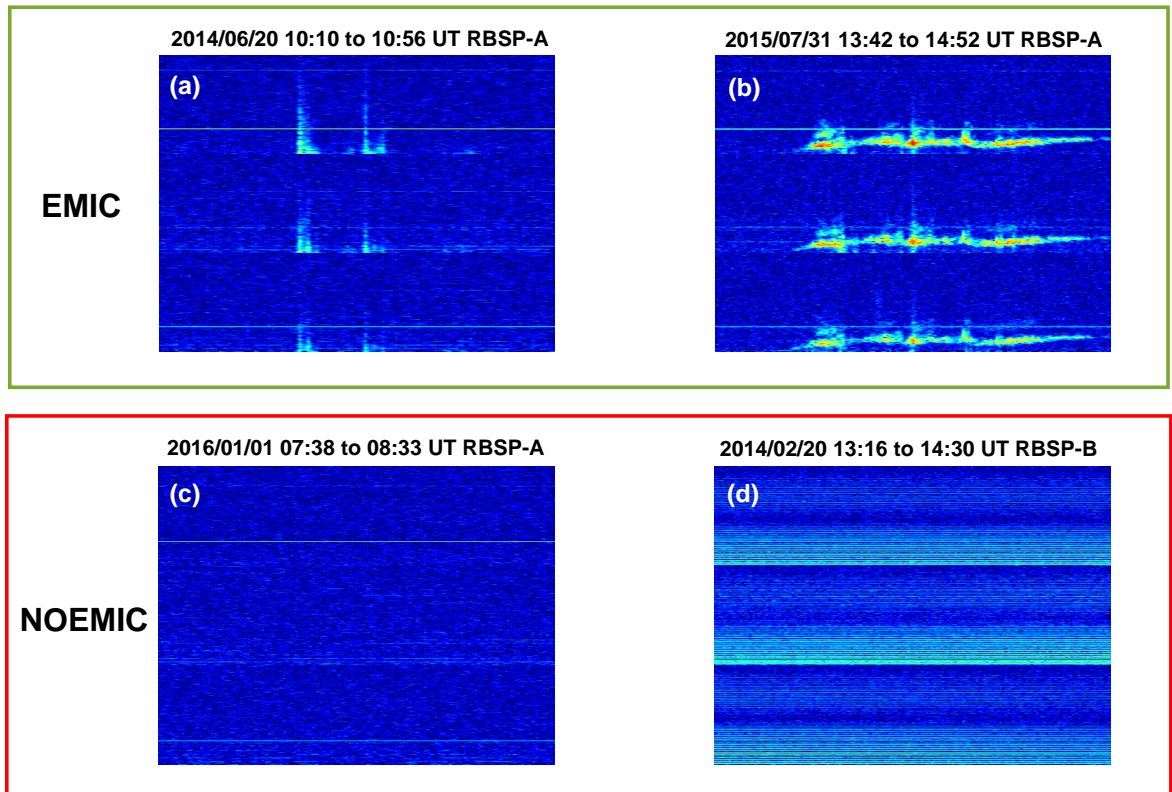
The date, time interval and which spacecraft the spectrograms have been obtained are shown on top of each panel. Images like those shown on panels (a) and (b) form a single class, named as EMIC, with likely EMIC wave events. They exemplify cases where (a) PSD enhancements might be related with EMIC wave signatures, but further analysis is required, and (b) where unambiguous evidence of EMIC waves is found. Likewise, images like those shown on panels (c) and (d) form a single class, named as NOEMIC, where (c) no distinguishable EMIC wave signatures are present, and (d) there is a presence of instrumental artifacts which do not allow a clear eye inspection of EMIC wave signatures.

SOURCE: Medeiros et al. (2020).

The classification process used k-means clustering technique (DUDA; HART, 1973) to create the bag-of-features. Bag-of-features were a 500 features references which

will be used to compare with unclassified images and the frequency of their occurrence were correlated to the class from which the image belongs. Figure 6.5 shows an example of histogram for these different classes. The green circles on the colored images corresponding to the interest points where the feature extractor built the vector descriptor. All vector descriptors on an image were submitted to the classifier and the frequency of occurrence of the visual features(words) appeared (histograms on the right side). EMIC cases usually showed a higher number of features because their images usually containing more regions were the intensity varies when compared with the background signal. The NOEMIC images usually showed a lower number of features and only some specific visual features(words) were found.

Figure 6.5 - Frequency of features in each classes according to Bag-of-features
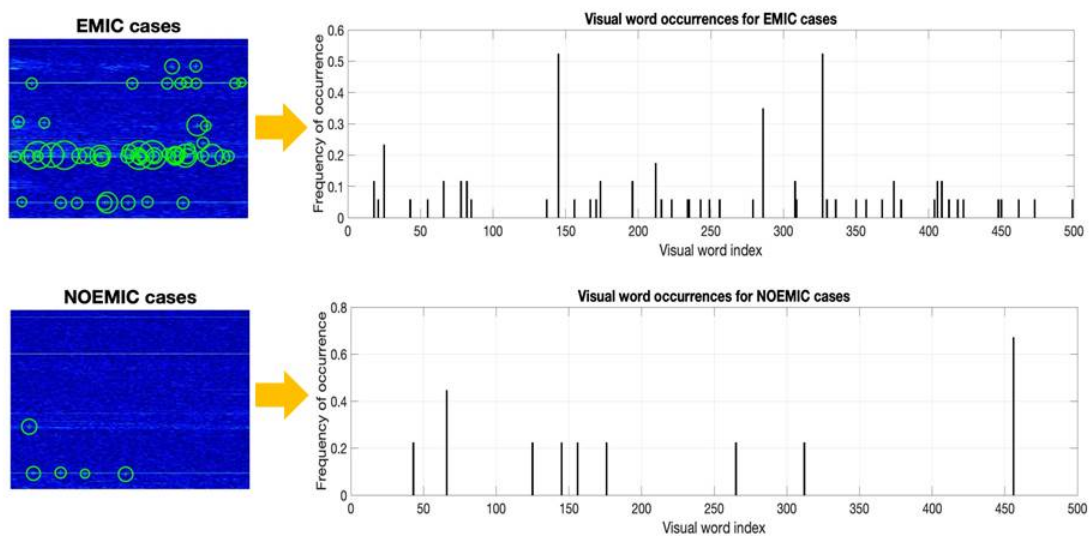
Comparison between an image from each class and the Bag-of-Feature(word). The features from the images on the left were compared and the rate in which the features(words) were more frequently corresponded to the class where the image belongs to.

SOURCE: Medeiros et al. (2020).

It meant the vector descriptor provided by the feature extractor were clusterized in such a way to define the references associated with each class. These 500 features

were known as words because they labeled the classifier. This number was tested to define the minimum size to guarantee the best accuracy. Table 6.2 shows the mean accuracy obtained when the number of words varies. Note that the higher EMIC accuracy was in 125 words and the mean accuracy were similar to 500 words, but the identification of NOEMIC were 3% higher using 500 words. That was the reason why 500 word sizes were chosen.

Table 6.2 - BoF's performance evaluation

Words or $N_{f,user}$	Average accuracy (%)	NOEMIC (%)	EMIC (%)
500	86	94	78
250	85	92	79
125	86	91	81
100	86	91	80
50	84	88	80
25	81	87	76
10	80	83	76

BoF's performance evaluation according to the number of words, i.e., the user-defined number of clusters $N_{f,user}$ wherein the features extracted from the images within the training dataset are going to be grouped via K-Means clustering (see text for details). $N_{f,user} = 500$ has been selected since it provides the best accuracy, that is, 94%, for the classification of the *NOEMIC* cases, which represents the largest part of our dataset, while not degrading too much the accuracy for the *EMIC* cases.

SOURCE: Medeiros et al. (2020).

Once the training dataset were exposed to the Bag-of-Feature script, using 500 words and the SURF vector descriptor extractor the output was a category classifier with two classes EMIC and NOEMIC. Using our 2,000 training images and 28,190 validation images, the accuracy were presented below in Confusion Matrix Table 6.3. The evaluate function from MATLAB$^{\text{TM}}$ provided us a confusion matrix comparing the known images (visually classified) with the predicted by the classifier.

The confusion matrix is calculated based on an exposure to the trained neural network of the entire validation dataset previously classified. The average confidence of 86% in classifying EMIC as shown in Table 6.3 was obtained according to the following rule: All 2,490 EMIC cases were exposed to the trained neural network and 1,931 (78%) were correctly classified into the EMIC class. It fails on 22% out of 2,490 EMIC images. All 25,700 NOEMIC cases were exposed to the trained neural network and 21,171(94%) of them were correctly classified into the NOEMIC class.

It fails on 6% out of 25,700 NOEMIC images.

Table 6.3 - Confusion Matrix

KNOWN	PREDICTED	
	EMIC %	NOEMIC %
EMIC	78	22
NOEMIC	6	94
Average Accuracy is 86%		

SOURCE: Medeiros et al. (2020).

It was investigated the misclassified images to better understand why they were wrongly classified. There were selected four images in which the classifier was different from the visual classification. The Figure 6.6(a,b) show two cases (RBSP-A and RBSP-B) visually classified as EMIC class and misclassified as NOEMIC class. The Figure 6.6(c,d) show two cases (RBSP-A and RBSP-B) visually classified as NOEMIC class and misclassified as EMIC class. The main reason seemed to be difficult for the detector to disentangle small EMIC waves signatures from the background noise.

Figure 6.6 - Wrong classified classes

Visually classified as EMIC x BoF classified as NOEMIC

Visually classified as NOEMIC x BoF classified as EMIC
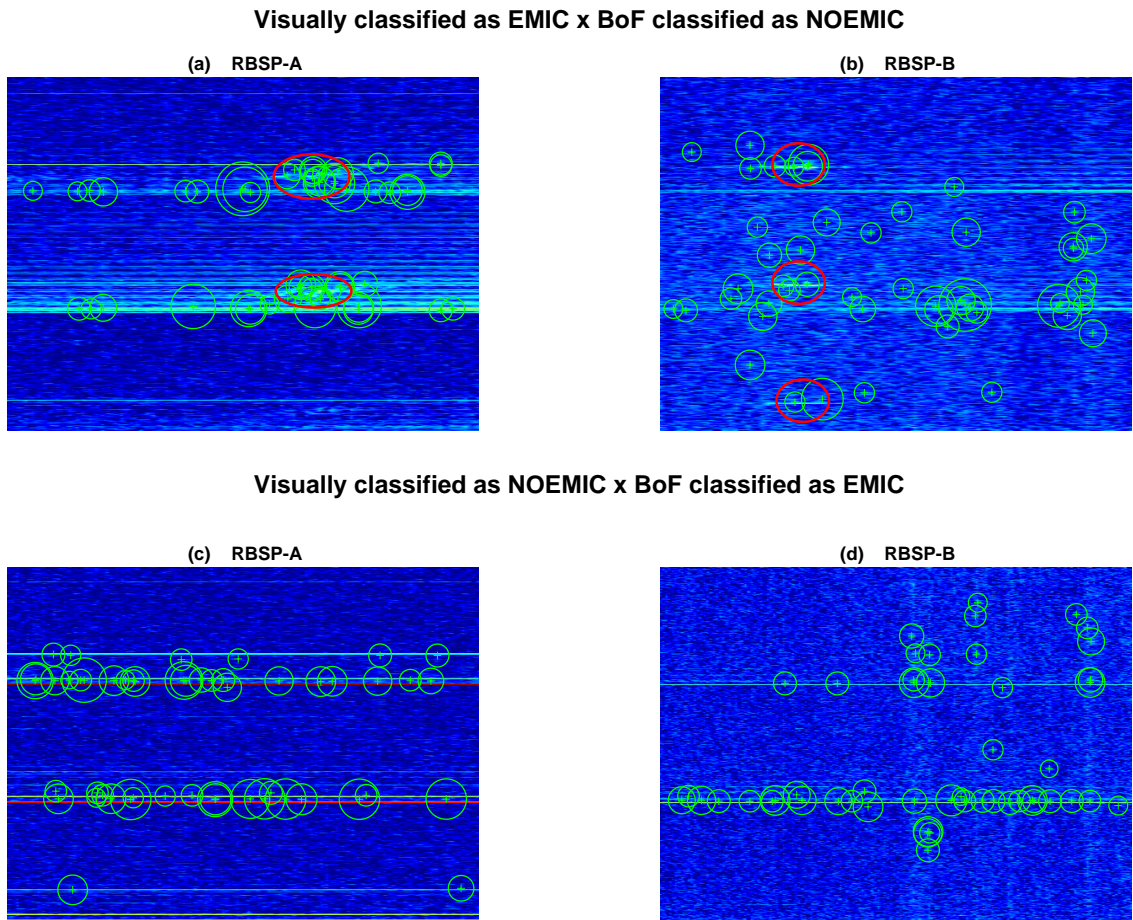
An example of wrong BoF's classification for both RBSP-A (a,c) and RBSP-B (b,d) data. Each green circle represent an extracted feature of the image as obtained by the SURF detector. Panels (a) and (b) show examples of images that have been visually classified as likely EMIC cases, therefore pertaining to the *EMIC* class, but the BoF classification defined them as belonging to the *NOEMIC* class. The opposite situation occurs in panels (c) and (d).

SOURCE: Medeiros et al. (2020).

The lower resolution from the images were probably responsible to corroborate with the misclassification of the images. A strong limitation in this analysis is the fact that in the RBSP-A spectrograms there was a spin tone in almost all images. These spin tones made the images suggest an existence of false gradient on the image.

Some of the features would be selected wrongly as strongest even when it was only a limitation. It could be the favorable EMIC waves occurrence in RBSP-A when compared with RBSP-B. Another important aspect is the

The classifier's performance analysis, in this case, can be a problem due to the inevitable imbalance of the predominant occurrence in NOEMIC cases. Even the training dataset is equal in both classes, the occurrence of EMIC on the database will always be lower than NOEMIC cases. A matrix validation submitted to the trained neural network is an example of the real database. In order to better evaluate the quality of the classifier, it is necessary to define metrics that will help to define the best network configuration (REZENDE, 2003). Considering sensitivity as the network's ability to correctly classify EMIC images (78% as mentioned before) and specificity the ability to correctly detect NOEMIC images (94%), the ideal cut-off point would be to achieve 100% for both parameters. Table 6.2 show that an attempt to improve the neural network sensitivity by increasing the proportion of correctly classified EMIC waves, decreases the specificity. This in fact increases relatively the number of NOEMIC erroneously classified as EMIC and in proportion to the relatively larger number of NOEMIC cases, this means significantly increasing the samples to be analyzed. Due to the specific character of data mining for which this network was developed, we preferred to guarantee greater specificity. It led us to a positive reliability of nearly 56% which in these validation dataset was the best result.

6.3.2   Image classifier application and results

The evaluate process showed 86% mean accuracy. The function predict from MATLAB^{TM} was used to apply the category classifier to the unclassified images (36,014). The diagram below (Figure 6.7) shows a summary of the classification process. Table 6.4 shows a dataset summary and the results in each step.

Figure 6.7 - Diagram process
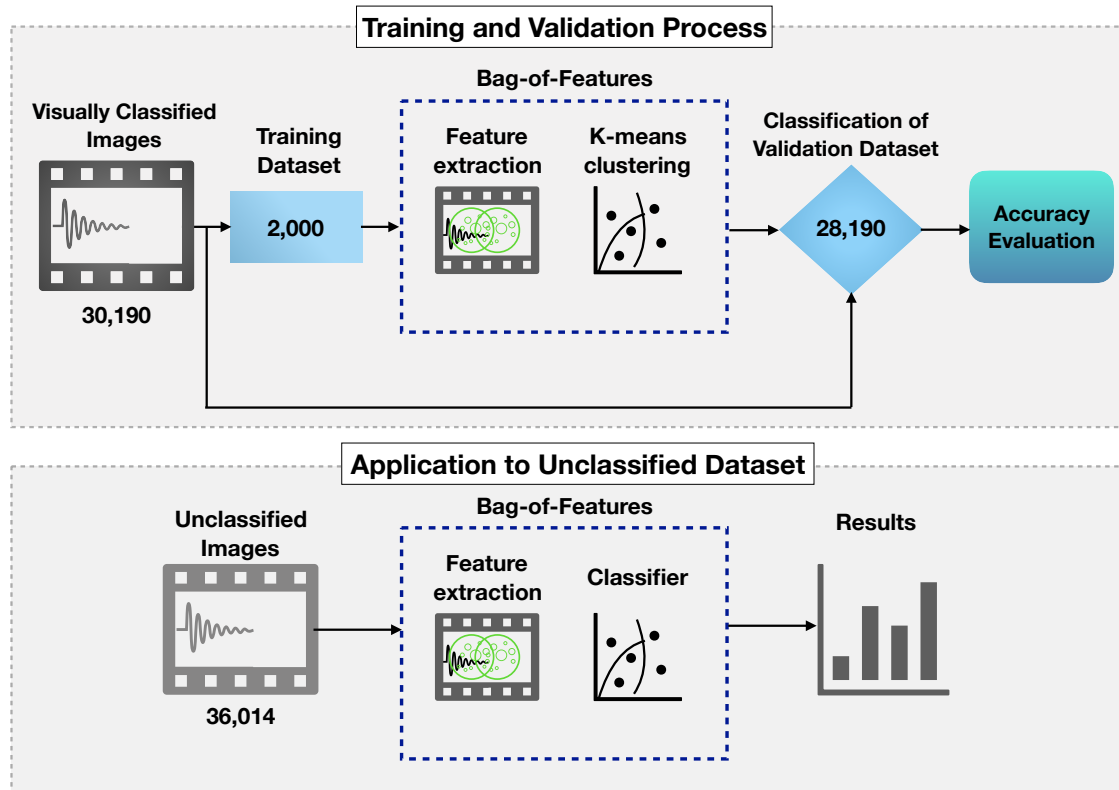
Schematic diagram to illustrate all steps involved in the classification of input images. A total of 30,190 visually classified images are used to compose both the training (2000 images) and validation (28,190 images) datasets. Once presented to the BoF, the images have their features extracted and an image classifier is built via K-Means clustering (see text for details). Using the validation dataset, the BoF's accuracy can be evaluated. Afterwards, the unclassified (36,014) images are presented to the BoF to be classified and the results are further analyzed.

SOURCE: Medeiros et al. (2020).

Table 6.4 - Dataset

DATASET	EMIC		NOEMIC		TOTAL
	A	**B**	**A**	**B**	
TRAINING	538	462	466	534	2,000
VALIDATION	1,416	1,074	12,674	13,026	28,190
BoF CLASSIFICATION	3,920	3,787	14,371	13,936	36,014
TOTAL	**5,874**	**5,323**	**27,511**	**27,496**	**66,204**

Classification of stacked up spectrogram images as either *EMIC* or *NOEMIC*. Images pertaining to both training and validation datasets totalizing 30,190 images are classified via visual inspection, whereas the remaining 36,014 images from the whole dataset are classified only via the BoF technique. A and B denote, respectively, RBSP-A and RBSP-B.

SOURCE: Medeiros et al. (2020).

The results showed (Figure 6.8) images classified by bag-of-features as EMIC in more than twenty one percent (21%). In almost eighty percent (79%) of cases, they were classified as NOEMIC. Both classes were almost balanced in occurrence from both spacecraft.

Figure 6.8 - Histogram of cases per class
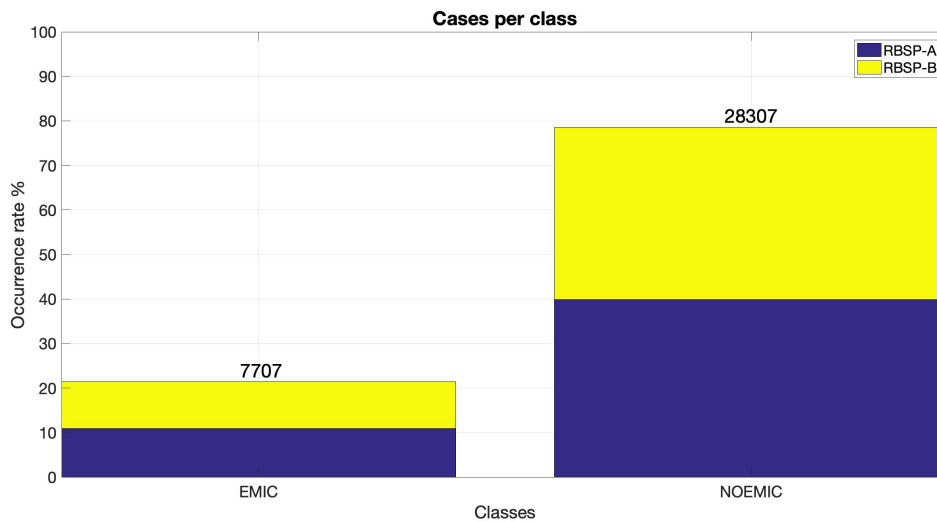
BoF's classification of unclassified dataset (36,014 images). About 21% of the input images are classified as *EMIC* and 79% as *NOEMIC*. RBSP-A and RBSP-B observed almost the same number of cases per class.

SOURCE: Medeiros et al. (2020).

The validation was classified in both ways, visually and by the BoF technique.

Comparing both techniques and counting the occurrence each month during the time interval it was observed that both techniques were well correlated. Figure 6.9 shows the distribution of the EMIC class comparing both techniques.

Figure 6.9 - Comparison of BoF's performance
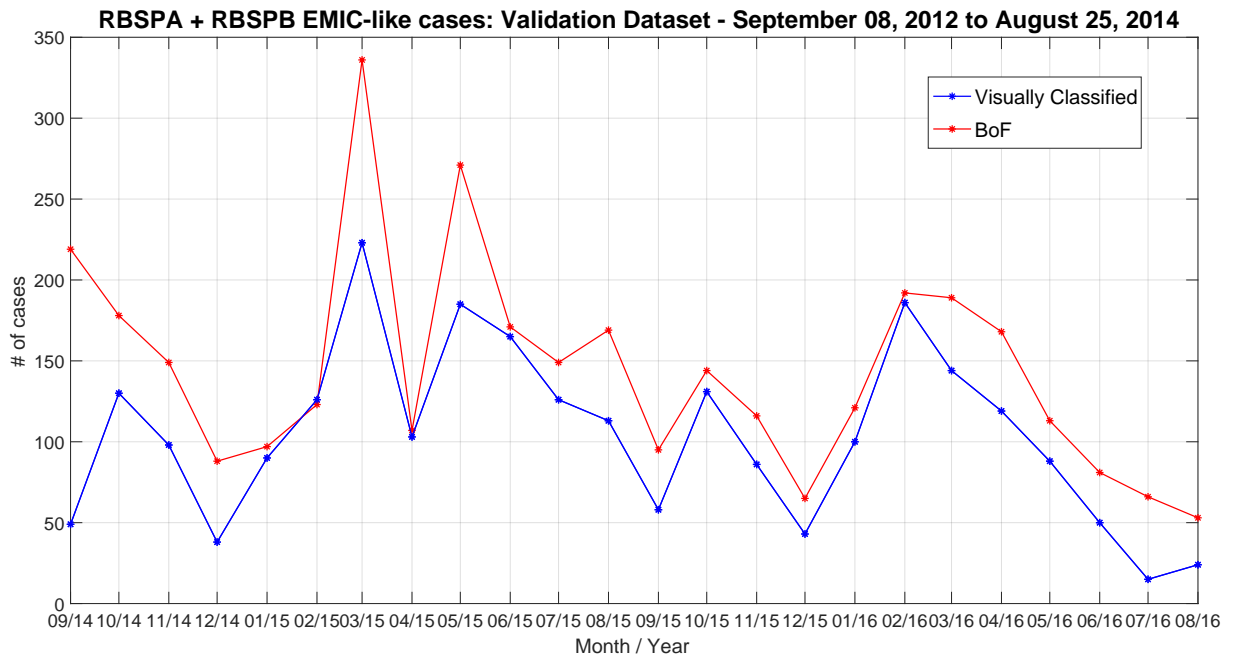
Comparison of BoF's performance against that of the visual classification method. The validation dataset is used and the period it refers to is shown on the top of both panels. The monthly number of EMIC cases as given by the visual classification (blue line) and by the BoF classification (red line) methods is shown in the vertical axis.

SOURCE: Medeiros et al. (2020).

BoF classifier was applied to the RBSP-A and RBSP-B unclassified images (36,014 images). The occurrence rates of EMIC class images by month were shown in Figure 6.11. We also plotted the occurrence of EMIC classes according to MLT and Earth Radii. The MLT were time tagged by the initial time from the interval. The interval contains around 40 minutes and were entirely inside the same region defined by the Figure 6.10. We considered only intervals between 3, 4, 5, 5.5, and 6 Earth Radii (Re). The inbound and outbound were put together. Figure 6.10 showed the occurrence rate according to the MLT for the first, second, and the beginning of the third precession. Just looking for this distribution we can observe the BoF classification

denoted the favorable region for EMIC classes near the noon and the midnight region in the first precession. The second precession contained most of the EMIC cases and the duskside region seemed to be the favoured region extended to the midnight sector. The beginning of the third precession concentrated almost all EMIC cases between midnight and dawnside region. The third precession seemed to present more EMIC cases in the region between 00 MLT and 06 MLT even though it was known the precession were not all covered. In numbers we have 1,538 EMIC-like cases whereas for the first orbit it was 529 and for the second it was 1,107.

Figure 6.10 - Occurrence rates by MLT.
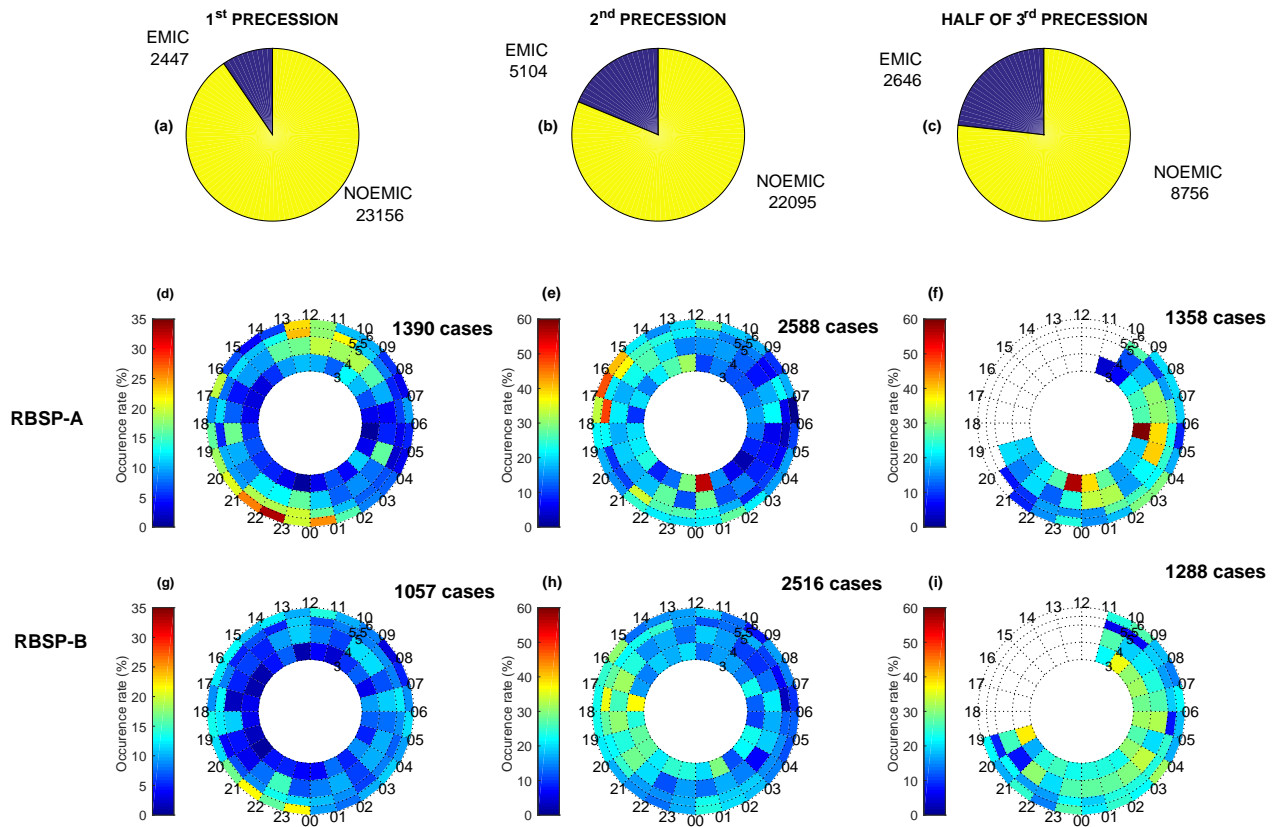
Distribution of images per classes according to the BoF classification process for (a) the first, (b) the second, and (c) the beginning of the third precession. In all intervals the NOEMIC class contained most of the cases, see Table 6.5. Panels (d,e,f) and (g,h,i) contain the distribution of EMIC class cases for MLT for RBSP-A and RBSP-B, respectively.

SOURCE: Medeiros et al. (2020).

Figure 6.11 - BoF classification for RBSP-A and RBSP-B.
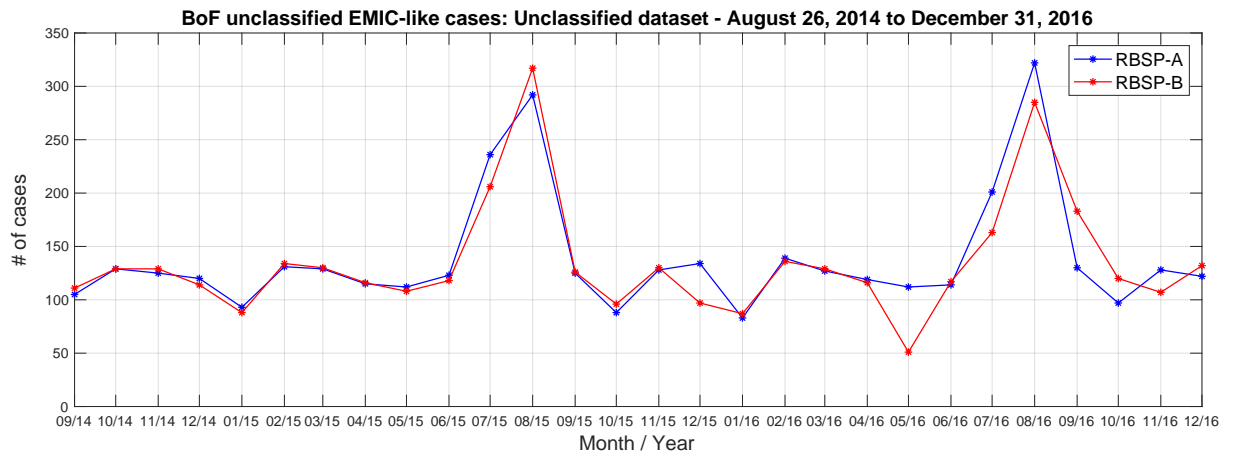
Monthly number of likely EMIC wave events as determined only by the BoF technique for the unclassified dataset which contains 36,014 stacked up spectrogram images. Data from RBSP-A (blue line) and RBSP-B (red line) is shown.

SOURCE: Medeiros et al. (2020).

This process works well to identify NOEMIC cases. It can be used to exclude NOEMIC cases from the dataset. It made it possible to reduce from 64,204 spectrograms (intervals) to nearly 10,000 spectrograms that had something different from the constant background signal. In possession of EMIC events it was necessary to correlate it with unusual butterfly-like PAD shape. It will be treated in the next chapter.

Table 6.5 - Results

DATASET	EMIC		NOEMIC		TOTAL
	A	B	A	B	
FIRST PRECESSION	1,390	1,057	11,461	11,695	25,603
SECOND PRECESSION	2,588	2,516	11,068	11,027	27,199
HALF OF THIRD PRECESSION	1,358	1,288	4,516	4,240	11,402
TOTAL	**5,336**	**4,861**	**27,045**	**26,962**	**64,204**

Number of images, per Van Allen Probe (either A or B), classified as *EMIC* or *NOEMIC* via the BoF technique. The dataset used for the BoF classification is comprised of both validation and unclassified datasets, and they are divided into three precessions of the Van Allen Probes' orbits. The first precession interval goes from September 8, 2012 to June 19, 2014, whereas the second and half of the third precessions go from June 20, 2014 to March 29, 2016, and from March 30,2016 to December 31,2016, respectively.

SOURCE: Medeiros et al. (2020).

7 PITCH ANGLE DISTRIBUTION SURVEY: A MACHINE LEARNING-BASED APPROACH

This chapter is based on the Chapter 13 "Classification of Magnetospheric Particle Distributions Via Neural Networks" (SOUZA et al., 2018) from the book "Machine Learning Techniques for Space Weather". The technique was applied to the thesis proposed here.

7.1 Pitch angle distribution

REPT instrument was designed to provide accurate measurements of energetic electron fluxes in the range ~ 1.5 to ~ 20 MeV and detailed pitch angle information (BAKER et al., 2013). These measurements were done in-situ but still represent the Van Allen radiation belt composition because particles were drifting around the Earth periodically crossing the region where the spacecraft took measurements. It made it possible to infer the dynamics of the Van Allen radiation belts since the particles motion were strongly affected by many transport processes as waves and fields along their particle journey. Associated with measurements and dynamic models of the global magnetosphere it was possible to interpret changes in the Van Allen radiation belt particle fluxes. One of the ways to analyse particle fluxes that were trapped is to infer their pitch angle. Level 3 dataset from the REPT data website provided us pitch angle time series for all the Van Allen Probe mission era. One example of the pitch angle distribution (PAD) is to show a 3-D picture of particles distribution at a given instant of time and for a given energy range (SOUZA et al., 2018).

Figure 7.1 shows electron flux data at relativistic (panels a–e) energy acquired from the REPT instrument onboard the Van Allen Probe A, during the month of November 2014. Panels (a) presents electron flux, in units of particles/$(cm^2$ s sr MeV) as a function of radial distance (L-shell parameter) and time along the Van Allen Probe A orbit. The electron flux is averaged over one orbit duration ($\sim 9h$) at each time/L-shell bin, and the flux value is assigned in a color map, where the blue (red) colors correspond to lower (higher) values. Panels (B) in Figure 7.1 shows normalized electron PADs acquired at L = 5 RE as a function of time. Normalized flux values are also presented using the same color map shown in Panel (a). Panels (c-e) show examples of PADs obtained in the time instants marked by the vertical black lines in Panel (b). The same criteria to classify PAD was used here as referred in Section 5.1.2. An example of butterfly PAD shapes presented a local flux minimum at 90 degrees pitch angle and two local flux maxima at around 45 degrees and 135 degrees

(Figure 7.1(c)). Another example of PAD shape was 90 degrees-peaked shown in Figure 7.1(d). The pitch angle distribution were shown as an all bins distributions named flattop, for example, shown in Figure 7.1(e).

Figure 7.1 - RBSP-A Electron flux and PADs.
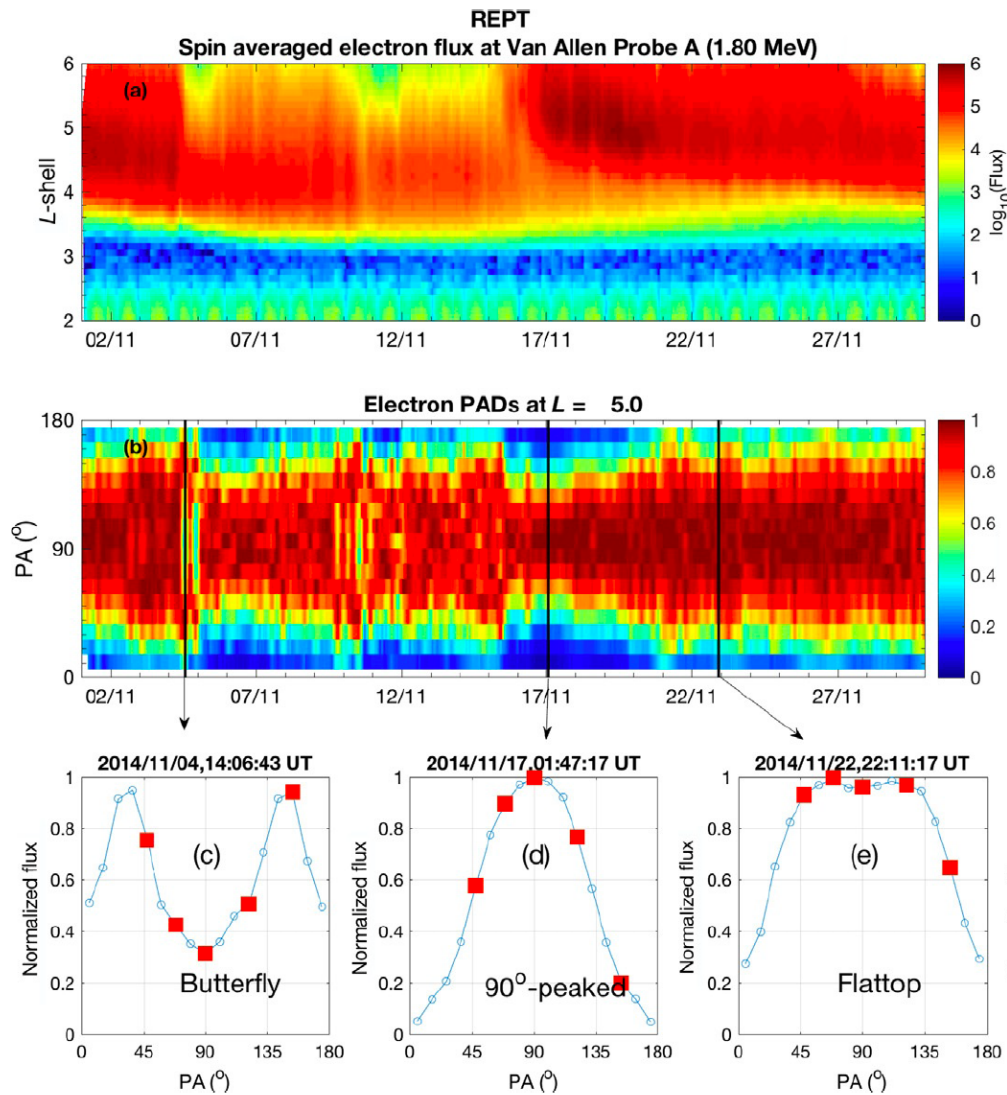
Electron flux and PADs in the Van Allen radiation belts during the month of November 2014, as measured by (a-e) the Relativistic Electron-Proton Telescope (REPT) instrument onboard the Van Allen Probe A. Panels (a-e) refer to electron flux and PAD at relativistic (1.8 MeV). Panels (b-e) show different PAD shapes that may be present along a month in the Van Allen belts region. At least three kinds of PAD shapes shown on panels (c-e) obtained at the moments marked by the vertical black lines in panel (b). The red squares on panels (c-e) indicate the pitch angles bins chosen for the learning phase of the SOM. See text for details.

SOURCE: Souza et al. (2018).

On the scope of wave-particle interactions, EMIC waves occurrence were usually associated with 90 degrees-peak PAD shapes due to pitch angle scattering (BING-LEY et al., 2019; USANOVA et al., 2014). Relativistic electron losses caused by EMIC waves were more effective in low pitch angles below around 45°(USANOVA et al., 2014). In agreement with this, Medeiros et al. (2019) presented evidence that an unusual butterfly-like PAD shape should be also associated with EMIC waves. It was found that the two local maxima flux peak in a previous butterfly PAD, originally formed by magnetopause shadowing, moved from close to 30°(150°) to approximately 45°(135°) immediately after evidence of EMIC waves occurrences. Following this issue, it seemed to be interesting to find time instants where butterfly PAD shape presented the same configuration, e.g. two local maxima flux peak at approximately 45°(135°) pitch angle bins. It was important to notice the effectiveness of EMIC waves in scatter particles into the loss cone were usually associated with the particle energy. Therefore, it was chosen to analyse PAD for relativistic electrons above 1.2 MeV.

7.2 Application of the self-organizing map technique

Self-organizing map (SOM) technique, as the name says, is an automatic process of classification, namely, unsupervised learning process. It means the algorithm is able to find patterns on the dataset and distribute these input data in output classes with similar characteristics (SOUZA et al., 2018). All neural network-related results shown in this study were obtained by MATLAB's Neural Network Toolbox1, as shown in Souza et al. (2018). To perform it there were two major steps: training and classification. The training process is the phase where the algorithm produces the output classes based on a competitive learning which is capable of activating a single neuron at any one time (SOUZA et al., 2018). In possession of the trained neural network, built by a SOM, it is possible to classify a new dataset.

As shown by Souza et al 2018 it was chosen to use SOM to classify PAD in classes where we expected to find unusual butterfly PAD shapes as at least one of the patterns found during an interval of interest. The larger the amount of different PADs in the input data presented to the SOM, the better the SOM will be able to generalize but it also provides computational cost which needs to be analysed. The procedure adopted by this thesis is described below.

7.2.1 Input dataset

To analyse PAD shape it was necessary to normalize the relativistic electron flux as done by Souza et al. (2018). The REPT instrument presented 12 different energy channels which the first one represents energy of 1.8 MeV and it was used in this study. After that, it was chosen which pitch angle bins were relevant to be used as input. In this case, five pitch angle bins were enough to find different shapes as described in previous studies aforementioned (GANNON et al., 2007; NI et al., 2015; SOUZA et al., 2016; SOUZA et al., 2018; MEDEIROS et al., 2019). Specifically, in this study, these pitch angles bins are 26.47°, 47.65°, 90.00°, 132.35°, and 153.53°. As mentioned by Souza et al. (2018), five bins is reasonable to guarantee a good representation of the PAD with low computational resources compromise.

7.2.2 PAD classification by SOM

In summary, it was selected the normalized pitch angle-resolved particle flux data for five pitch angle bins (26.47, 47.65, 90.00, 132.35, and 153.53 degrees), at 1.80 MeV electron energy channel, during the time interval from January 2014 to October 2015. After submit the input dataset to the trainning process, the results provided 32 classes as shown Figure7.2. The SOM classification method was able to identify at least three kinds of electron PADs shapes commonly found in the literature, namely, 90 degrees-peaked (classes 4, 6, 8, 20, and 22), butterfly-like distributions (29, 31, 32), and flattop-like distributions (12, 16, 23, 24). In this study, it was suggested a subclass unusual butterfly-like distribution (28) (Figure 7.2). The vertical and horizontal axes show normalized electron flux data and pitch angles, respectively. The colors at each plot mean the fraction of time that the normalized flux at a given pitch angle obtains the value on the y-axis for the set of training vectors that are mapped to each class/neuron (SOUZA et al., 2018). The unusual butterfly distribution was selected based on the discussion presented in Chapter 3.1.5.6. In this Figure 7.2 in class 28 it was observed a slightly decrease in the normalized flux on the region between 0°(180°) and 45°(135°) in comparison with the other butterfly-like distribution classes 29, 31 and 32. The proposal here is to find the time intervals which this class represents thus if they corresponds to EMIC waves occurrences as well.

Figure 7.2 - Electron PAD classification from January 2014 to October 2015.
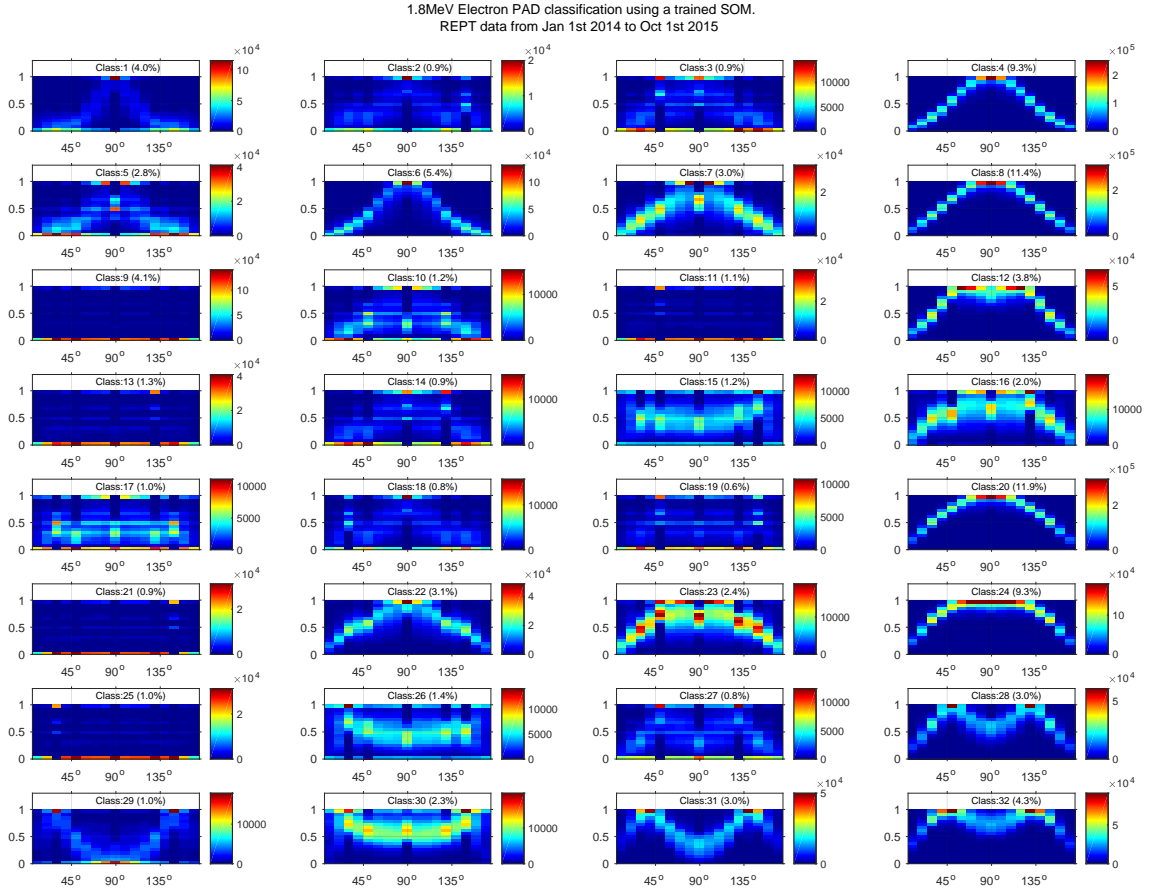
An SOM with 32 neurons/classes was trained using normalized pitch angle-resolved electron fluxes from the first (1.80 MeV) energy channel of the REPT instrument onboard the Van Allen Probe A. After the training phase, the SOM was used to classify/cluster the same input data on which the SOM was trained. The SOM classification method was able to identify at least three kinds of electron PADs shapes commonly found in the literature, namely, 90 degrees-peaked (classes 4, 6, 8, 20, and 22), butterfly-like distributions (29, 31, 32), and flattop-like distributions (12, 16, 23, 24). In this study, it was suggested a subclass unusual butterfly (28). The vertical and horizontal axes show normalized electron flux data and pitch angles, respectively. The colors at each plot mean the fraction of time that the normalized flux at a given pitch angle obtains the value on the y-axis for the set of training vectors that are mapped to each class/neuron (SOUZA et al., 2018).

SOURCE: Author production.

The spatial distribution of these classes were shown in Figure 7.3. The energy channel

selected to be classified corresponds to 1.8 MeV pitch angle resolved electron flux. During the time interval from January 2014 to October 2015 the Van Allen Probe A, covered all MLT which provided us the PAD shapes commonly find during the orbit. Similarly to Souza et al. (2018) this system of reference which is derived considering the Earth's magnetic field as a pure dipole (OP77Q), the magnetic equator plane is divided into 24 sectors/bins, each with a 15 degrees-width (24 × 15 degrees = 360 degrees). The 12 MLT (00 MLT) mark is placed along the Earth-Sun line in the dayside (nightside) region. Thus, in such a reference system, one can refers to different sectors of the magnetosphere by using the corresponding MLT (provided by the REPT instrument dataset).

Figure 7.3 shows the occurrence rate of (a) 90°-peaked, (b) butterfly, (c) unusual butterfly, and (d) flattop electron PAD as function of radial distance and MLT during one entire precession (January 2014 to October 2015). At a given MLT and radial distance bin, say 11 - 12 MLT and 4 - 4.5RE, we count the number of times NT, during the 22-month period just mentioned, the Van Allen Probe A was located within this bin. At each of these times, we use the SOM algorithm to determine the shapes of the measured 1.8 MeV energy electron PADs, and then to obtain the number of times a 90 degrees-peaked, butterfly, unusual butterfly or flattop PAD is observed. The occurrence rate of a particular electron PAD shape at a given MLT and radial distance bin is then acquired as the ratio N_{shape}/NT multiplied by 100 in order to provide a percentage value (SOUZA et al., 2018). Different from Souza et al. (2018), the occurrence rate *less than 5% of the maximum NT value for the whole analyzed interval* was not removed from our dataset.

The results shown a similar occurrence rate found by Souza et al. (2018) as expected once they are analysing the same time interval. Although, the butterfly PAD shape were split in two distinct classes in this thesis, butterfly and unusual butterfly. Our interesting is majority in unusual butterfly PAD shape. Figure 7.3(c) shows the favorable region of unusual butterfly is the nightside, slightly higher in 01-02 MLT, which differ from the butterfly PAD shape in Figure 7.3(b). The sum of both unusual butterfly and butterfly PAD shape are equivalent to the results found by Souza et al. (2018). It is well known the favorable region of butterfly PAD shapes in these regions once it was expected drift shell-splitting acting as driver to this distribution (SIBECK et al., 1987).

Figure 7.3 - PAD shapes occurrence rate about MLT and Re
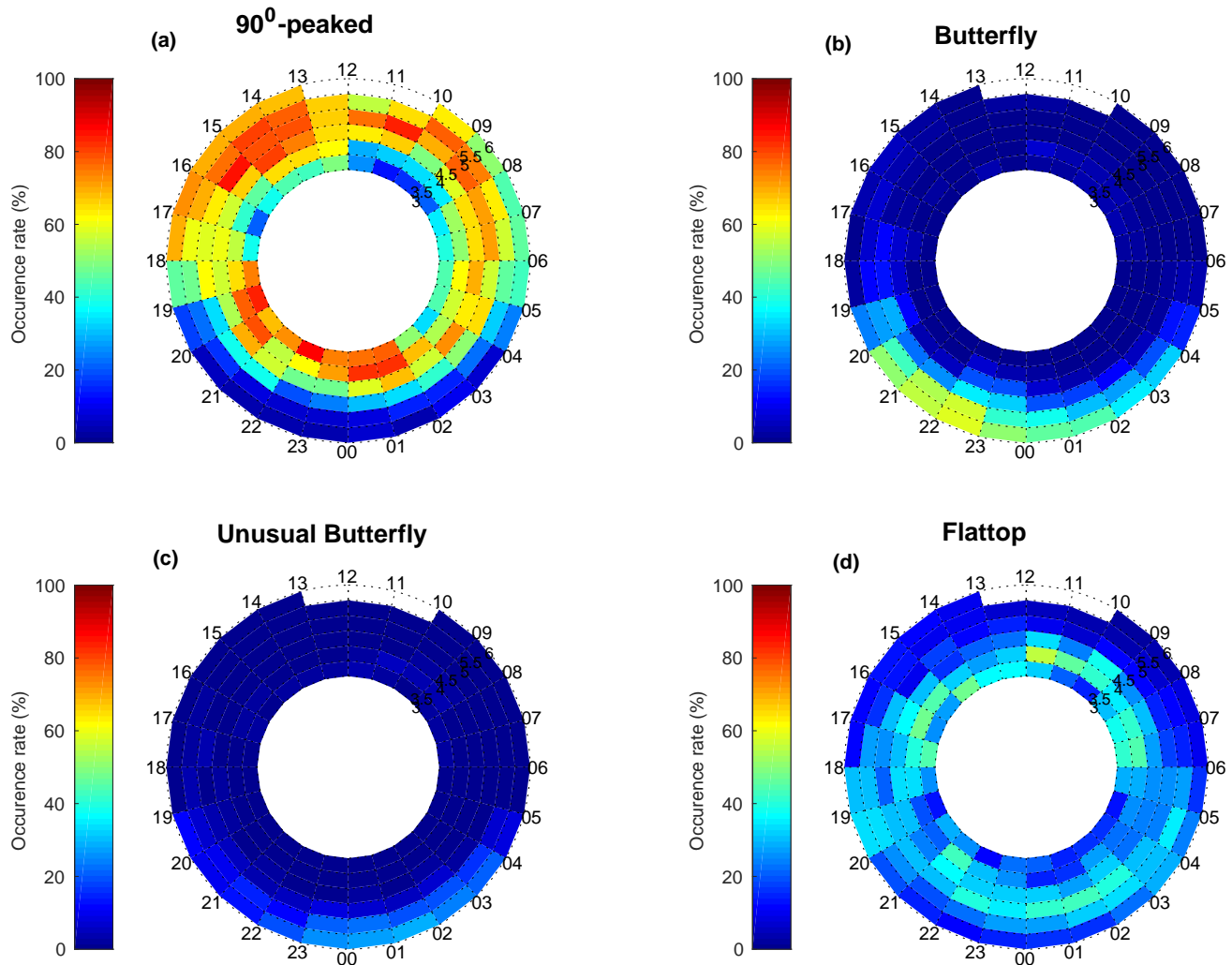
Occurrence rate of (A) 90 degrees-peaked, (B) butterfly, (C) unusual butterfly and (D) flattop PADs in the Van Allen belts for the January 1, 2014 to October 1, 2015 period. PADs were identified using the SOM method on pitch angle-resolved 1.8 MeV energy electron flux data from the REPT instrument onboard Van Allen Probe A. In each panel the PADs are seen as a function of radial distance (from 3 to 6 RE in 0.5 RE steps), and magnetic local time (MLT), where the 061218 MLT interval corresponds to the dayside region of the equatorial magnetosphere, whereas the 060018 MLT interval to the nightside region. The Sun is located at the top of each panel.

SOURCE: Author production.

Likewise, SOM methodology provided a PAD classification at instant of normalized pitch angle resolved electron flux data during all interval. Figure 7.4 shows: (a) the B_Z and B_T interplanetary magnetic field from January 2014 to October 2015, (b)the solar wind speed, (c) 1.8 MeV electron flux as function of L [1] distance and time, and (d) electron PAD classification based on SOM method. Some classes don't represent any known PAD shape and also all of them together represents less than 31% of time instants. The dataset comprises measurements from inner belt, slot, and outer belt region. The slot regions usually contains most of the undefined PAD shape once the electron flux in this energy range are extremely low in comparison with inner and outer belt region. It can be observed in Figure 7.4(c) by the dark blue colored map. Our interesting is the unusual butterfly which is barely found along this precession and almost all of them are concentrated at higher L. All the time instant classified as unusual are in class 28. The occurrence rate of unusual butterfly PAD shape is 3%(109.785 time instant). But, some isolated unusual butterfly PAD shape instant are sparse along the precession. Thus it was chosen to find time interval where a persistent shape happened. It was selected cases where the unusual butterfly PAD shape appeared for at least 10 minutes. The black dots in Figure 7.4(d) represents all the persistent ($> 10min$) unusual butterfly PAD shape. They correspond to 11.785 cases which is around 0.3% of the total (3.628.012) PAD shapes. All of them are concentrated from September 26, 2014 to August 19, 2015. During these time interval the Van Allen Probe A apogee where from 05 to 14 MLT near the nightside and also at high L-shell. It was also possible to observe the higher occurrence rate during the time interval where the electron flux at 1.8 MeV are higher.

---

[1]L-Mcllwaim's L-shell parameter computed for 90 degree particles using OP77Q external field and IGRF internal field

Figure 7.4 - PAD and SOM classification
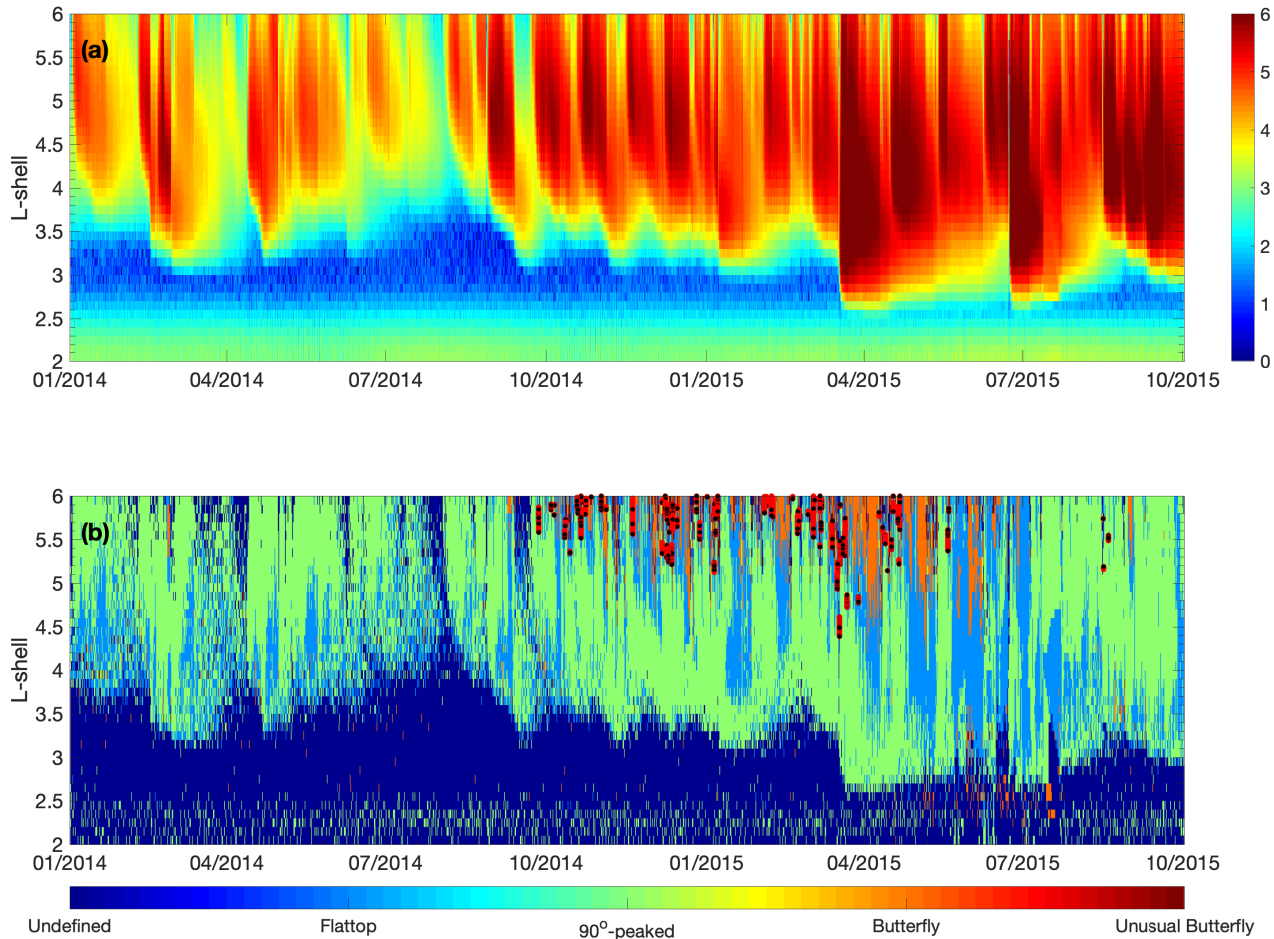
Panels show: (a) 1.8 MeV electron flux as function of L distance and time, and (b) electron PAD classification based on SOM method. The black dots represents all the persistent ($> 10min$) unusual butterfly PAD shape.

SOURCE: Author production.

Figure 7.5 shows the interplanetary parameters during from January 2014 to October 2015. The time interval from September 26, 2014 to August 19, 2015 are denoted more intense in solar activity in comparison with the previously period. The IMF, solar wind speed and proton temperature were stronger then before and they are concurrent with the stronger electron flux at 1.8 MeV showed in Figure 7.4. During this interval as mentioned before During these time interval the Van Allen Probe A apogee where from 05 to 14 MLT near the nightside region. This region is considered

a favorable region for drift shell splitting, which can led the PAD to butterfly PAD shape (SIBECK et al., 1987). The fact that most of the unusual butterfly pitch angle distribution were measured in this region is the concomitant loss of particles by EMIC waves and the reconfiguration of the outer radiation belt by drift shell splitting. It is also possible the occurrence of magnetopause shadowing as mentioned by Medeiros et al. (2019) but only with deep analysis it will be possible to distinguish between both process. It can be contemplated in future studies.

Figure 7.5 - Interplanetary parameter
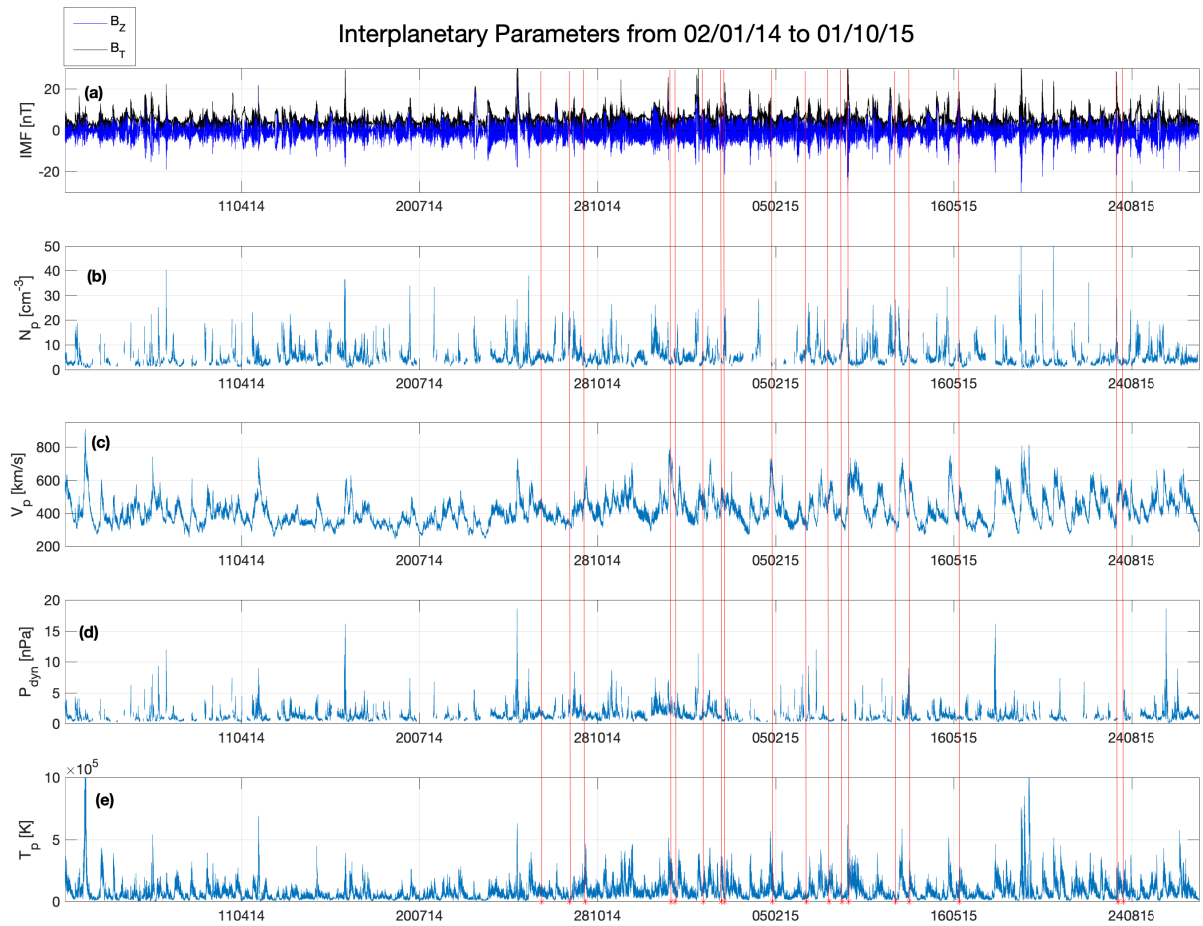
Panels show solar wind parameters from January 2014 to October 2015: (a) the B_Z and B_T interplanetary magnetic field , (b) proton density, (c) the solar wind speed, (d) Dynamic pressure, and (e) proton temperature. The red dots/lines represents 18 persistent ($> 10 min$) unusual butterfly PAD shape chosen.

SOURCE: Author production.

One interesting time interval containing the unusual butterfly PAD shape is the St Patrick' storm day. Previously studies showed butterfly PAD shapes at the same day (RUNOV et al., 2016; LI et al., 2016; BAKER et al., 2016). It was observed the butterfly as well but the persistent unusual butterfly pitch angle shape appeared a day before on March 16,2015 (Figure 7.6) and the day after on March 18,2015 (Figure 7.7).

Figure 7.6 - Day before St Patrick storm event.
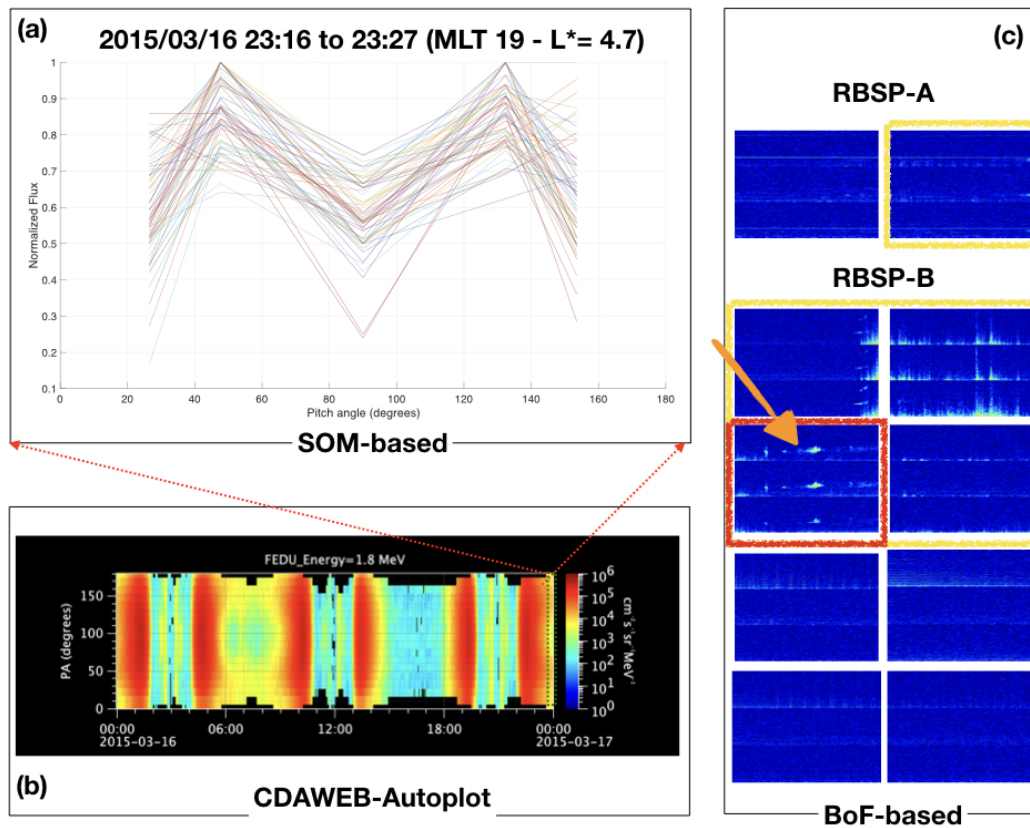
(a)SOM-based classification shown the persistent unusual butterfly PAD shape on March 16,2015 after 23:16 UT. Van Allen Probe A was in MLT 19 and L-star ~ 4.7.(b)The relativistic electron at 1.8 MeV channel shown the pitch angle distribution during one day. The interval of interesting appeared in the end of the that day.(c) Bof technique classified 10(2 by RBSP-A and 8 by RBSP-B) images as EMIC classes. Five images (yellow box) shown considerable regions in which the contrast with the background color suggested some wave activities. One of them (red box) presented clear EMIC-like wave signature(orange arrow).

SOURCE: Author production.

Figure 7.7 - Day after St Patrick storm event.
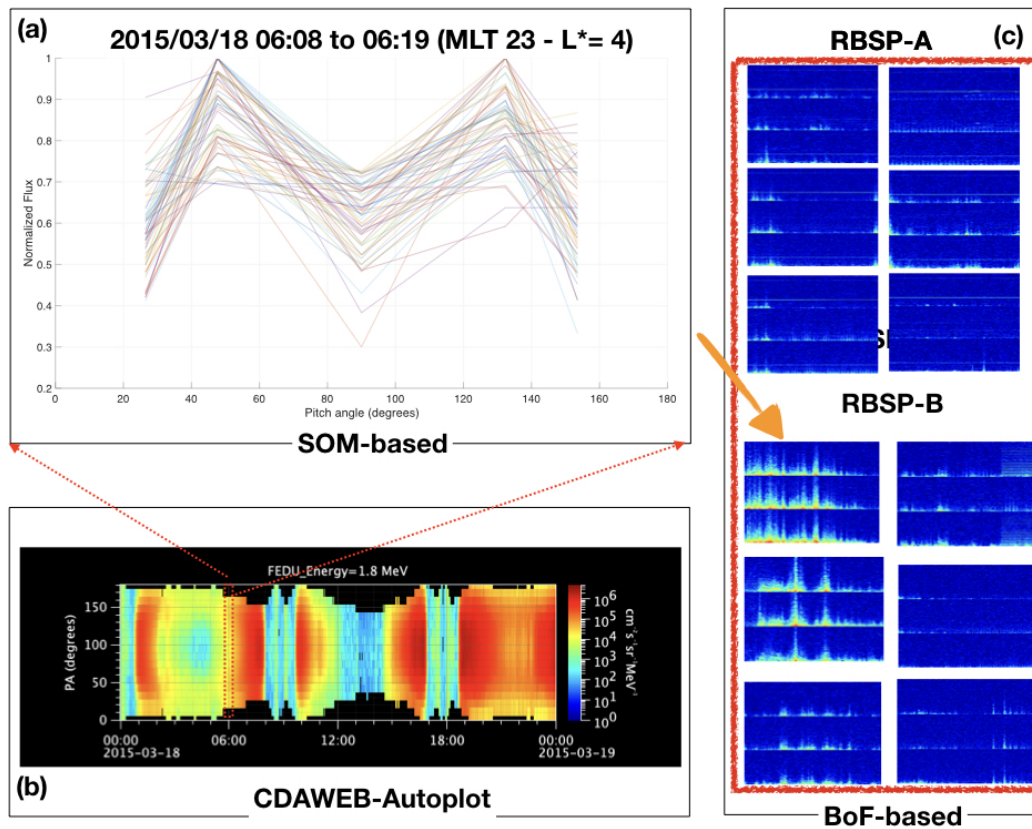
(a) SOM-based classification shown the persistent unusual butterfly PAD shape on March 18,2015 after 06:08 UT. Van Allen Probe A was in MLT 23 and L-star $\sim$ 4.(b) The relativistic electron at 1.8 MeV channel shown the pitch angle distribution during one day. (c) Bof technique classified 12 (6 by RBSP-A and 6 by RBSP-B) images as EMIC classes. All of them (red box) presented clear EMIC-like wave signature (orange arrow).

SOURCE: Author production.

The day after St Patrick storm event (March 18, 2015) was detected by SOM as containing a persistent unusual butterfly PAD shape. At the same period, BoF classified several spectrogram images as containing EMIC-like features. Figure 7.8 address this point showing the time instant where EMIC waves were probably interacting with energetic particles above 1.8 MeV and their lost which can be observed in the relativistic electron PAD flux at these energy levels. The response to the flux decrease seamed to be after minutes of EMIC waves activities quite similar to previous studies about EMIC wave particle interaction (USANOVA et al., 2013; USANOVA et al., 2014; BINGLEY et al., 2019; MEDEIROS et al., 2019; BLUM et al., 2015; CLILVERD et

al., 2015). The effectiveness in scatter particles will not be calculated in this thesis. Even thought, it is suggested to be done as future work.

Figure 7.8 - BoF and SOM approaches compared to REPT data.
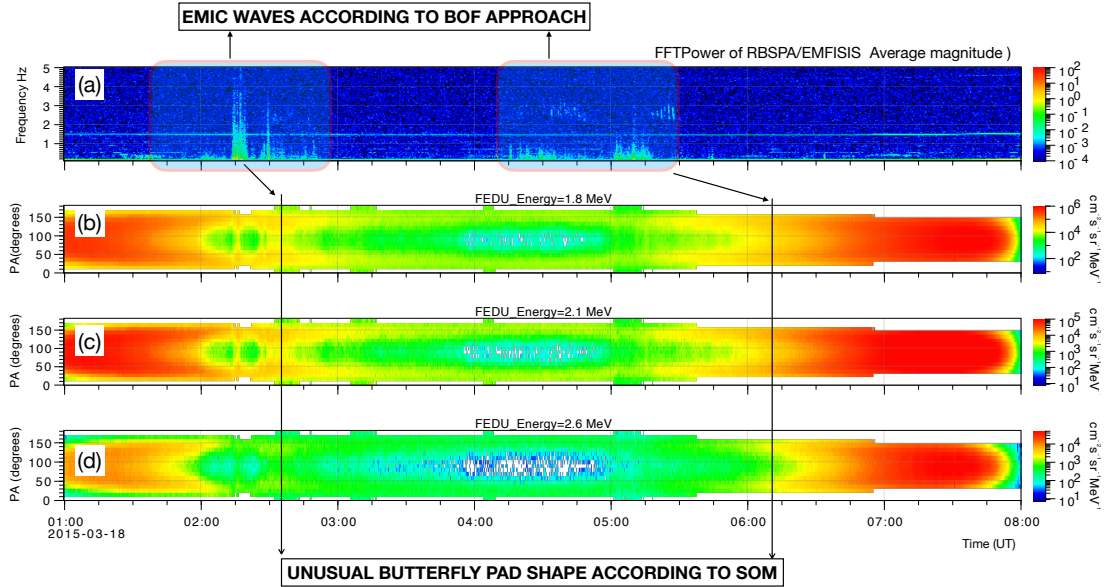
Day after St Patrick storm on March 18, 2015. Panels show: (a) Power spectrum density containing EMIC waves activities, (b) Electron fluxes PAD at (b)1.8 MeV (c) 2.1 MeV, and (d) 2.6 MeV energy channels in $cm^2s^{-1}sr^{-1}MeV^{-1}$. The black line shown the time instant in which the SOM denoted the persistent ($> 10min$) unusual butterfly PAD shape.

SOURCE: Author production.

These persistent unusual butterfly PAD shape were most pronounced in 23 events analyzed during the whole precession (see Anexo A for others 21 events cited here). It was observed the occurrence of EMIC waves in 21 out of 22 days. Our neural network based technique, i.e., Bag-of-Features, described in Chapter 6.2 showed at least one image containing EMIC-waves like signatures. As mentioned by Runov et al. (2016), Li et al. (2016) it was essential to estimate the EMIC wave contribution to resonant interact with relativistic electron acting as an additional mechanism responsible for scatter particle into loss cone.

8 CONCLUSIONS

This thesis was developed in at least four major steps: 1°) a case study about the likely contribution of EMIC waves in the reconfiguration of regular electron butterfly pitch angle distribution (PAD) at relativistic ($\gtrsim 1\,\mathrm{MeV}$) energies into an unusual or peculiar electron butterfly PAD shape (MEDEIROS et al., 2019); 2°) an EMIC waves survey performed by means of a machine learning (Bag-of-Features)-based approach and whose results have been submitted to *The Astrophysical Journal Supplements* (MEDEIROS et al., 2020); 3°) utilization of another machine learning-based methodology known as Self-Organizing Map (SOM), as previously implemented by Souza et al. (2018), in order to find unusual electron PAD shapes similar to those found by Medeiros et al. (2019); and finally 4°) the connection between all developed techniques in an attempt to verify whether there is a direct association between unusual electron PAD shapes, as reported by Medeiros et al. (2019), and EMIC waves occurrence. This chapter is an effort to show the evolution and the major findings as well as how everything is connected. Figure 8.1 summarizes the steps above.

Figure 8.1 - Flow chart summary
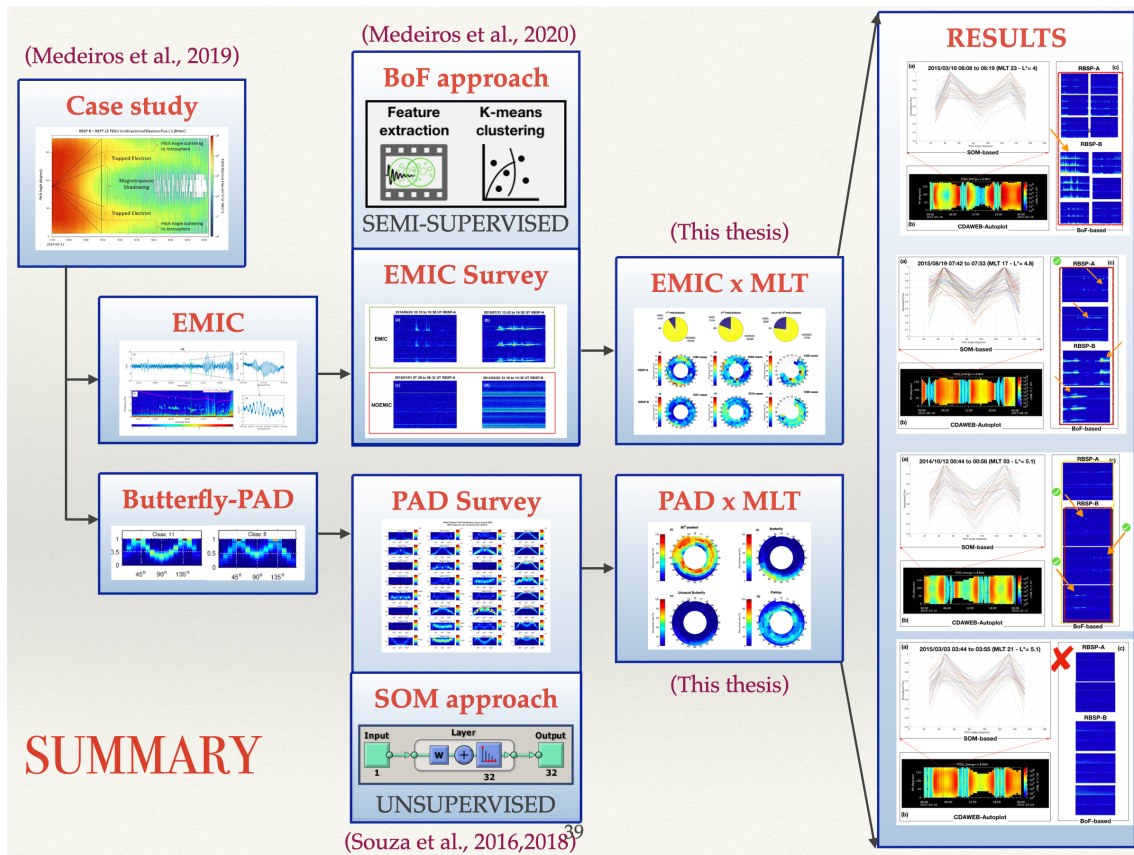
The leftmost panels show the motivation of this study which initiated with a case study reported by Medeiros et al. (2019). As a result of this work, the likely association between EMIC waves and unusual electron butterfly PAD shapes needed to be further investigated. EMIC and electron PAD surveys were performed using the BoF and SOM approaches, respectively. A distribution of EMIC cases and electron PAD shapes per MLT were obtained. Persistent (> 10 min duration) unusual electron butterfly PAD shapes have been selected and correlated with occurrences of EMIC waves.

SOURCE: Author production.

The main results of this thesis can be summarized as follows:

- An unusual electron butterfly PAD shape for relativistic energies has been reported by Medeiros et al. (2019). Such an unusual electron PAD shape resembles the regular electron butterfly PAD, with the exception that it shows an enhanced depletion of electron flux at pitch angles $< 35°$ and $> 135°$, and more importantly such a decrease in flux seems to be associated

with the occurrence of EMIC waves.

- A machine learning-based technique referred to as Bag-of-Features (BoF) has been implemented to classify, in a semi-automated way, stacked up spectrogram images into two groups: one that should contain spectrograms with clear evidences of EMIC waves, thus named as *EMIC*, and the other where no clear EMIC wave signatures would be present, therefore named as *NOEMIC*. The BoF technique has been applied in a large dataset spanning ~ 4 years of magnetic field spectrogram images, amounting to 66,204 images. From those, 30,190 (about 45%) were visually classified to serve as a validation dataset. For this set, the BoF technique correctly classified the input images into the *EMIC* class in 78% of the times, while it showed a better performance, that is, 94% when classifying input images into the *NOEMIC* group. The BoF technique performed nearly as good as the visual classification method in terms of accuracy, with the enormous advantage that the BoF technique greatly expedites the analysis by accomplishing the task in just a few minutes.

- The Self Organizing Map (SOM)-based survey has shown that unusual electron butterfly PAD shapes, as reported by Medeiros et al. (2019), are indeed unusual when considering events wherein there is at least a 10 minutes persistence. These events amount to 0.3% (11,789 cases) of the whole 1.8 MeV energy electron PADs dataset acquired during a full Van Allen Probes' orbit precession from January 2014 to October 2015.

- Such persistent events generally occur throughout the nightside region, at L-shell locations larger than about $5\,R_E$, with a slightly higher occurrence rate in the 01:00–02:00 MLT range. Causes for these spatially localized occurrence rates are left for future work. Earth's magnetosphere nightside region has been previously reported as a favorable region for regular electron butterfly PAD shapes due mostly to drift-shell splitting (WEST JUNIOR et al., 1973; SIBECK et al., 1987). Also, these regular electron butterfly PAD shapes can also be associated with loss of electrons at 90° pitch angle due to magnetopause shadowing (JAYNES et al., 2015; ALVES et al., 2016; MEDEIROS et al., 2019). The unusual electron butterfly PAD shape reported by (MEDEIROS et al., 2019), however, has an additional "ingredient" for its formation which is the presence of EMIC waves.

- Visual inspection of a reduced subset, i.e., 23 events, of the persistent (> 10 minute-long) unusual electron butterfly PAD shapes in conjunction with

the BoF-based EMIC waves survey has shown that these unusual electron butterfly PAD shapes are indeed associated with EMIC waves occurrence for 22 events. Thus it is argued that EMIC waves can be the dominant factor in the relativistic electron flux reduction at pitch angles $< 45°$ and $> 135°$ which in turn lead to the appearance of such unusual electron butterfly PAD shapes.

- This thesis work indicate the need to carefully analyze the presence of EMIC waves whenever an electron butterfly PAD at relativistic energies is found in the outer Van Allen radiation belt. EMIC waves can contribute to a reconfiguration of the regular electron butterfly PAD shape to an unusual butterfly PAD shape. The presence of the latter implies in more relativistic electron loss from the outer radiation belt with such particles likely precipitating into the upper atmosphere. Knowledge of the unusual electron butterfly PADs spatial distribution provides us with a way of inferring regions in the outer Van Allen belt where the flux of relativistic electrons is prone to a higher level of variability.

REFERENCES

ABEL, B.; THORNE, R. M. Electron scattering loss in earth's inner magnetosphere: 1. dominant physical processes. **Journal of Geophysical Research: Space Physics**, v. 103, n. A2, p. 2385–2396, 1998. Disponível em: <https://agupubs.onlinelibrary.wiley.com/doi/abs/10.1029/97JA02919>. 19

ALLEN, J. A. V. Why radiation belts exist. **Eos, Transactions American Geophysical Union**, v. 72, n. 34, p. 361–363, 1991. Disponível em: <https://agupubs.onlinelibrary.wiley.com/doi/abs/10.1029/90EO10279>. 27

ALVES, L. R.; SILVA, L. A. D.; SOUZA, V. M.; SIBECK, D. G.; JAUER, P. R.; VIEIRA, L. E. A.; WALSH, B. M.; SILVEIRA, M. V. D.; MARCHEZI, J. P.; ROCKENBACH, M.; LAGO, A. D.; MENDES, O.; TSURUTANI, B. T.; KOGA, D.; KANEKAL, S. G.; BAKER, D. N.; WYGANT, J. R.; KLETZING, C. A. Outer radiation belt dropout dynamics following the arrival of two interplanetary coronal mass ejections. **Geophysical Research Letters**, v. 43, n. 3, p. 978–987, 2016. ISSN 1944-8007. 2015GL067066. Disponível em: <http://dx.doi.org/10.1002/2015GL067066>. 14, 49, 109

ANDERSON, B. J.; ERLANDSON, R. E.; ZANETTI, L. J. A statistical study of pc 1-2 magnetic pulsations in the equatorial magnetosphere. i - equatorial occurrence distributions. ii - wave properties. **Journal of Geophysical Research**, v. 97, p. 3075–3101, mar. 1992. 41

ASEEV, N. A.; SHPRITS, Y. Y.; DROZDOV, A. Y.; KELLERMAN, A. C.; USANOVA, M. E.; WANG, D.; ZHELAVSKAYA, I. S. Signatures of ultrarelativistic electron loss in the heart of the outer radiation belt measured by Van Allen probes. **Journal of Geophysical Research: Space Physics**, v. 122, n. 10, p. 10,102–10,111, 2017. Disponível em: <https://agupubs.onlinelibrary.wiley.com/doi/abs/10.1002/2017JA024485>. 43

BAKER, D. N.; JAYNES, A. N.; HOXIE, V. C.; THORNE, R. M.; FOSTER, J. C.; LI, X.; FENNELL, J. F.; WYGANT, J. R.; KANEKAL, S. G.; ERICKSON, P. J.; KURTH, W.; LI, W.; MA, Q.; SCHILLER, Q.; BLUM, L.; MALASPINA, D. M.; GERRARD, A.; LANZEROTTI, L. An impenetrable barrier to ultrarelativistic electrons in the Van Allen radiation belts. **Nature**, v. 515,

n. 7528, p. 531–534, Nov 2014. ISSN 1476-4687. Disponível em:
<http://dx.doi.org/10.1038/nature13956>. 17

BAKER, D. N.; JAYNES, A. N.; KANEKAL, S. G.; FOSTER, J. C.; ERICKSON,
P. J.; FENNELL, J. F.; BLAKE, J. B.; ZHAO, H.; LI, X.; ELKINGTON, S. R.;
HENDERSON, M. G.; REEVES, G. D.; SPENCE, H. E.; KLETZING, C. A.;
WYGANT, J. R. Highly relativistic radiation belt electron acceleration, transport,
and loss: large solar storm events of march and june 2015. **Journal of
Geophysical Research: Space Physics**, v. 121, n. 7, p. 6647–6660, 2016.
Disponível em: <https:
//agupubs.onlinelibrary.wiley.com/doi/abs/10.1002/2016JA022502>. 104

BAKER, D. N.; KANEKAL, S. G.; HOXIE, V. C.; BATISTE, S.; BOLTON, M.;
LI, X.; ELKINGTON, S. R.; MONK, S.; REUKAUF, R.; STEG, S.; WESTFALL,
J.; BELTING, C.; BOLTON, B.; BRAUN, D.; CERVELLI, B.; HUBBELL, K.;
KIEN, M.; KNAPPMILLER, S.; WADE, S.; LAMPRECHT, B.; STEVENS, K.;
WALLACE, J.; YEHLE, A.; SPENCE, H. E.; FRIEDEL, R. The relativistic
electron-proton telescope (rept) instrument on board the radiation belt storm
probes (rbsp) spacecraft: characterization of earth's radiation belt high-energy
particle populations. **Space Science Reviews**, v. 179, n. 1, p. 337–381, 2013.
ISSN 1572-9672. Disponível em:
<http://dx.doi.org/10.1007/s11214-012-9950-9>. 15, 42, 46, 93

BAY, H.; ESS, A.; TUYTELAARS, T.; GOOL, L. V. Speeded-up robust features
(surf). **Computer Vision and Image Understanding**, v. 110, n. 3, p. 346 –
359, 2008. ISSN 1077-3142. Disponível em: <http:
//www.sciencedirect.com/science/article/pii/S1077314207001555>. 77, 78

BINGLEY, L.; ANGELOPOULOS, V.; SIBECK, D.; ZHANG, X.; HALFORD, A.
The evolution of a pitch-angle "bite-out" scattering signature caused by EMIC
wave activity: a case study. **Journal of Geophysical Research (Space
Physics)**, v. 124, n. 7, p. 5042–5055, jul. 2019. 96, 105, 106

BITTENCOURT, J. A. Fundamentals of plasma physics. Springer New York, 2004.
Disponível em: <http://dx.doi.org/10.1007/978-1-4757-4030-1>. 21, 34

BLAKE, J. B.; CARRANZA, P. A.; CLAUDEPIERRE, S. G.; CLEMMONS,
J. H.; CRAIN, W. R.; DOTAN, Y.; FENNELL, J. F.; FUENTES, F. H.;
GALVAN, R. M.; GEORGE, J. S.; HENDERSON, M. G.; LALIC, M.; LIN, A. Y.;
LOOPER, M. D.; MABRY, D. J.; MAZUR, J. E.; MCCARTHY, B.; NGUYEN,

C. Q.; O'BRIEN, T. P.; PEREZ, M. A.; REDDING, M. T.; ROEDER, J. L.; SALVAGGIO, D. J.; SORENSEN, G. A.; SPENCE, H. E.; YI, S.; ZAKRZEWSKI, M. P. The magnetic electron ion spectrometer (mageis) instruments aboard the radiation belt storm probes (rbsp) spacecraft. **Space Science Reviews**, v. 179, n. 1, p. 383–421, 2013. ISSN 1572-9672. Disponível em: <http://dx.doi.org/10.1007/s11214-013-9991-8>. 46

BLUM, L. W.; HALFORD, A.; MILLAN, R.; BONNELL, J. W.; GOLDSTEIN, J.; USANOVA, M.; ENGEBRETSON, M.; OHNSTED, M.; REEVES, G.; SINGER, H.; CLILVERD, M.; LI, X. Observations of coincident emic wave activity and duskside energetic electron precipitation on 18–19 january 2013. **Geophysical Research Letters**, v. 42, n. 14, p. 5727–5735, 2015. Disponível em: <https://agupubs.onlinelibrary.wiley.com/doi/abs/10.1002/2015GL065245>. 43, 105, 106

BORTNIK, J.; THORNE, R. The dual role of elf/vlf chorus waves in the acceleration and precipitation of radiation belt electrons. **Journal of Atmospheric and Solar-Terrestrial Physics**, v. 69, n. 3, p. 378 – 386, 2007. ISSN 1364-6826. Disponível em: <http://www.sciencedirect.com/science/article/pii/S136468260600277X>. 35

BORTNIK, J.; THORNE, R. M.; O'BRIEN, T. P.; GREEN, J. C.; STRANGEWAY, R. J.; SHPRITS, Y. Y.; BAKER, D. N. Observation of two distinct, rapid loss mechanisms during the 20 november 2003 radiation belt dropout event. **Journal of Geophysical Research: Space Physics**, v. 111, n. A12, 2006. Disponível em: <https://agupubs.onlinelibrary.wiley.com/doi/abs/10.1029/2006JA011802>. 41, 43

BRAUTIGAM, D. H.; GINET, G. P.; ALBERT, J. M.; WYGANT, J. R.; ROWLAND, D. E.; LING, A.; BASS, J. Crres electric field power spectra and radial diffusion coefficients. **Journal of Geophysical Research: Space Physics**, v. 110, n. A2, 2005. Disponível em: <https://agupubs.onlinelibrary.wiley.com/doi/abs/10.1029/2004JA010612>. 39

CLAUDEPIERRE, S. G.; ELKINGTON, S. R.; WILTBERGER, M. Solar wind driving of magnetospheric ULF waves: pulsations driven by velocity shear at the magnetopause. **Journal of Geophysical Research: Space Physics**, Wiley-Blackwell, v. 113, n. A5, p. n/a–n/a, may 2008. Disponível em: <http://dx.doi.org/10.1029/2007JA012890>. 38

CLAUDEPIERRE, S. G.; WILTBERGER, M.; ELKINGTON, S. R.; LOTKO, W.;
HUDSON, M. K. Magnetospheric cavity modes driven by solar wind dynamic
pressure fluctuations. **Geophysical Research Letters**, v. 36, n. 13, 2009.
Disponível em: <https:
//agupubs.onlinelibrary.wiley.com/doi/abs/10.1029/2009GL039045>. 38

CLILVERD, M. A.; DUTHIE, R.; HARDMAN, R.; HENDRY, A. T.; RODGER,
C. J.; RAITA, T.; ENGEBRETSON, M.; LESSARD, M. R.; DANSKIN, D.;
MILLING, D. K. Electron precipitation from emic waves: a case study from 31
may 2013. **Journal of Geophysical Research: Space Physics**, v. 120, n. 5, p.
3618–3631, 2015. Disponível em: <https:
//agupubs.onlinelibrary.wiley.com/doi/abs/10.1002/2015JA021090>. 43,
105, 106

CLILVERD, M. A.; RODGER, C. J.; MCCARTHY, M.; MILLAN, R.; BLUM,
L. W.; COBBETT, N.; BRUNDELL, J. B.; DANSKIN, D.; HALFORD, A. J.
Investigating energetic electron precipitation through combining ground-based and
balloon observations. **Journal of Geophysical Research: Space Physics**,
v. 122, n. 1, p. 534–546, 2017. ISSN 2169-9402. 2016JA022812. Disponível em:
<http://dx.doi.org/10.1002/2016JA022812>. 43, 49, 68

CSURKA, G.; BRAY, C.; DANCE, C.; FAN, L. Visual categorization with bags of
keypoints. In: WORKSHOP ON STATISTICAL LEARNING IN COMPUTER
VISION. **Proceedings**. [S.l.], 2004. p. 1–22. 73

DROZDOV, A. Y.; SHPRITS, Y. Y.; ORLOVA, K. G.; KELLERMAN, A. C.;
SUBBOTIN, D. A.; BAKER, D. N.; SPENCE, H. E.; REEVES, G. D. Energetic,
relativistic, and ultrarelativistic electrons: comparison of long-term verb code
simulations with van allen probes measurements. **Journal of Geophysical
Research: Space Physics**, v. 120, n. 5, p. 3574–3587, 2015. Disponível em:
<https:
//agupubs.onlinelibrary.wiley.com/doi/abs/10.1002/2014JA020637>. 42

DUDA, R. O.; HART, P. E. **Pattern classification and scene analysis**. New
Yotk: John Willey & Sons, 1973. 81

DUNGEY, J. W. Interplanetary magnetic field and the auroral zones. **Physical
Review Letters**, v. 6, n. 2, p. 47–48, 1961. 11

ELKINGTON, S. R. A review of ulf interactions with radiation belt electrons. In:
_____. **Magnetospheric ULF waves: synthesis and new directions**.

American Geophysical Union (AGU), 2013. p. 177–193. ISBN 9781118666319. Disponível em: <https://agupubs.onlinelibrary.wiley.com/doi/abs/10.1029/169GM12>. 17, 19, 39

FELDSTEIN, Y.; STARKOV, G. The auroral oval and the boundary of closed field lines of geomagnetic field. **Planetary and Space Science**, v. 18, n. 4, p. 501 – 508, 1970. ISSN 0032-0633. Disponível em: <http://www.sciencedirect.com/science/article/pii/0032063370901273>. 14

FELDSTEIN, Y. I.; GRAFE, A.; GROMOVA, L. I.; POPOV, V. A. Auroral electrojets during geomagnetic storms. **Journal of Geophysical Research: Space Physics**, v. 102, n. A7, p. 14223–14235, 1997. Disponível em: <https://agupubs.onlinelibrary.wiley.com/doi/abs/10.1029/97JA00577>. 14

FRASER, B. J.; KEMP, W. J.; WEBSTER, D. J. Ground-satellite study of a pc 1 ion cyclotron wave event. **Journal of Geophysical Research: Space Physics**, v. 94, n. A9, p. 11855–11863, 1989. Disponível em: <https://agupubs.onlinelibrary.wiley.com/doi/abs/10.1029/JA094iA09p11855>. 41

GANNON, J. L.; LI, X.; HEYNDERICKX, D. Pitch angle distribution analysis of radiation belt electrons based on combined release and radiation effects satellite medium electrons a data. **Journal of Geophysical Research: Space Physics**, v. 112, p. A05212, maio 2007. 43, 52, 55, 56, 97

GIBSON, S. E.; KOZYRA, J. U.; TOMA, G. de; EMERY, B. A.; ONSAGER, T.; THOMPSON, B. J. If the sun is so quiet, why is the earth ringing? a comparison of two solar minimum intervals. **Journal of Geophysical Research: Space Physics**, v. 114, n. A9, 2009. Disponível em: <https://agupubs.onlinelibrary.wiley.com/doi/abs/10.1029/2009JA014342>. 8

GONZALEZ, W. D.; JOSELYN, J. A.; KAMIDE, Y.; KROEHL, H. W.; ROSTOKER, G.; TSURUTANI, B. T.; VASYLIUNAS, V. M. What is a geomagnetic storm? **Journal of Geophysical Research: Space Physics**, v. 99, n. A4, p. 5771–5792, 1994. Disponível em: <https://agupubs.onlinelibrary.wiley.com/doi/abs/10.1029/93JA02867>. 11, 12

HALFORD, A. J.; FRASER, B. J.; MORLEY, S. K. Emic wave activity during geomagnetic storm and nonstorm periods: Crres results. **Journal of Geophysical Research: Space Physics**, v. 115, n. A12, 2010. Disponível em: <https://agupubs.onlinelibrary.wiley.com/doi/abs/10.1029/2010JA015716>. 41

HALFORD, A. J.; FRASER, B. J.; MORLEY, S. K.; ELKINGTON, S. R.; CHAN, A. A. Dependence of emic wave parameters during quiet, geomagnetic storm, and geomagnetic storm phase times. **Journal of Geophysical Research: Space Physics**, v. 121, n. 7, p. 6277–6291, 2016. ISSN 2169-9402. 2016JA022694. Disponível em: <http://dx.doi.org/10.1002/2016JA022694>. 41, 43

HORNE, R. B.; THORNE, R. M. Potential waves for relativistic electron scattering and stochastic acceleration during magnetic storms. **Geophysical Research Letters**, v. 25, n. 15, p. 3011–3014, 1998. Disponível em: <https://agupubs.onlinelibrary.wiley.com/doi/abs/10.1029/98GL01002>. 19

_____. Relativistic electron acceleration and precipitation during resonant interactions with whistler-mode chorus. **Geophysical Research Letters**, v. 30, n. 10, 2003. Disponível em: <https://agupubs.onlinelibrary.wiley.com/doi/abs/10.1029/2003GL016973>. 35, 43, 52

HORNE, R. B.; THORNE, R. M.; GLAUERT, S. A.; ALBERT, J. M.; MEREDITH, N. P.; ANDERSON, R. R. Timescale for radiation belt electron acceleration by whistler mode chorus waves. **Journal of Geophysical Research: Space Physics**, v. 110, n. A3, 2005. Disponível em: <https://agupubs.onlinelibrary.wiley.com/doi/abs/10.1029/2004JA010811>. 19, 35

HU, Y.; DENTON, R. E.; JOHNSON, J. R. Two-dimensional hybrid code simulation of electromagnetic ion cyclotron waves of multi-ion plasmas in a dipole magnetic field. **Journal of Geophysical Research: Space Physics**, v. 115, n. A9, 2010. Disponível em: <https://agupubs.onlinelibrary.wiley.com/doi/abs/10.1029/2009JA015158>. 41

HUDSON, M. K.; ELKINGTON, S. R.; LYON, J. G.; WILTBERGER, M.; LESSARD, M. Radiation belt electron acceleration by ulf wave drift resonance: simulation of 1997 and 1998 storms. In: _____. **Space weather**. American Geophysical Union (AGU), 2013. p. 289–296. ISBN 9781118668351. Disponível em:

<https:
//agupubs.onlinelibrary.wiley.com/doi/abs/10.1029/GM125p0289>. 19

HUGHES, W. J. Magnetospheric ulf waves: a tutorial with a historical perspective. In: _____. **Solar wind sources of magnetospheric ultra-low-frequency waves**. American Geophysical Union (AGU), 2013. p. 1–11. ISBN 9781118663943. Disponível em: <https:
//agupubs.onlinelibrary.wiley.com/doi/abs/10.1029/GM081p0001>. 39

HWANG, J. A.; LEE, D.-Y.; LYONS, L. R.; SMITH, A. J.; ZOU, S.; MIN, K. W.; KIM, K.-H.; MOON, Y.-J.; PARK, Y. D. Statistical significance of association between whistler-mode chorus enhancements and enhanced convection periods during high-speed streams. **Journal of Geophysical Research: Space Physics**, v. 112, n. A9, 2007. Disponível em: <https:
//agupubs.onlinelibrary.wiley.com/doi/abs/10.1029/2007JA012388>. 35

JACOBS, J. A.; KATO, Y.; MATSUSHITA, S.; TROITSKAYA, V. A. Classification of geomagnetic micropulsations. **Journal of Geophysical Research**, v. 69, n. 1, p. 180–181, 1964. Disponível em: <https:
//agupubs.onlinelibrary.wiley.com/doi/abs/10.1029/JZ069i001p00180>. 39

JAYNES, A. N.; BAKER, D. N.; SINGER, H. J.; RODRIGUEZ, J. V.; LOTO'ANIU, T. M.; ALI, A. F.; ELKINGTON, S. R.; LI, X.; KANEKAL, S. G.; CLAUDEPIERRE, S. G.; FENNELL, J. F.; LI, W.; THORNE, R. M.; KLETZING, C. A.; SPENCE, H. E.; REEVES, G. D. Source and seed populations for relativistic electrons: their roles in radiation belt changes. **Journal of Geophysical Research: Space Physics**, v. 120, n. 9, p. 7240–7254, 2015. ISSN 2169-9402. 2015JA021234. Disponível em:
<http://dx.doi.org/10.1002/2015JA021234>. 49, 109

JORDANOVA, V. K.; ALBERT, J.; MIYOSHI, Y. Relativistic electron precipitation by emic waves from self-consistent global simulations. **Journal of Geophysical Research: Space Physics**, v. 113, n. A3, 2008. Disponível em:
<https:
//agupubs.onlinelibrary.wiley.com/doi/abs/10.1029/2008JA013239>. 17, 19, 41, 43

JORDANOVA, V. K.; KISTLER, L. M.; FARRUGIA, C. J.; TORBERT, R. B. Effects of inner magnetospheric convection on ring current dynamics: March 10–12,

1998. **Journal of Geophysical Research: Space Physics**, v. 106, n. A12, p. 29705–29720, 2001. Disponível em: <https: //agupubs.onlinelibrary.wiley.com/doi/abs/10.1029/2001JA000047>. 41

KAMIDE, Y.; CHIAN, A. **Handbook of the solar-terrestrial environment**. Springer Berlin Heidelberg, 2007. Disponível em: <https://doi.org/10.1007/978-3-540-46315-3>. 3, 4, 5, 7

KANG, S.-B.; FOK, M.-C.; GLOCER, A.; MIN, K.-W.; CHOI, C.-R.; CHOI, E.; HWANG, J. Simulation of a rapid dropout event for highly relativistic electrons with the rbe model. **Journal of Geophysical Research: Space Physics**, v. 121, n. 5, p. 4092–4102, 2016. ISSN 2169-9402. 2015JA021966. Disponível em: <http://dx.doi.org/10.1002/2015JA021966>. 61, 62, 67

KASAHARA, Y.; SAWADA, A.; YAMAMOTO, M.; KIMURA, I.; KOKUBUN, S.; HAYASHI, K. Ion cyclotron emissions observed by the satellite akebono in the vicinity of the magnetic equator. **Radio Science**, v. 27, n. 2, p. 347–362, 1992. Disponível em: <https://agupubs.onlinelibrary.wiley.com/doi/abs/10.1029/91RS01872>. 41

KEIKA, K.; TAKAHASHI, K.; UKHORSKIY, A. Y.; MIYOSHI, Y. Global characteristics of electromagnetic ion cyclotron waves: occurrence rate and its storm dependence. **Journal of Geophysical Research: Space Physics**, v. 118, n. 7, p. 4135–4150, 2013. Disponível em: <https: //agupubs.onlinelibrary.wiley.com/doi/abs/10.1002/jgra.50385>. 41

KENNEL, C. F.; PETSCHEK, H. E. Limit on stably trapped particle fluxes. **Journal of Geophysical Research**, v. 71, n. 1, p. 1–28, 1966. Disponível em: <https: //agupubs.onlinelibrary.wiley.com/doi/abs/10.1029/JZ071i001p00001>. 21, 34, 40, 53

KIVELSON, A.; KIVELSON, M.; RUSSELL, C. **Introduction to space physics**. Cambridge: Cambridge University Press„ 1995. (Cambridge atmospheric and space science series). ISBN 9780521457149. Disponível em: <https://books.google.com.br/books?id=qWHSqXGfsfQC>. 6

KLETZING, C. A.; KURTH, W. S.; ACUNA, M.; MACDOWALL, R. J.; TORBERT, R. B.; AVERKAMP, T.; BODET, D.; BOUNDS, S. R.; CHUTTER, M.; CONNERNEY, J.; CRAWFORD, D.; DOLAN, J. S.; DVORSKY, R.;

HOSPODARSKY, G. B.; HOWARD, J.; JORDANOVA, V.; JOHNSON, R. A.; KIRCHNER, D. L.; MOKRZYCKI, B.; NEEDELL, G.; ODOM, J.; MARK, D.; PFAFF, R.; PHILLIPS, J. R.; PIKER, C. W.; REMINGTON, S. L.; ROWLAND, D.; SANTOLIK, O.; SCHNURR, R.; SHEPPARD, D.; SMITH, C. W.; THORNE, R. M.; TYLER, J. The electric and magnetic field instrument suite and integrated science (emfisis) on rbsp. **Space Science Reviews**, v. 179, n. 1, p. 127–181, 2013. ISSN 1572-9672. Disponível em: <http://dx.doi.org/10.1007/s11214-013-9993-6>. 38, 40, 47, 48

KURTH, W. S.; GURNETT, D. A. Plasma waves in planetary magnetospheres. **Journal of Geophysical Research: Space Physics**, v. 96, n. S01, p. 18977–18991, 1991. Disponível em: <https://agupubs.onlinelibrary.wiley.com/doi/abs/10.1029/91JA01819>. 34

LI, W.; MA, Q.; THORNE, R. M.; BORTNIK, J.; ZHANG, X.-J.; LI, J.; BAKER, D. N.; REEVES, G. D.; SPENCE, H. E.; KLETZING, C. A.; KURTH, W. S.; HOSPODARSKY, G. B.; BLAKE, J. B.; FENNELL, J. F.; KANEKAL, S. G.; ANGELOPOULOS, V.; GREEN, J. C.; GOLDSTEIN, J. Radiation belt electron acceleration during the 17 march 2015 geomagnetic storm: observations and simulations. **Journal of Geophysical Research: Space Physics**, v. 121, n. 6, p. 5520–5536, 2016. Disponível em: <https://agupubs.onlinelibrary.wiley.com/doi/abs/10.1002/2016JA022400>. 104, 106

LI, W.; THORNE, R. M.; ANGELOPOULOS, V.; BORTNIK, J.; CULLY, C. M.; NI, B.; LECONTEL, O.; ROUX, A.; AUSTER, U.; MAGNES, W. Global distribution of whistler-mode chorus waves observed on the themis spacecraft. **Geophysical Research Letters**, v. 36, n. 9, 2009. Disponível em: <https://agupubs.onlinelibrary.wiley.com/doi/abs/10.1029/2009GL037595>. 35

LI, Z.; MILLAN, R. M.; HUDSON, M. K.; WOODGER, L. A.; SMITH, D. M.; CHEN, Y.; FRIEDEL, R.; RODRIGUEZ, J. V.; ENGEBRETSON, M. J.; GOLDSTEIN, J.; FENNELL, J. F.; SPENCE, H. E. Investigation of emic wave scattering as the cause for the barrel 17 january 2013 relativistic electron precipitation event: a quantitative comparison of simulation with observations. **Geophysical Research Letters**, v. 41, n. 24, p. 8722–8729, 2014. ISSN 1944-8007. 2014GL062273. Disponível em: <http://dx.doi.org/10.1002/2014GL062273>. 49, 68

LOTO'ANIU, T. M.; FRASER, B. J.; WATERS, C. L. Propagation of electromagnetic ion cyclotron wave energy in the magnetosphere. **Journal of Geophysical Research: Space Physics**, v. 110, n. A7, 2005. Disponível em: <https://agupubs.onlinelibrary.wiley.com/doi/abs/10.1029/2004JA010816>. 40

LOTO'ANIU, T. M.; SINGER, H. J.; WATERS, C. L.; ANGELOPOULOS, V.; MANN, I. R.; ELKINGTON, S. R.; BONNELL, J. W. Relativistic electron loss due to ultralow frequency waves and enhanced outward radial diffusion. **Journal of Geophysical Research: Space Physics**, v. 115, n. A12, 2010. Disponível em: <https://agupubs.onlinelibrary.wiley.com/doi/abs/10.1029/2010JA015755>. 19

LYONS, L. R.; THORNE, R. M. Parasitic pitch angle diffusion of radiation belt particles by ion cyclotron waves. **Journal of Geophysical Research**, v. 77, n. 28, p. 5608–5616, oct 1972. Disponível em: <http://dx.doi.org/10.1029/JA077i028p05608>. 19, 41, 43

LYONS, L. R.; WILLIAMS, D. J. **Quantitative aspects of magnetospheric physics**. Berlin: Springer, 1984. ISBN 9789401728195. Disponível em: <http://dx.doi.org/10.1007/978-94-017-2819-5>. 21

MATHIE, R. A.; MANN, I. R. A correlation between extended intervals of ulf wave power and storm-time geosynchronous relativistic electron flux enhancements. **Geophysical Research Letters**, v. 27, n. 20, p. 3261–3264, 2000. Disponível em: <https://agupubs.onlinelibrary.wiley.com/doi/abs/10.1029/2000GL003822>. 40

MAUK, B. H.; FOX, N. J.; KANEKAL, S. G.; KESSEL, R. L.; SIBECK, D. G.; UKHORSKIY, A. Science objectives and rationale for the radiation belt storm probes mission. **Space Science Reviews**, v. 179, n. 1-4, p. 3–27, sep 2012. Disponível em: <http://dx.doi.org/10.1007/s11214-012-9908-y>. 45, 46

MAUK, B. H.; MCPHERRON, R. L. An experimental test of the electromagnetic ion cyclotron instability within the earth's magnetosphere. **The Physics of Fluids**, v. 23, n. 10, p. 2111–2127, 1980. Disponível em: <https://aip.scitation.org/doi/abs/10.1063/1.862873>. 41

MEDEIROS, C.; M., S. V.; VIEIRA, L. E.; SIBECK, D. G.; REMYA, B.; SILVA, L. A. D.; ALVES, L. R.; MARCHEZI, J. P.; JAUER, P. R.; ROCKENBACH, M.; LAGO, A. D.; KLETZING, C. A. Electromagnetic ion-cyclotron waves pattern

recognition based on a deep learning technique: Bag-of-features algorithm applied to spectrograms. Submitted to ApJS,. May 2020. xiii, xv, 1, 2, 75, 76, 79, 81, 82, 83, 84, 85, 87, 88, 89, 90, 91, 92, 107

MEDEIROS, C.; SOUZA, V. M.; VIEIRA, L. E. A.; SIBECK, D. G.; HALFORD, A. J.; KANG, S.-B.; SILVA, L. A. D.; ALVES, L. R.; MARCHEZI, J. P.; DALLAQUA, R. S.; JAUER, P. R.; ROCKENBACH, M.; MENDES, O.; ALVES, M. V.; LAGO, A. D.; FOK, M.-C.; KANEKAL, S. G.; BAKER, D. N.; KLETZING, C. A. On the contribution of emic waves to the reconfiguration of the relativistic electron butterfly pitch angle distribution shape on 2014 september 12—a case study. **The Astrophysical Journal**, v. 872, n. 1, p. 36, Feb 2019. ISSN 1538-4357. Disponível em: <http://dx.doi.org/10.3847/1538-4357/aaf970>. xiii, xv, 1, 2, 14, 43, 49, 50, 51, 52, 54, 55, 56, 58, 59, 60, 62, 63, 64, 65, 66, 67, 68, 69, 70, 71, 75, 96, 97, 103, 105, 106, 107, 108, 109

MEREDITH, N. P.; HORNE, R. B.; KERSTEN, T.; FRASER, B. J.; GREW, R. S. Global morphology and spectral properties of emic waves derived from crres observations. **Journal of Geophysical Research: Space Physics**, v. 119, n. 7, p. 5328–5342, 2014. Disponível em: <https://agupubs.onlinelibrary.wiley.com/doi/abs/10.1002/2014JA020064>. 41

MEREDITH, N. P.; HORNE, R. B.; THORNE, R. M.; SUMMERS, D.; ANDERSON, R. R. Substorm dependence of plasmaspheric hiss. **Journal of Geophysical Research: Space Physics**, v. 109, n. A6, 2004. Disponível em: <https://agupubs.onlinelibrary.wiley.com/doi/abs/10.1029/2004JA010387>. 36

MIN, K.; BORTNIK, J.; LEE, J. A novel technique for rapid lstar calculation: algorithm and implementation. **Journal of Geophysical Research: Space Physics**, v. 118, n. 5, p. 1912–1921, 2013. ISSN 2169-9402. Disponível em: <http://dx.doi.org/10.1002/jgra.50250>. 61

_____. A novel technique for rapid lstar calculation using ubk coordinates. **Journal of Geophysical Research: Space Physics**, v. 118, n. 1, p. 192–197, 2013. ISSN 2169-9402. Disponível em: <http://dx.doi.org/10.1029/2012JA018177>. 61

MIN, K.; LEE, J.; KEIKA, K.; LI, W. Global distribution of emic waves derived from themis observations. **Journal of Geophysical Research: Space Physics**,

v. 117, n. A5, 2012. Disponível em: <https:
//agupubs.onlinelibrary.wiley.com/doi/abs/10.1029/2012JA017515>. 41

MIYOSHI, Y.; JORDANOVA, V.; THOMSEN, M.; REEVES, G.; EVANS, D.;
MORIOKA, A.; KASAHARA, Y.; NAGAI, T.; GREEN, J. Simulation of energetic
electrons dynamics on the oct. 2001 magnetic storm. In: **Abstracts**. [S.l.: s.n.],
2003. p. p.SM51C–0540. 19

MIYOSHI, Y.; SAKAGUCHI, K.; SHIOKAWA, K.; EVANS, D.; ALBERT, J.;
CONNORS, M.; JORDANOVA, V. Precipitation of radiation belt electrons by
emic waves, observed from ground and space. **Geophysical Research Letters**,
v. 35, n. 23, 2008. Disponível em: <https:
//agupubs.onlinelibrary.wiley.com/doi/abs/10.1029/2008GL035727>. 43

NI, B.; THORNE, R. M.; SHPRITS, Y. Y.; BORTNIK, J. Resonant scattering of
plasma sheet electrons by whistler-mode chorus: contribution to diffuse auroral
precipitation. **Geophysical Research Letters**, v. 35, n. 11, 2008. Disponível em:
<https:
//agupubs.onlinelibrary.wiley.com/doi/abs/10.1029/2008GL034032>. 35

NI, B.; ZOU, Z.; GU, X.; ZHOU, C.; THORNE, R. M.; BORTNIK, J.; SHI, R.;
ZHAO, Z.; BAKER, D. N.; KANEKAL, S. G.; SPENCE, H. E.; REEVES, G. D.;
LI, X. Variability of the pitch angle distribution of radiation belt ultrarelativistic
electrons during and following intense geomagnetic storms: Van Allen probes
observations. **Journal of Geophysical Research: Space Physics**, v. 120, n. 6,
p. 4863–4876, 2015. Disponível em: <https:
//agupubs.onlinelibrary.wiley.com/doi/abs/10.1002/2015JA021065>. 97

O'BRIEN, T. P.; MCPHERRON, R. L.; SORNETTE, D.; REEVES, G. D.;
FRIEDEL, R.; SINGER, H. J. Which magnetic storms produce relativistic
electrons at geosynchronous orbit? **Journal of Geophysical Research: Space
Physics**, v. 106, n. A8, p. 15533–15544, 2001. Disponível em: <https:
//agupubs.onlinelibrary.wiley.com/doi/abs/10.1029/2001JA000052>. 19

O'HARA, S.; DRAPER, B. A. Introduction to the bag of features paradigm for
image classification and retrieval. **CoRR**, abs/1101.3354, 2011. Disponível em:
<http://arxiv.org/abs/1101.3354>. 73

ONSAGER, T. G.; GREEN, J. C.; REEVES, G. D.; SINGER, H. J. Solar wind
and magnetospheric conditions leading to the abrupt loss of outer radiation belt
electrons. **Journal of Geophysical Research: Space Physics**, v. 112, n. A1, p.

n/a–n/a, jan 2007. Disponível em:
<http://dx.doi.org/10.1029/2006JA011708>. 35

OZEKE, L. G.; MANN, I. R.; MURPHY, K. R.; SIBECK, D. G.; BAKER, D. N.
Ultra-relativistic radiation belt extinction and ulf wave radial diffusion: modeling
the september 2014 extended dropout event. **Geophysical Research Letters**,
v. 44, n. 6, p. 2624–2633, 2017. ISSN 1944-8007. 2017GL072811. Disponível em:
<http://dx.doi.org/10.1002/2017GL072811>. 49

PARKER, E. N. Dynamics of the interplanetary gas and magnetic fields. **The
Astrophysical Journal**, v. 128, p. 664, Nov 1958. ISSN 1538-4357. Disponível
em: <http://dx.doi.org/10.1086/146579>. 6, 7

PARKS, G. **Physics of space plasmas: an introduction**. 2. ed. Avalon
Publishing, 2003. ISBN 9780813341309. Disponível em:
<https://books.google.com.br/books?id=yY8rvgAACAAJ>. 19, 21, 34

_____. Magnetosphere. In: NORTH, G. R.; PYLE, J.; ZHANG, F. (Ed.).
Encyclopedia of atmospheric sciences. 2. ed. Oxford: Academic Press, 2015.
p. 309 – 315. ISBN 978-0-12-382225-3. Disponível em: <http:
//www.sciencedirect.com/science/article/pii/B9780123822253002115>. 10

RAUCH, J. L.; ROUX, A. Ray tracing of ulf waves in a multicomponent
magnetospheric plasma: consequences for the generation mechanism of ion
cyclotron waves. **Journal of Geophysical Research: Space Physics**, v. 87,
n. A10, p. 8191–8198, 1982. Disponível em: <https:
//agupubs.onlinelibrary.wiley.com/doi/abs/10.1029/JA087iA10p08191>.
41

REGI, M. Ulf power fluctuations in the solar-wind parameters and their
relationship with the relativistic electron flux at the geosynchronous orbit. **II
Nuobo Cimento C**, 08 2016. Disponível em:
<https://doi.org/10.1393/ncc/i2016-16285-x>. 18

REZENDE, S. **Sistemas inteligentes: fundamentos e aplicações**. Manole,
2003. ISBN 9788520416839. Disponível em:
<https://books.google.com.br/books?id=UsJe_PlbnWcC>. 86

RODGER, C. J.; HENDRY, A. T.; CLILVERD, M. A.; KLETZING, C. A.;
BRUNDELL, J. B.; REEVES, G. D. High-resolution in situ observations of
electron precipitation-causing emic waves. **Geophysical Research Letters**,

v. 42, n. 22, p. 9633–9641, 2015. Disponível em: <https:
//agupubs.onlinelibrary.wiley.com/doi/abs/10.1002/2015GL066581>. 42,
43

RODGER, C. J.; RAITA, T.; CLILVERD, M. A.; SEPPÄLÄ, A.; DIETRICH, S.;
THOMSON, N. R.; ULICH, T. Observations of relativistic electron precipitation
from the radiation belts driven by emic waves. **Geophysical Research Letters**,
v. 35, n. 16, 2008. Disponível em: <https:
//agupubs.onlinelibrary.wiley.com/doi/abs/10.1029/2008GL034804>. 43

ROEDERER, J. G. On the adiabatic motion of energetic particles in a model
magnetosphere. **Journal of Geophysical Research**, v. 72, n. 3, p. 981–992,
1967. Disponível em: <https:
//agupubs.onlinelibrary.wiley.com/doi/abs/10.1029/JZ072i003p00981>.
53

ROEDERER, J. G.; SCHULZ, M. Splitting of drift shells by the magnetospheric
electric field. **Journal of Geophysical Research**, v. 76, n. 4, p. 1055–1059, 1971.
ISSN 2156-2202. Disponível em:
<http://dx.doi.org/10.1029/JA076i004p01055>. 17, 34, 43

ROELOF, E. C.; SIBECK, D. G. Magnetopause shape as a bivariate function of
interplanetary magnetic field bz and solar wind dynamic pressure. **Journal of
Geophysical Research: Space Physics**, v. 98, n. A12, p. 21421–21450, 1993.
Disponível em:
<https://agupubs.onlinelibrary.wiley.com/doi/abs/10.1029/93JA02362>.
14

ROSE, D.; CLARK, M. **Plasmas and controlled fusion**. M.I.T. Press, 1961.
Disponível em: <https://books.google.com.br/books?id=aSZRAAAAMAAJ>. 32

ROSTOKER, G.; SKONE, S.; BAKER, D. N. On the origin of relativistic
electrons in the magnetosphere associated with some geomagnetic storms.
Geophysical Research Letters, v. 25, n. 19, p. 3701–3704, 1998. Disponível em:
<https://agupubs.onlinelibrary.wiley.com/doi/abs/10.1029/98GL02801>.
19

RUNOV, A.; ZHANG, X. J.; ANGELOPOULOS, V. Evolution of partial ring
current ion pitch angle distributions during the main phase of a storm on 17 march
2015. **Journal of Geophysical Research: Space Physics**, v. 121, n. 6, p.
5284–5293, 2016. Disponível em: <https:

//agupubs.onlinelibrary.wiley.com/doi/abs/10.1002/2016JA022391>. 104,
106

SAIKIN, A. A.; ZHANG, J.-C.; ALLEN, R. C.; SMITH, C. W.; KISTLER, L. M.;
SPENCE, H. E.; TORBERT, R. B.; KLETZING, C. A.; JORDANOVA, V. K. The
occurrence and wave properties of h^+-, he^+-, and o^+-band emic waves observed by
the van allen probes. **Journal of Geophysical Research: Space Physics**,
v. 120, p. 7477–7492, set. 2015. 41, 65

SAIKIN, A. A.; ZHANG, J.-C.; SMITH, C. W.; SPENCE, H. E.; TORBERT,
R. B.; KLETZING, C. A. The dependence on geomagnetic conditions and solar
wind dynamic pressure of the spatial distributions of emic waves observed by the
Van Allen probes. **Journal of Geophysical Research: Space Physics**, v. 121,
n. 5, p. 4362–4377, 2016. Disponível em: <https:
//agupubs.onlinelibrary.wiley.com/doi/abs/10.1002/2016JA022523>. 41,
43

SAKAGUCHI, K.; SHIOKAWA, K.; MIYOSHI, Y.; OTSUKA, Y.; OGAWA, T.;
ASAMURA, K.; CONNORS, M. Simultaneous appearance of isolated auroral arcs
and pc 1 geomagnetic pulsations at subauroral latitudes. **Journal of Geophysical
Research: Space Physics**, v. 113, n. A5, 2008. Disponível em: <https:
//agupubs.onlinelibrary.wiley.com/doi/abs/10.1029/2007JA012888>. 41

SCHULZ, M.; LANZEROTTI, L. **Particle diffusion in the radiation belts**.
Berlin: Springer-Verlag,, 1974. (Physics and chemistry in space). ISBN
9783540063988. Disponível em:
<https://books.google.com.br/books?id=wUZ5AAAAIAAJ>. 9, 19

SELESNICK, R. S.; BLAKE, J. B. Relativistic electron drift shell splitting.
Journal of Geophysical Research: Space Physics, v. 107, n. A9, p. SMP
27–1–SMP 27–10, 2002. Disponível em: <https:
//agupubs.onlinelibrary.wiley.com/doi/abs/10.1029/2001JA009179>. 52

SHPRITS, Y. Y.; CHEN, L.; THORNE, R. M. Simulations of pitch angle
scattering of relativistic electrons with mlt-dependent diffusion coefficients.
Journal of Geophysical Research: Space Physics, v. 114, p. A03219, mar.
2009. 18, 19, 49, 68

SHPRITS, Y. Y.; DROZDOV, A. Y.; SPASOJEVIC, M.; KELLERMAN, A. C.;
USANOVA, M. E.; ENGEBRETSON, M. J.; AGAPITOV, O. V.;
ZHELAVSKAYA, I. S.; RAITA, T. J.; SPENCE, H. E.; BAKER, D. N.; ZHU, H.;

ASEEV, N. A. Wave-induced loss of ultra-relativistic electrons in the Van Allen radiation belts. **Nature Communications**, v. 7, n. 1, p. 12883, 2016. Disponível em: <https://doi.org/10.1038/ncomms12883>. 42

SHPRITS, Y. Y.; THORNE, R. M. Time dependent radial diffusion modeling of relativistic electrons with realistic loss rates. **Geophysical Research Letters**, v. 31, n. 8, 2004. Disponível em: <https://agupubs.onlinelibrary.wiley.com/doi/abs/10.1029/2004GL019591>. 19

SHPRITS, Y. Y.; THORNE, R. M.; FRIEDEL, R.; REEVES, G. D.; FENNELL, J.; BAKER, D. N.; KANEKAL, S. G. Outward radial diffusion driven by losses at magnetopause. **Journal of Geophysical Research: Space Physics**, v. 111, n. A11, 2006. Disponível em: <https://agupubs.onlinelibrary.wiley.com/doi/abs/10.1029/2006JA011657>. 19

SHUE, J.-H.; SONG, P.; RUSSELL, C. T.; STEINBERG, J. T.; CHAO, J. K.; ZASTENKER, G.; VAISBERG, O. L.; KOKUBUN, S.; SINGER, H. J.; DETMAN, T. R.; KAWANO, H. Magnetopause location under extreme solar wind conditions. **Journal of Geophysical Research: Space Physics**, v. 103, n. A8, p. 17691–17700, 1998. ISSN 2156-2202. Disponível em: <http://dx.doi.org/10.1029/98JA01103>. 15, 16

SIBECK, D. G.; MCENTIRE, R. W.; LUI, A. T. Y.; LOPEZ, R. E.; KRIMIGIS, S. M. Magnetic field drift shell splitting: cause of unusual dayside particle pitch angle distributions during storms and substorms. **Journal of Geophysical Research: Space Physics**, v. 92, n. A12, p. 13485–13497, 1987. ISSN 2156-2202. Disponível em: <http://dx.doi.org/10.1029/JA092iA12p13485>. 14, 43, 52, 53, 99, 103, 109

SILVA, L. A. D. **Omnidirectional electron flux, magnetopause position and Dst index during September 12 - 21, 2014.** 2015. Private comunication. 16

SOUZA, V. M.; MEDEIROS, C.; KOGA, D.; ALVES, L. R.; VIEIRA, L. E.; LAGO, A. D.; SILVA, L. A. D.; JAUER, P. R.; BAKER, D. N. Classification of magnetospheric particle distributions via neural networks. In: CAMPOREALE, E.; WING, S.; JOHNSON, J. R. (Ed.). **Machine learning techniques for space weather**. Elsevier, 2018. p. 329 – 353. ISBN 978-0-12-811788-0. Disponível em: <http://www.sciencedirect.com/science/article/pii/B9780128117880000135>. 93, 95, 96, 97, 98, 99, 107

SOUZA, V. M.; VIEIRA, L. E. A.; MEDEIROS, C.; SILVA, L. A. D.; ALVES, L. R.; KOGA, D.; SIBECK, D. G.; WALSH, B. M.; KANEKAL, S. G.; JAUER, P. R.; ROCKENBACH, M.; LAGO, A. D.; SILVEIRA, M. V. D.; MARCHEZI, J. P.; MENDES, O.; GONZALEZ, W. D.; BAKER, D. N. A neural network approach for identifying particle pitch angle distributions in Van Allen probes data. **Space Weather**, v. 14, n. 4, p. 275–284, 2016. Disponível em: <https://agupubs.onlinelibrary.wiley.com/doi/abs/10.1002/2015SW001349>. xiii, xv, 97

STIX, T. H.; SCOTT, F. R. The theory of plasma waves. **American Journal of Physics**, v. 31, n. 10, p. 816–816, Oct 1963. ISSN 1943-2909. Disponível em: <http://dx.doi.org/10.1119/1.1969127>. 34

SUESS, S. T.; TSURUTANI, B. T. **From the sun : auroras, magnetic storms, solar flares, cosmic rays**. In: . [S.l.]: [S.l.]: AGU, 1998. 13

SUMMERS, D.; NI, B.; MEREDITH, N. P. Timescales for radiation belt electron acceleration and loss due to resonant wave-particle interactions: 1. theory. **Journal of Geophysical Research: Space Physics**, v. 112, n. A4, 2007. ISSN 2156-2202. A04206. Disponível em: <http://dx.doi.org/10.1029/2006JA011801>. 41, 43, 49, 68

SUMMERS, D.; THORNE, R. M. Relativistic electron pitch-angle scattering by electromagnetic ion cyclotron waves during geomagnetic storms. **Journal of Geophysical Research: Space Physics**, v. 108, n. A4, 2003. ISSN 2156-2202. 1143. Disponível em: <http://dx.doi.org/10.1029/2002JA009489>. 41, 43, 67

SUMMERS, D.; THORNE, R. M.; XIAO, F. Relativistic theory of wave-particle resonant diffusion with application to electron acceleration in the magnetosphere. **Journal of Geophysical Research: Space Physics**, v. 103, n. A9, p. 20487–20500, 1998. Disponível em: <https://agupubs.onlinelibrary.wiley.com/doi/abs/10.1029/98JA01740>. 19

THORNE, R. M. Radiation belt dynamics: the importance of wave-particle interactions. **Geophysical Research Letters**, v. 37, n. 22, 2010. Disponível em: <https://agupubs.onlinelibrary.wiley.com/doi/abs/10.1029/2010GL044990>. 18, 19, 20, 35, 36, 38, 41

THORNE, R. M.; HORNE, R. B. Modulation of electromagnetic ion cyclotron instability due to interaction with ring current o+ during magnetic storms. **Journal of Geophysical Research: Space Physics**, v. 102, n. A7, p. 14155–14163, 1997. Disponível em: <https://agupubs.onlinelibrary.wiley.com/doi/abs/10.1029/96JA04019>. 41

THORNE, R. M.; KENNEL, C. F. Relativistic electron precipitation during magnetic storm main phase. **Journal of Geophysical Research**, v. 76, n. 19, p. 4446–4453, jul 1971. Disponível em: <https://doi.org/10.1029/ja076i019p04446>. 19, 41

TÓTH, G.; HOLST, B. van der; SOKOLOV, I. V.; ZEEUW, D. L. D.; GOMBOSI, T. I.; FANG, F.; MANCHESTER, W. B.; MENG, X.; NAJIB, D.; POWELL, K. G.; STOUT, Q. F.; GLOCER, A.; MA, Y.-J.; OPHER, M. Adaptive numerical algorithms in space weather modeling. **Journal of Computational Physics**, v. 231, n. 3, p. 870 – 903, 2012. ISSN 0021-9991. Disponível em: <http://www.sciencedirect.com/science/article/pii/S002199911100088X>. 51

TSURUTANI, B. T.; LAKHINA, G. S. Some basic concepts of wave-particle interactions in collisionless plasmas. **Reviews of Geophysics**, v. 35, n. 4, p. 491–501, 1997. Disponível em: <https://agupubs.onlinelibrary.wiley.com/doi/abs/10.1029/97RG02200>. 21, 22, 23, 25, 26, 27, 28, 29, 30, 31, 33, 35

TSURUTANI, B. T.; SMITH, E. J. Postmidnight chorus: a substorm phenomenon. **Journal of Geophysical Research**, v. 79, n. 1, p. 118–127, 1974. Disponível em: <https://agupubs.onlinelibrary.wiley.com/doi/abs/10.1029/JA079i001p00118>. 35

TSYGANENKO, N. A.; SITNOV, M. I. Modeling the dynamics of the inner magnetosphere during strong geomagnetic storms. **Journal of Geophysical Research: Space Physics**, v. 110, n. A3, 2005. ISSN 2156-2202. A03208. Disponível em: <http://dx.doi.org/10.1029/2004JA010798>. 62, 71

UKHORSKIY, A. Y.; ANDERSON, B. J.; TAKAHASHI, K.; TSYGANENKO, N. A. Impact of ulf oscillations in solar wind dynamic pressure on the outer radiation belt electrons. **Geophysical Research Letters**, v. 33, n. 6, 2006. Disponível em: <https://agupubs.onlinelibrary.wiley.com/doi/abs/10.1029/2005GL024380>. 38

USANOVA, M. E.; DARROUZET, F.; MANN, I. R.; BORTNIK, J. Statistical analysis of emic waves in plasmaspheric plumes from cluster observations. **Journal of Geophysical Research: Space Physics**, v. 118, n. 8, p. 4946–4951, 2013. Disponível em: <https://agupubs.onlinelibrary.wiley.com/doi/abs/10.1002/jgra.50464>. 41, 105, 106

USANOVA, M. E.; DROZDOV, A.; ORLOVA, K.; MANN, I. R.; SHPRITS, Y.; ROBERTSON, M. T.; TURNER, D. L.; MILLING, D. K.; KALE, A.; BAKER, D. N.; THALLER, S. A.; REEVES, G. D.; SPENCE, H. E.; KLETZING, C.; WYGANT, J. Effect of emic waves on relativistic and ultrarelativistic electron populations: ground-based and van allen probes observations. **Geophysical Research Letters**, v. 41, n. 5, p. 1375–1381, 2014. ISSN 1944-8007. 2013GL059024. Disponível em: <http://dx.doi.org/10.1002/2013GL059024>. 19, 43, 49, 68, 96, 105, 106

USANOVA, M. E.; MANN, I. R.; BORTNIK, J.; SHAO, L.; ANGELOPOULOS, V. Themis observations of electromagnetic ion cyclotron wave occurrence: dependence on ae, symh, and solar wind dynamic pressure. **Journal of Geophysical Research: Space Physics**, v. 117, n. A10, 2012. Disponível em: <https://agupubs.onlinelibrary.wiley.com/doi/abs/10.1029/2012JA018049>. 41

VIOLA, P.; JONES, M. J. Robust real-time face detection. **International Journal of Computer Vision**, v. 57, n. 2, p. 137–154, May 2004. ISSN 0920-5691. Disponível em: <http://dx.doi.org/10.1023/B:VISI.0000013087.49260.fb>. 77

WANG, D.; YUAN, Z.; YU, X.; DENG, X.; ZHOU, M.; HUANG, S.; LI, H.; WANG, Z.; QIAO, Z.; KLETZING, C. A.; WYGANT, J. R. Statistical characteristics of emic waves: Van Allen probe observations. **Journal of Geophysical Research: Space Physics**, v. 120, p. 4400–4408, jun. 2015. 41, 63

WEIMER, D. R. An improved model of ionospheric electric potentials including substorm perturbations and application to the geospace environment modeling november 24, 1996, event. **Journal of Geophysical Research: Space Physics**, v. 106, n. A1, p. 407–416, 2001. ISSN 2156-2202. Disponível em: <http://dx.doi.org/10.1029/2000JA000604>. 62

WEST JUNIOR, H. I.; BUCK, R. M.; WALTON, J. R. Electron pitch angle distributions throughout the magnetosphere as observed on ogo 5. **Journal of**

Geophysical Research (1896-1977), v. 78, n. 7, p. 1064–1081, 1973. Disponível em: <https://agupubs.onlinelibrary.wiley.com/doi/abs/10.1029/JA078i007p01064>. 43, 52, 109

XIAO, F.; YANG, C.; SU, Z.; ZHOU, Q.; HE, Z.; HE, Y.; BAKER, D. N.; SPENCE, H. E.; FUNSTEN, H. O.; BLAKE, J. B. Wave-driven butterfly distribution of van allen belt relativistic electrons. **Nature Communications**, v. 6, p. 8590, oct 2015. Disponível em: <https://doi.org/10.1038/ncomms9590>. 42

ZEEUW, D. L. de; SAZYKIN, S.; WOLF, R. A.; GOMBOSI, T. I.; RIDLEY, A. J.; TÓTH, G. Coupling of a global mhd code and an inner magnetospheric model: initial results. **Journal of Geophysical Research: Space Physics**, v. 109, p. A12219, dez. 2004. 51

ZHANG, J.; HALFORD, A. J.; SAIKIN, A. A.; HUANG, C.-L.; SPENCE, H. E.; LARSEN, B. A.; REEVES, G. D.; MILLAN, R. M.; SMITH, C. W.; TORBERT, R. B.; KURTH, W. S.; KLETZING, C. A.; BLAKE, J. B.; FENNEL, J. F.; BAKER, D. N. Emic waves and associated relativistic electron precipitation on 25-26 january 2013. **Journal of Geophysical Research: Space Physics**, v. 121, n. 11, p. 11,086–11,100, 2016. ISSN 2169-9402. 2016JA022918. Disponível em: <http://dx.doi.org/10.1002/2016JA022918>. 49, 68

ZHANG, X.-J.; LI, W.; MA, Q.; THORNE, R. M.; ANGELOPOULOS, V.; BORTNIK, J.; CHEN, L.; KLETZING, C. A.; KURTH, W. S.; HOSPODARSKY, G. B.; BAKER, D. N.; REEVES, G. D.; SPENCE, H. E.; BLAKE, J. B.; FENNELL, J. F. Direct evidence for emic wave scattering of relativistic electrons in space. **Journal of Geophysical Research: Space Physics**, v. 121, n. 7, p. 6620–6631, 2016. ISSN 2169-9402. 2016JA022521. Disponível em: <http://dx.doi.org/10.1002/2016JA022521>. 65

APPENDIX A - 21 CASE STUDIES OF PERSISTENT UNUSUAL ELECTRON BUTTERFLY PITCH ANGLE DISTRIBUTION SHAPE

Figure A.1 - Event 01 - September 26, 2014
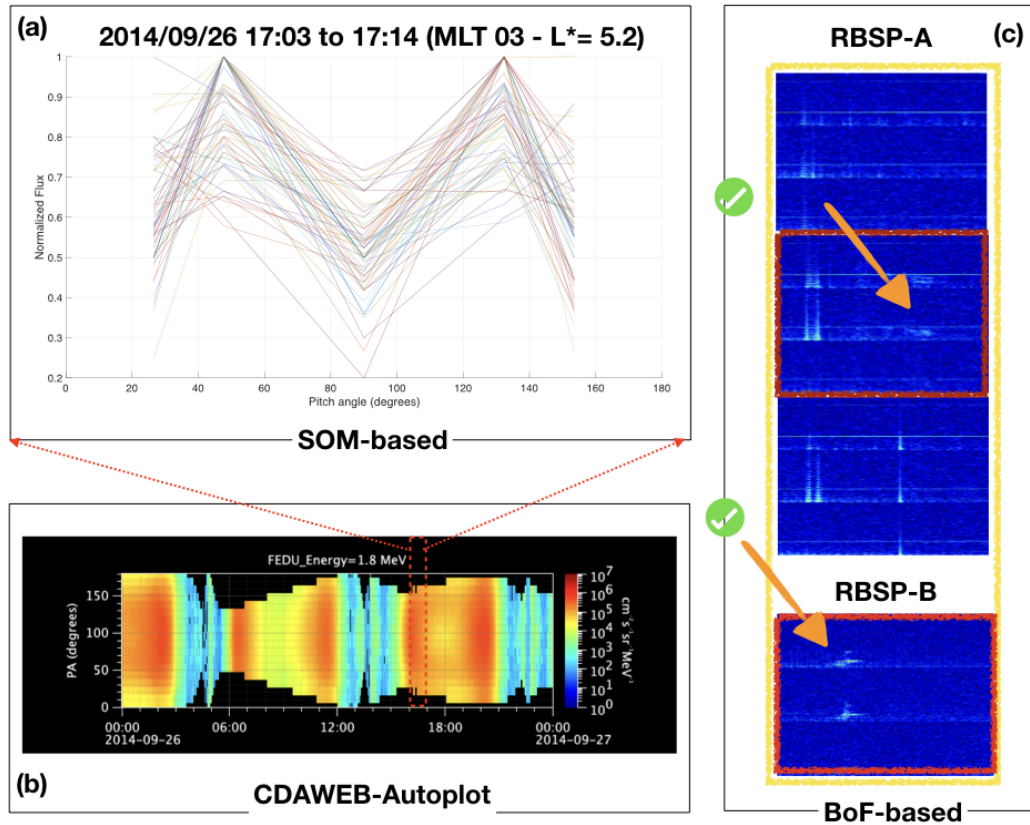
(a) SOM-based classification shown the persistent unusual butterfly PAD shape on September 26, 2014 after 17:00 UT. Van Allen Probe A was in MLT 03 and L-star $\sim$ 5.2.(b) The relativistic electron at 1.8 MeV channel shown the pitch angle distribution during one day.(c) Bof technique classified 4 (3 by RBSP-A and 1 by RBSP-B) images as EMIC classes. At least two of them (red box) presented clear EMIC-like wave signature (orange arrow).

SOURCE: Author production.

Figure A.2 - Event 02 - October 12, 2014
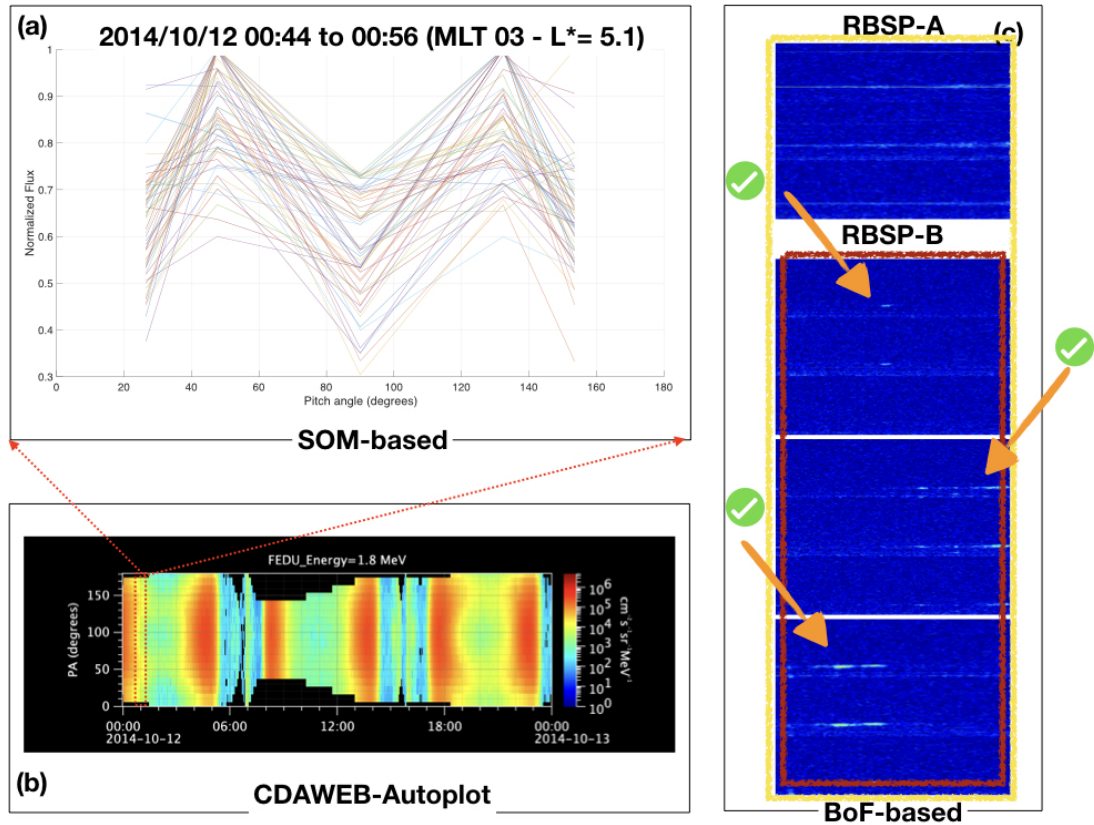
(a) SOM-based classification shown the persistent unusual butterfly PAD shape on October 12, 2014 after 00:44 UT. Van Allen Probe A was in MLT 03 and L-star ~ 5.1. (b) The relativistic electron at 1.8 MeV channel shown the pitch angle distribution during one day. (c) BoF technique classified 4 (1 by RBSP-A and 3 by RBSP-B) images as pertaining to the *EMIC* class. Four images (yellow box) shown considerable regions in which the contrast with the background color suggested some wave activities. Three of them (red box) presented clear EMIC-like wave signatures (orange arrows).

SOURCE: Author production.

Figure A.3 - Event 03 - October 21, 2014
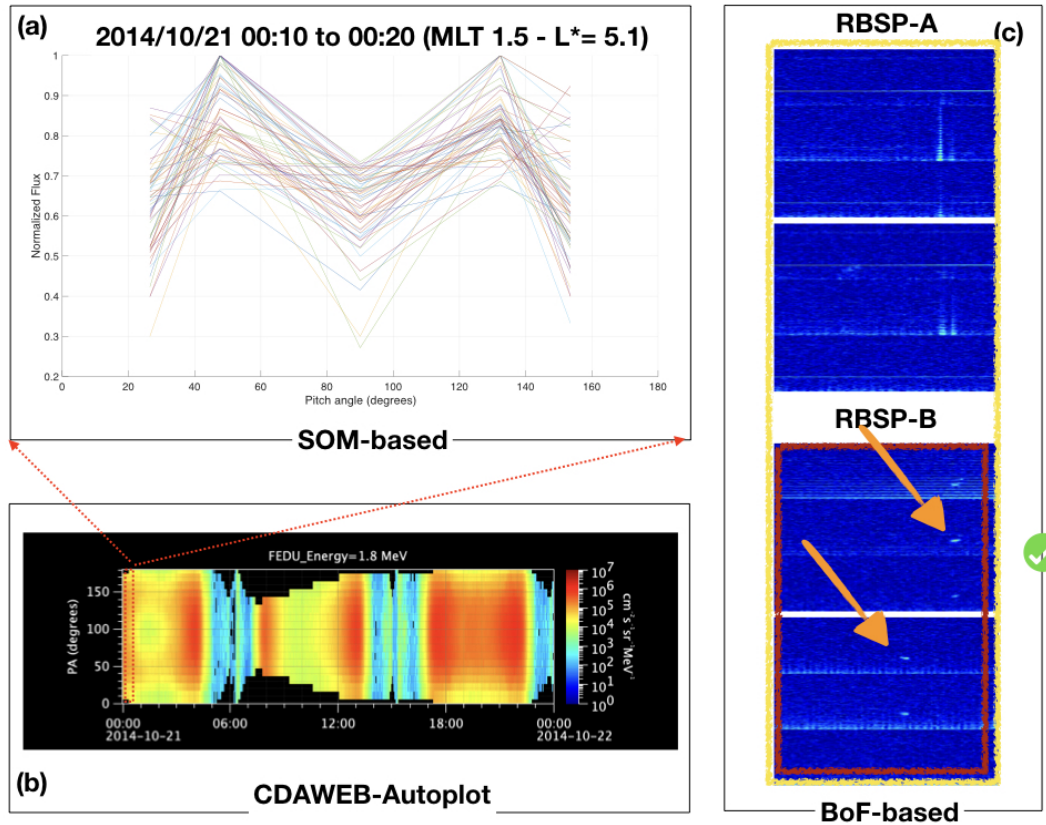
(a) SOM-based classification shown the persistent unusual butterfly PAD shape on October 21, 2014 after 00:44 UT. Van Allen Probe A was between MLT 01 and 02 and L-star ~ 5.1.(b) The relativistic electron at 1.8 MeV channel shown the pitch angle distribution during one day.(c) BoF technique classified 4 (2 by RBSP-A and 2 by RBSP-B) images as pertaining to the *EMIC* class. Four images (yellow box) shown considerable regions in which the contrast with the background color suggested some wave activities. Two of them (red box) presented clear EMIC-like wave signature (orange arrow).

SOURCE: Author production.

Figure A.4 - Event 04 - November 01, 2014
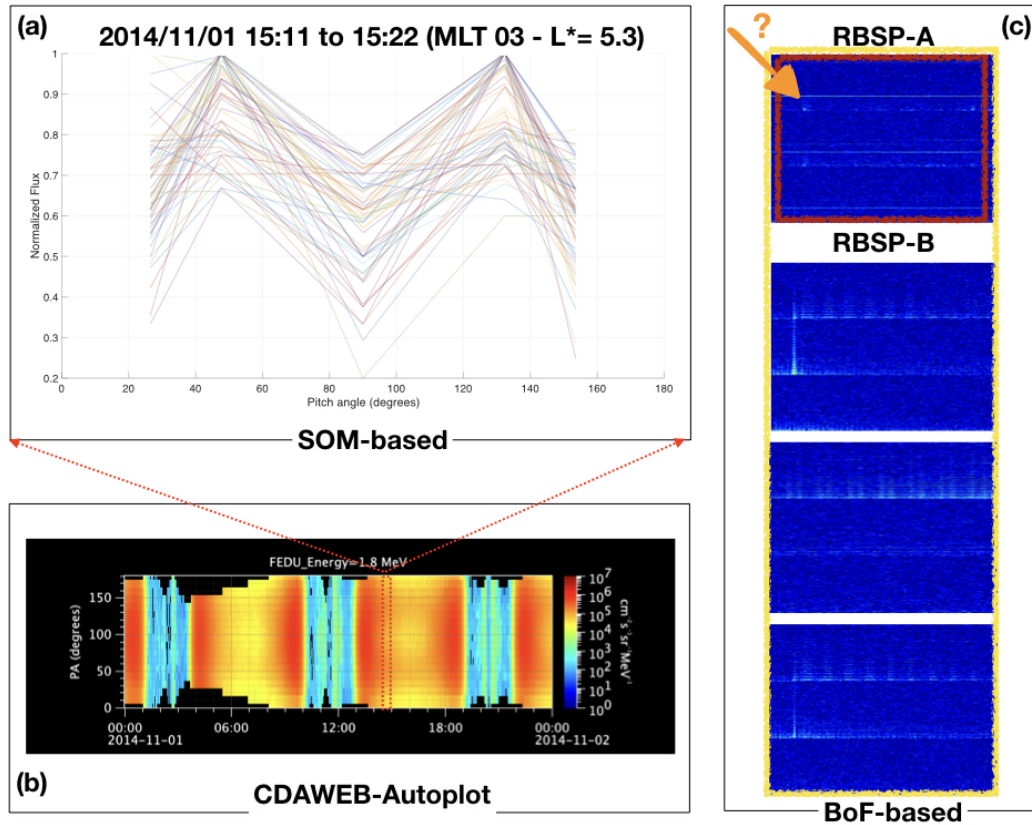
(a) SOM-based classification shown the persistent unusual butterfly PAD shape on November 01, 2014 after 15:11 UT. Van Allen Probe A was between MLT 03 and L-star $\sim$ 5.3.(b) The relativistic electron at 1.8 MeV channel shown the pitch angle distribution during one day.(c) Bof technique classified 4 (1 by RBSP-A and 3 by RBSP-B) images pertaining to the *EMIC* class. Four images (yellow box) shown considerable regions in which the contrast with the background color suggesting some wave activity. Only one of them (red box) presented, perhaps, EMIC-like wave signatures (orange arrow).

SOURCE: Author production.

Figure A.5 - Event 05 - November 19, 2014
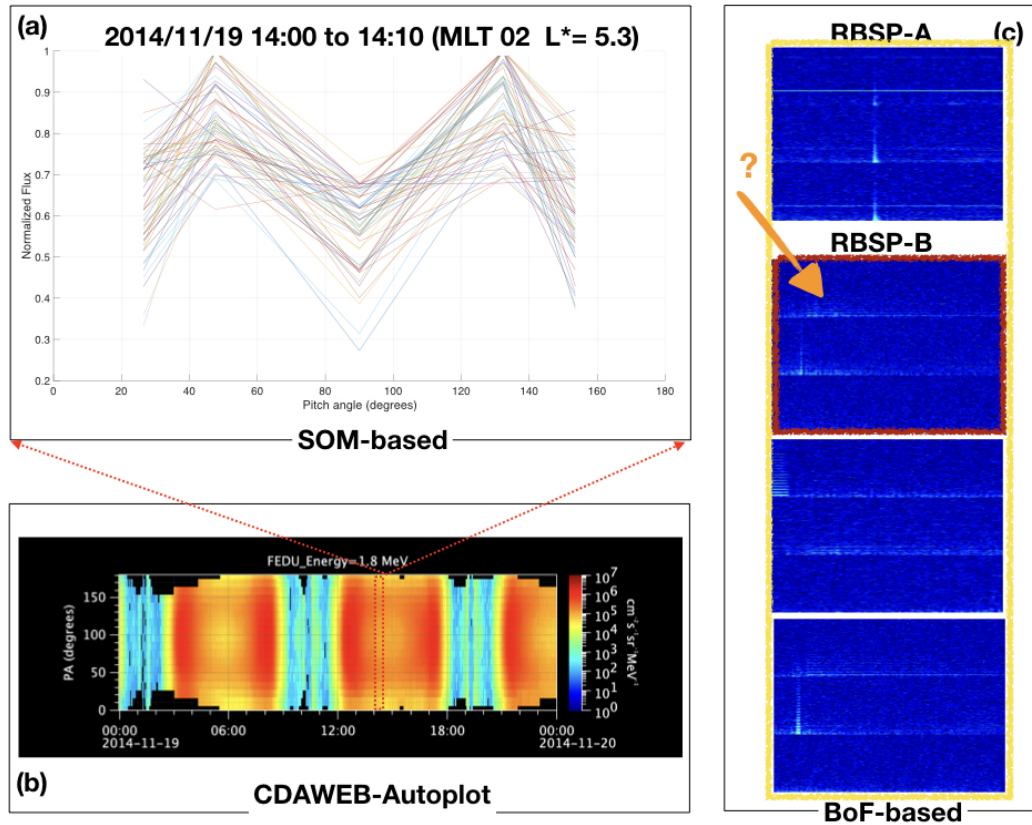
(a) SOM-based classification shown the persistent unusual butterfly PAD shape on November 19, 2014 after 14:00 UT. Van Allen Probe A was in MLT 02 and L-star ~ 5.3.(b) The relativistic electron at 1.8 MeV channel shown the pitch angle distribution during one day.(c) BoF technique classified 4 (1 by RBSP-A and 3 by RBSP-B) images as pertaining to the *EMIC* class. Four images (yellow box) show considerable regions in which the contrast with the background color suggested some wave activities. Only one of them (red box) presented, perhaps, EMIC-like wave signature (orange arrow).

SOURCE: Author production.

Figure A.6 - Event 06 - December 08, 2014
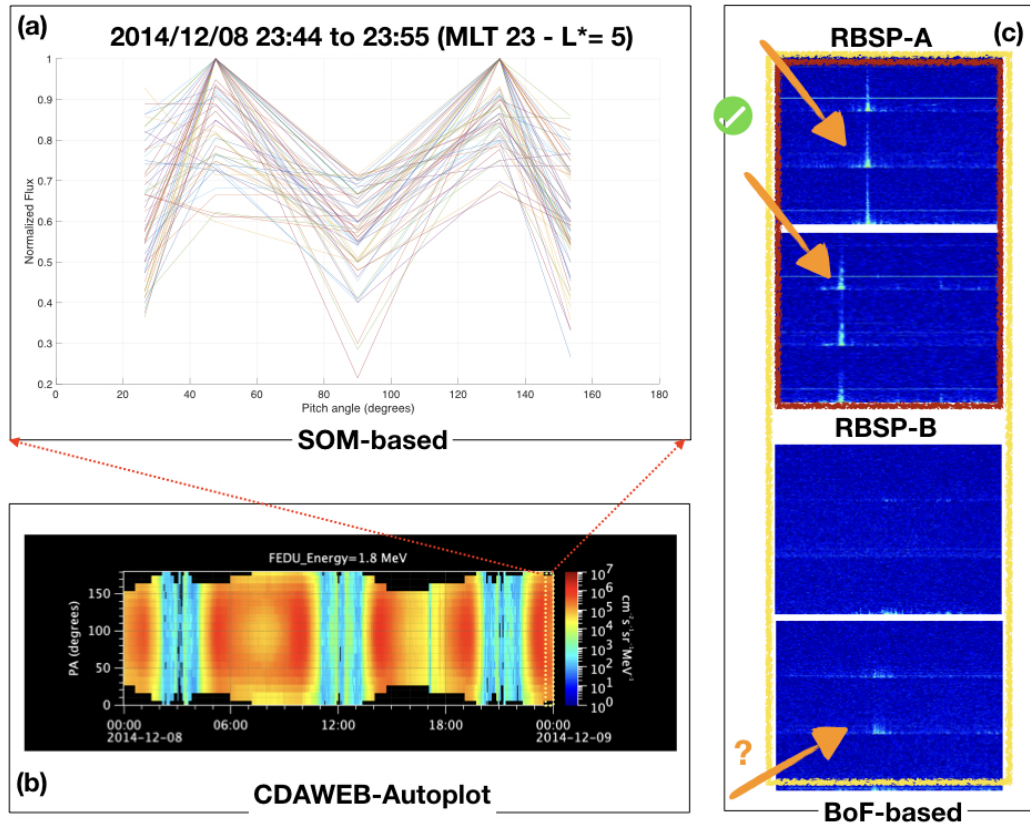
(a) SOM-based classification shown the persistent unusual butterfly PAD shape on December 08, 2014 after 23:44 UT. Van Allen Probe A was in MLT 23 and L-star $\sim$ 5.(b) The relativistic electron at 1.8 MeV channel shown the pitch angle distribution during one day. (c) Bof technique classified 4 (2 by RBSP-A and 2 by RBSP-B) images as EMIC classes. Four images (yellow box) shown considerable regions in which the contrast with the background color suggested some wave activities. Three of them (red box) presented EMIC-like wave signature (orange arrow).

SOURCE: Author production.

Figure A.7 - Event 07 - December 10, 2014
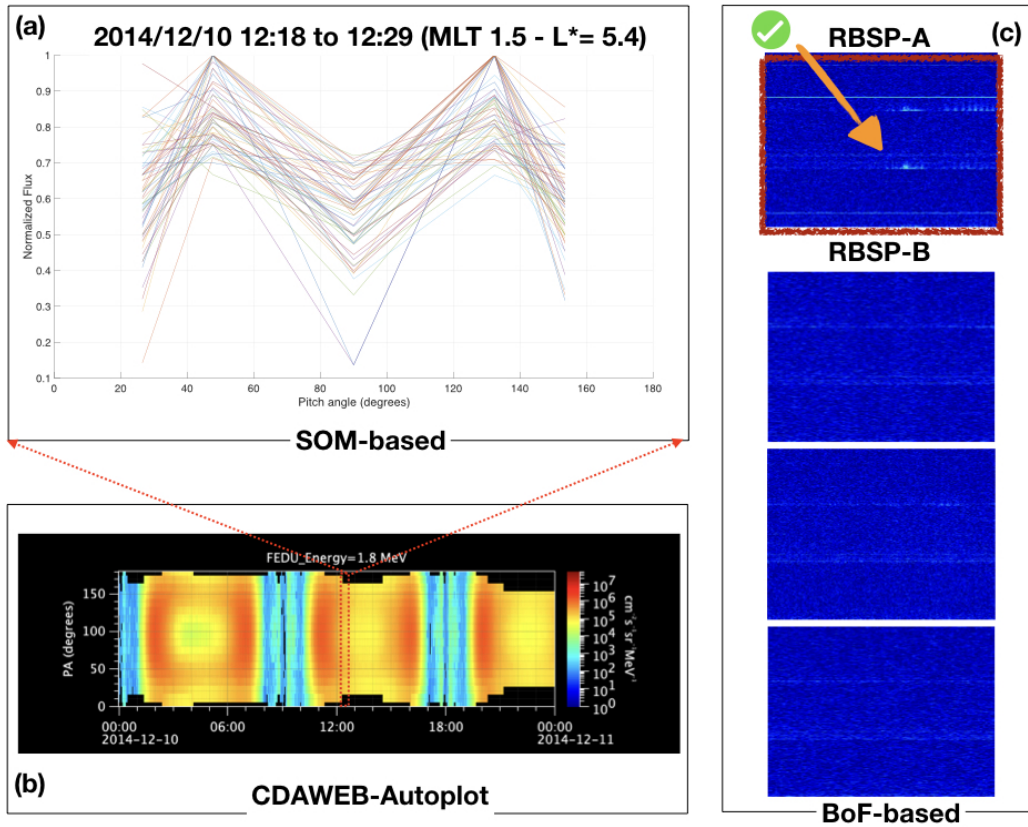
(a) SOM-based classification shown the persistent unusual butterfly PAD shape on December 10, 2014 after 12:18 UT. Van Allen Probe A was between MLT 01 and 02 and L-star ~ 5.4.(b) The relativistic electron at 1.8 MeV channel shown the pitch angle distribution during one day. (c) Bof technique classified 4 (1 by RBSP-A and 3 by RBSP-B) images as EMIC classes. One of them (red box) presented EMIC-like wave signature (orange arrow).

SOURCE: Author production.

Figure A.8 - Event 08 - December 26, 2014
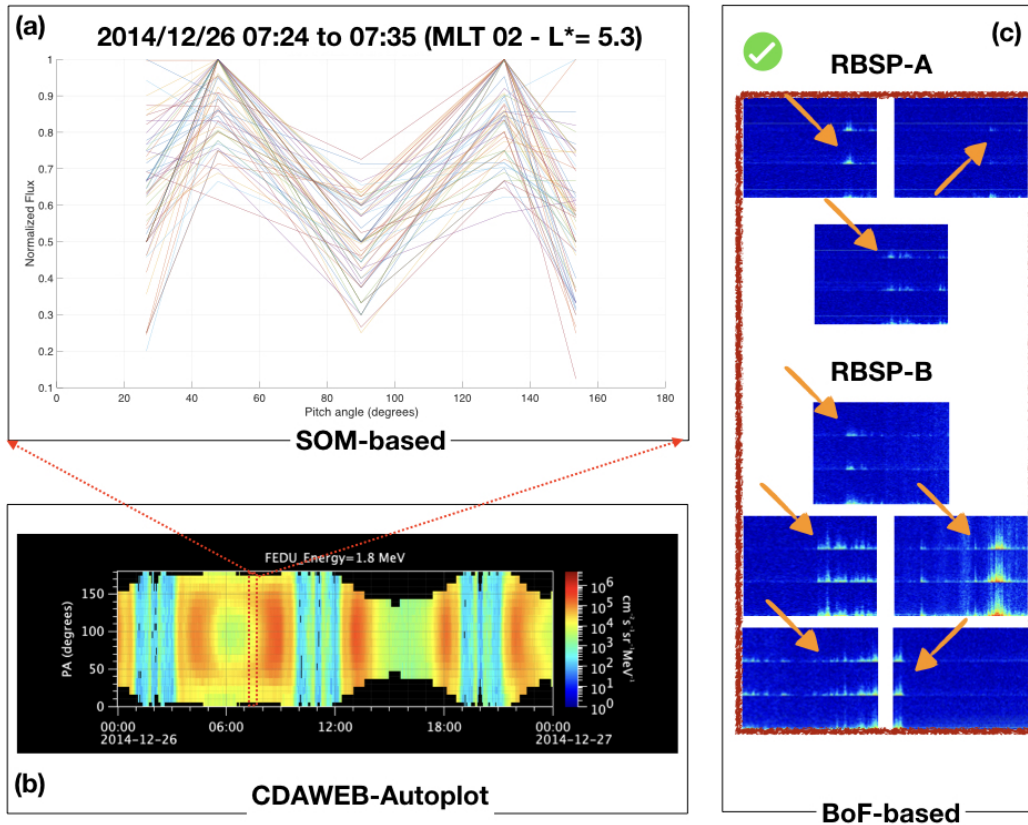
(a) SOM-based classification shown the persistent unusual butterfly PAD shape on December 26, 2014 after 07:24 UT. Van Allen Probe A was in MLT 02 and L-star ~ 5.3.(b) The relativistic electron at 1.8 MeV channel shown the pitch angle distribution during one day. (c) Bof technique classified 8 (3 by RBSP-A and 5 by RBSP-B) images as EMIC classes. All images shown considerable regions in which the contrast with the background color suggested EMIC-like wave signature (orange arrow).

SOURCE: Author production.

Figure A.9 - Event 09 - January 05, 2015
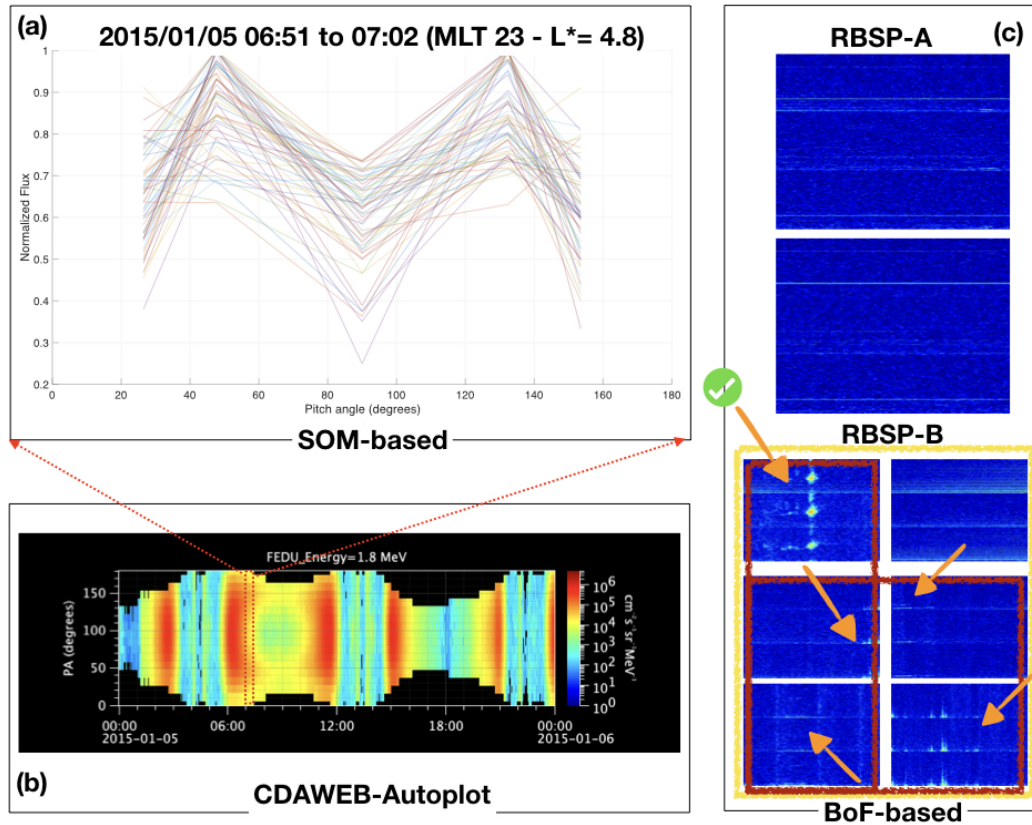
(a) SOM-based classification shown the persistent unusual butterfly PAD shape on January 05, 2015 after 06:51 UT. Van Allen Probe A was in MLT 23 and L-star ~ 4.8.(b) The relativistic electron at 1.8 MeV channel shown the pitch angle distribution during one day.(c) Bof technique classified 8 (2 by RBSP-A and 6 by RBSP-B) images as EMIC classes. Six images (yellow box) shown considerable regions in which the contrast with the background color suggested some wave activities. Five of them (red box) presented EMIC-like wave signature (orange arrow).

SOURCE: Author production.

Figure A.10 - Event 10 - January 07, 2015
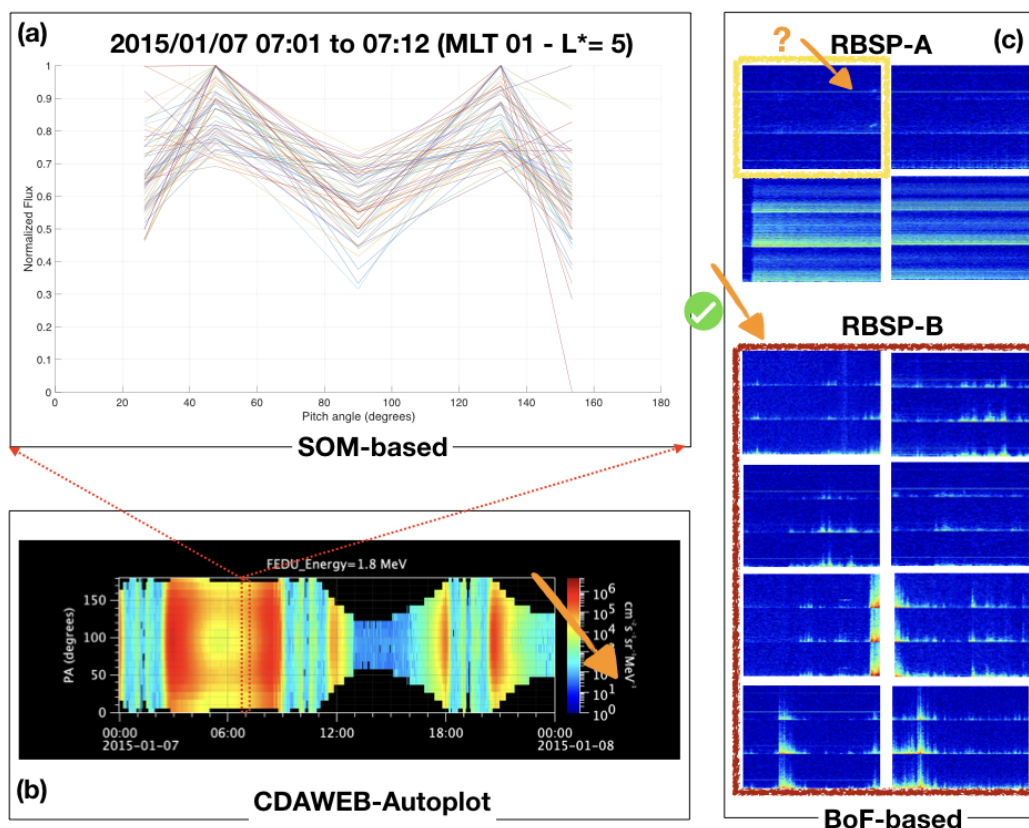
(a) SOM-based classification shown the persistent unusual butterfly PAD shape on January 07, 2015 after 07:01 UT. Van Allen Probe A was in MLT 01 and L-star $\sim$ 5.(b) The relativistic electron at 1.8 MeV channel shown the pitch angle distribution during one day.(c) Bof technique classified 12 (4 by RBSP-A and 8 by RBSP-B) images as EMIC classes. One image (yellow box) shown considerable regions in which the contrast with the background color suggested some wave activities. Two images from RBSP-A shown artifacts noise. Eight images (red box) from RBSP-B presented EMIC-like wave signature (orange arrow).

SOURCE: Author production.

Figure A.11 - Event 11 - February 03, 2015
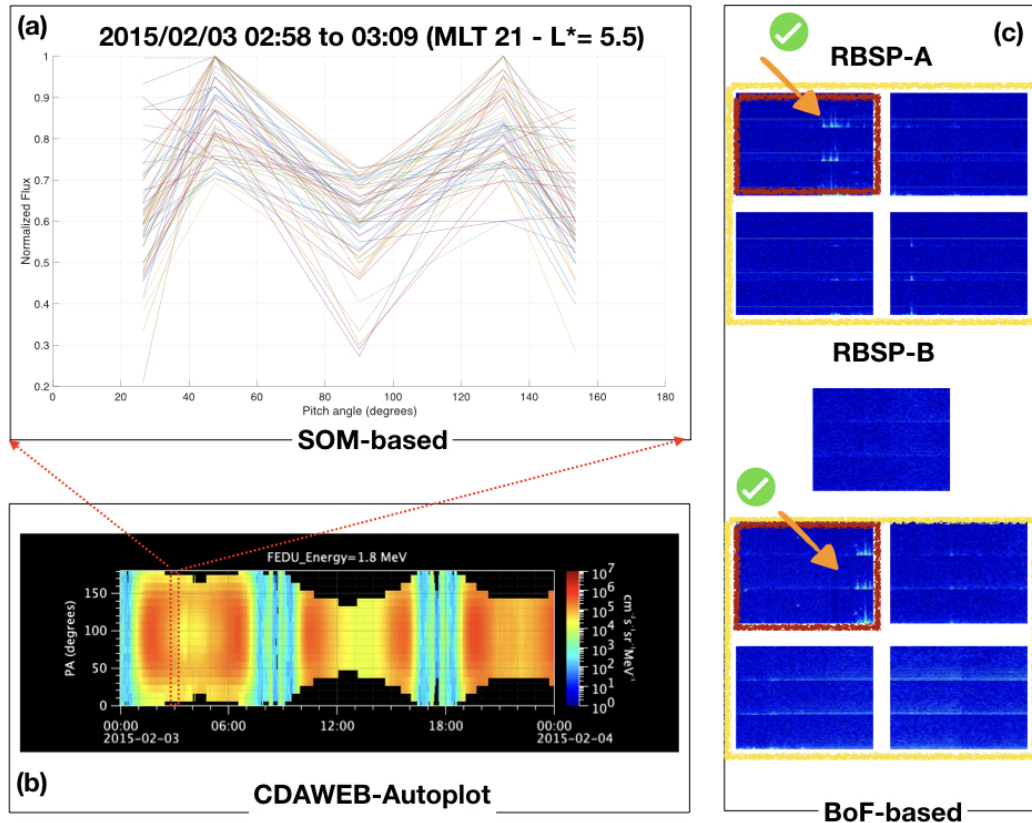
(a) SOM-based classification shown the persistent unusual butterfly PAD shape on February 03, 2015 after 2:58 UT. Van Allen Probe A was between MLT 21 and L-star ~ 5.5.(b)The relativistic electron at 1.8 MeV channel shown the pitch angle distribution during one day.(c) Bof technique classified 9 (4 by RBSP-A and 5 by RBSP-B) images as EMIC classes. Eight images (yellow box) shown considerable regions in which the contrast with the background color suggested some wave activities. Two of them (red box) presented EMIC-like wave signature(orange arrow).

SOURCE: Author production.

Figure A.12 - Event 12 - February 22, 2015
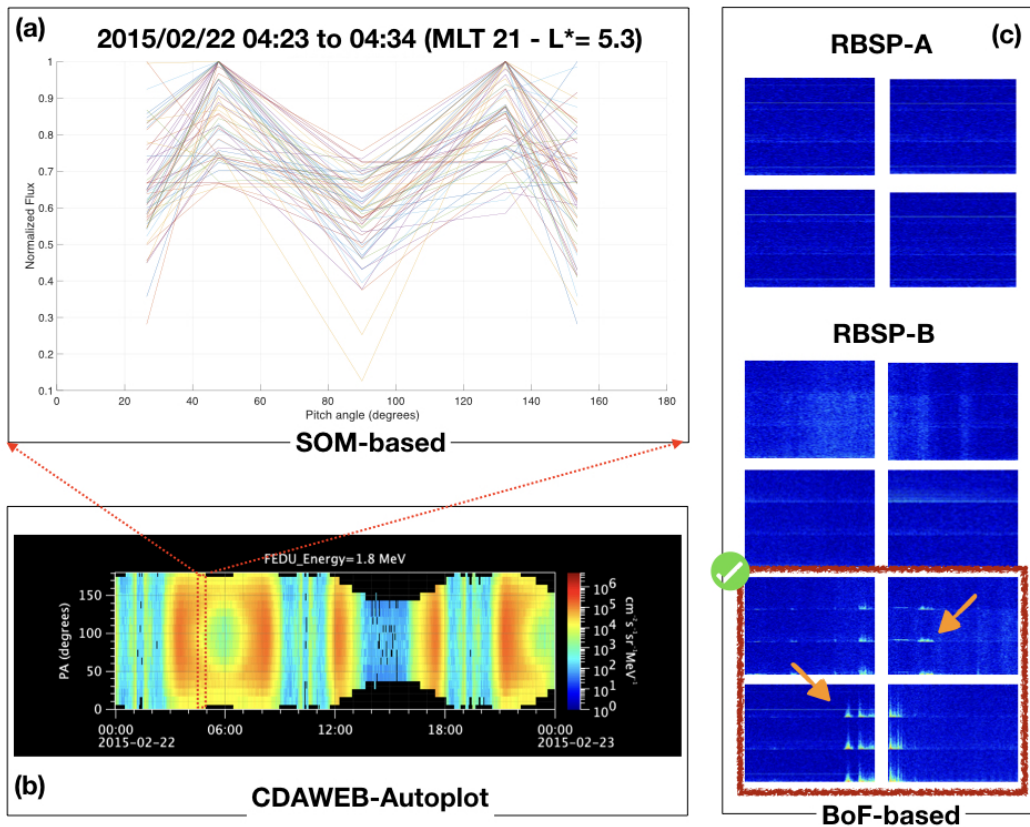
(a) SOM-based classification shown the persistent unusual butterfly PAD shape on February 22, 2015 after 4:23 UT. Van Allen Probe A was in MLT 21 and L-star $\sim$ 5.3.(b) The relativistic electron at 1.8 MeV channel shown the pitch angle distribution during one day.(c) Bof technique classified 12 (4 by RBSP-A and 8 by RBSP-B) images as EMIC classes. Four of them (red box) presented EMIC-like wave signature (orange arrow).

SOURCE: Author production.

Figure A.13 - Event 13 - March 03, 2015
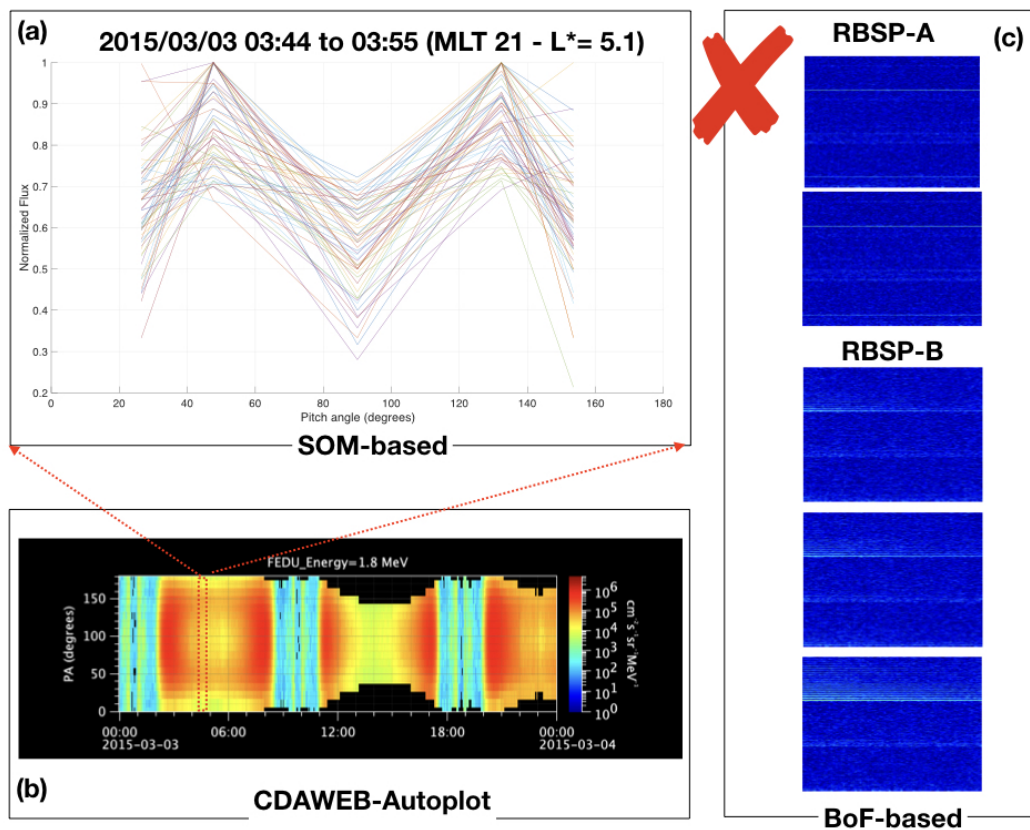
(a) SOM-based classification shown the persistent unusual butterfly PAD shape on March 03, 2015 after 03:44 UT. Van Allen Probe A was between MLT 21 and L-star $\sim$ 5.1.(b) The relativistic electron at 1.8 MeV channel shown the pitch angle distribution during one day.(c) Bof technique classified 5 (2 by RBSP-A and 3 by RBSP-B) images as EMIC classes. None of them presented EMIC-like wave signature.

SOURCE: Author production.

Figure A.14 - Event 14 - March 07, 2015
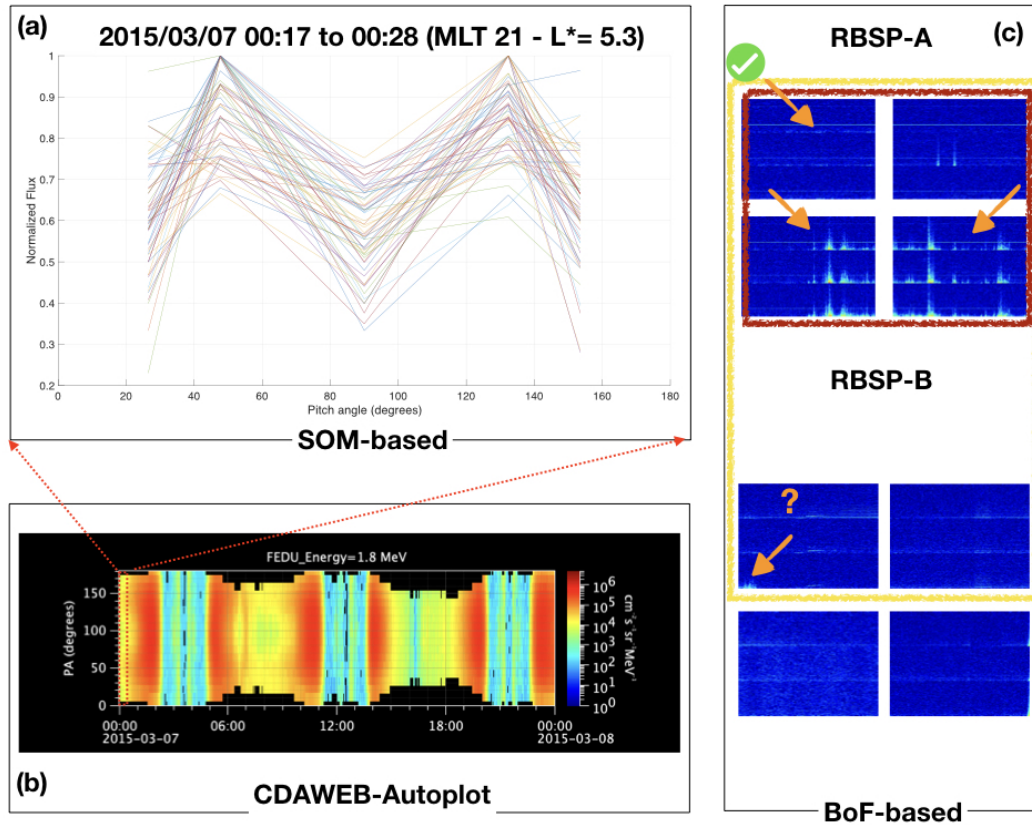
(a) SOM-based classification shown the persistent unusual butterfly PAD shape on March 07, 2015 after 00:17 UT. Van Allen Probe A was in MLT 21 and L-star $\sim$ 5.3.(b) The relativistic electron at 1.8 MeV channel shown the pitch angle distribution during one day.(c) Bof technique classified 8 (4 by RBSP-A and 4 by RBSP-B) images as EMIC classes. Six images (yellow box) shown considerable regions in which the contrast with the background color suggested some wave activities. Four of them (red box) presented EMIC-like wave signature (orange arrow).

SOURCE: Author production.

Figure A.15 - Event 15 - March 14, 2015
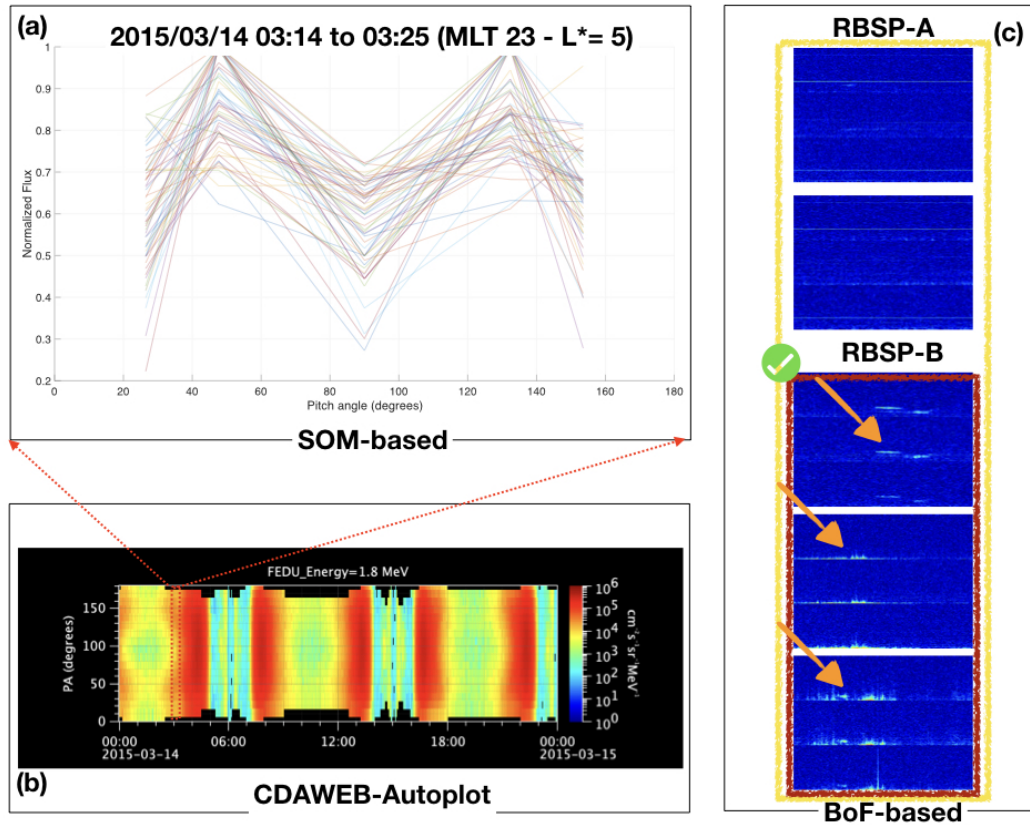
(a) SOM-based classification shown the persistent unusual butterfly PAD shape on March 14, 2015 after 3:14 UT. Van Allen Probe A was in MLT 23 and L-star $\sim$ 5.(b) The relativistic electron at 1.8 MeV channel shown the pitch angle distribution during one day.(c) Bof technique classified 5 (2 by RBSP-A and 3 by RBSP-B) images as EMIC classes. Five images (yellow box) shown considerable regions in which the contrast with the background color suggested some wave activities. Three of them (red box) presented EMIC-like wave signature (orange arrow).

SOURCE: Author production.

Figure A.16 - Event 16 - March 18, 2015
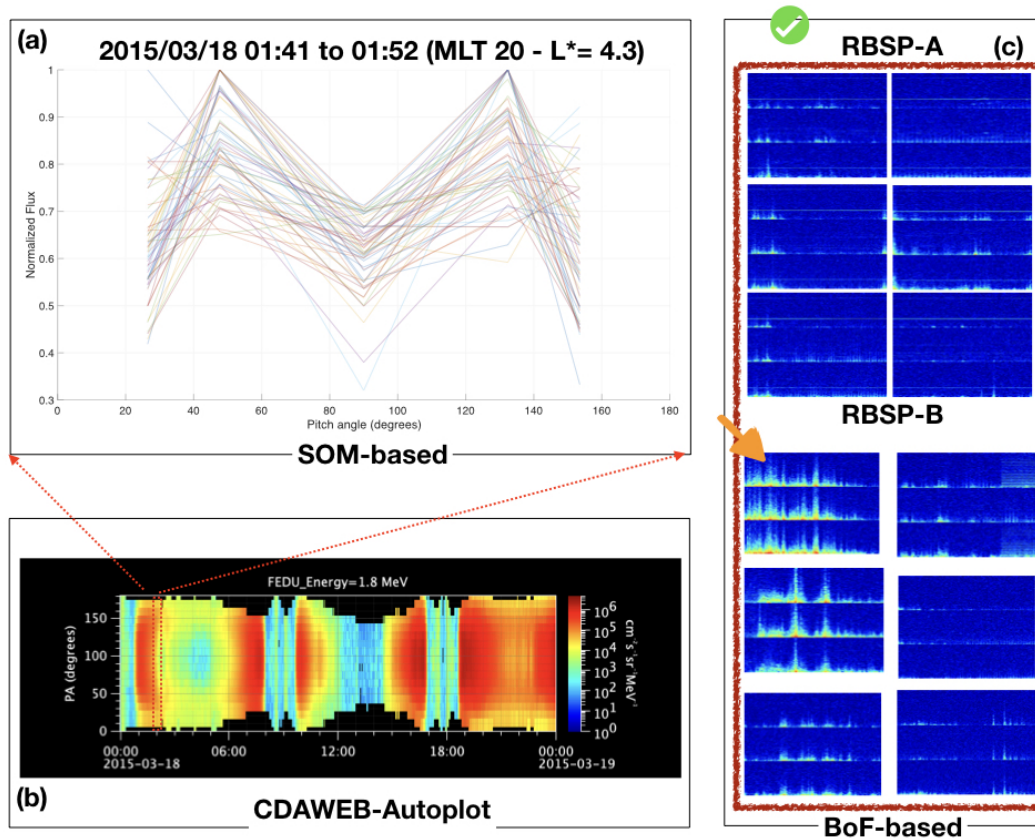
(a) SOM-based classification shown the persistent unusual butterfly PAD shape on March 18, 2015 after 01:41 UT. Van Allen Probe A was in MLT 20 and L-star $\sim$ 4.3.(b) The relativistic electron at 1.8 MeV channel shown the pitch angle distribution during one day.(c) Bof technique classified 12 (6 by RBSP-A and 6 by RBSP-B) images as EMIC classes. All images (red box) presented EMIC-like wave signature (orange arrow).

SOURCE: Author production.

Figure A.17 - Event 17 - April 13, 2015
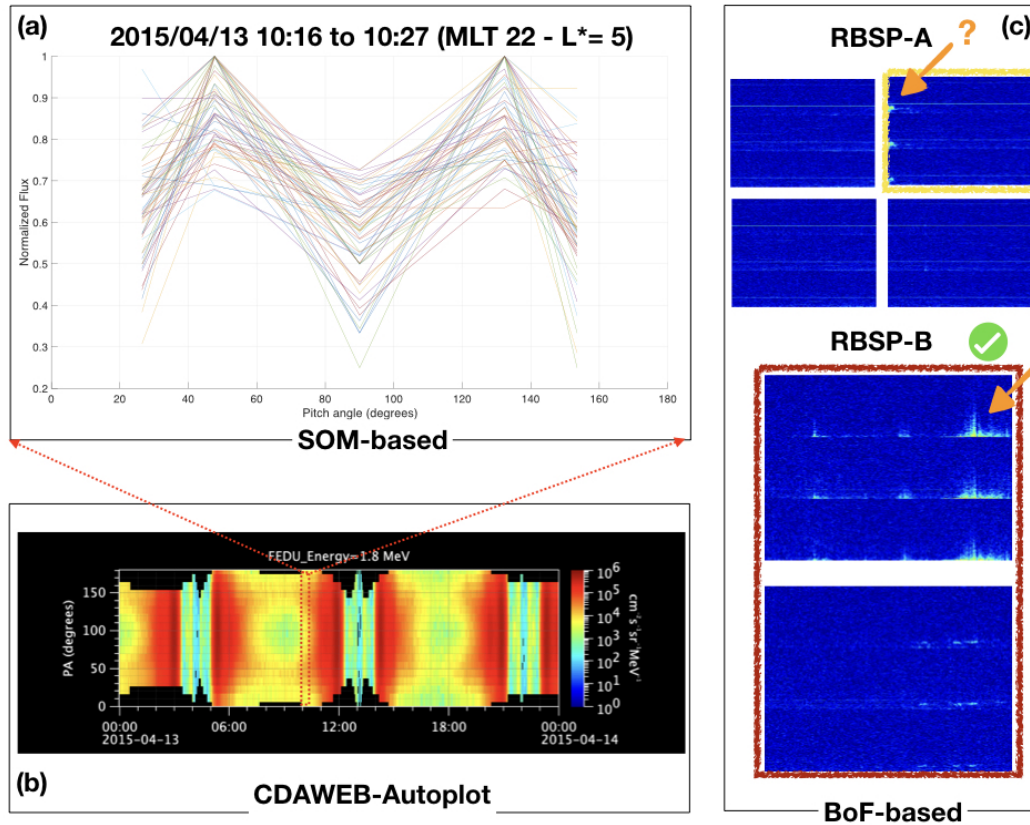
(a) SOM-based classification shown the persistent unusual butterfly PAD shape on April 13, 2015 after 10:16 UT. Van Allen Probe A was in MLT 22 and L-star $\sim$ 5.(b) The relativistic electron at 1.8 MeV channel shown the pitch angle distribution during one day.(c) Bof technique classified 6 (4 by RBSP-A and 2 by RBSP-B) images as EMIC classes. One image (yellow box) shown one region in which the contrast with the background color suggested some wave activities. Two images (red box) presented EMIC-like wave signature (orange arrow).

SOURCE: Author production.

Figure A.18 - Event 18 - April 20, 2015
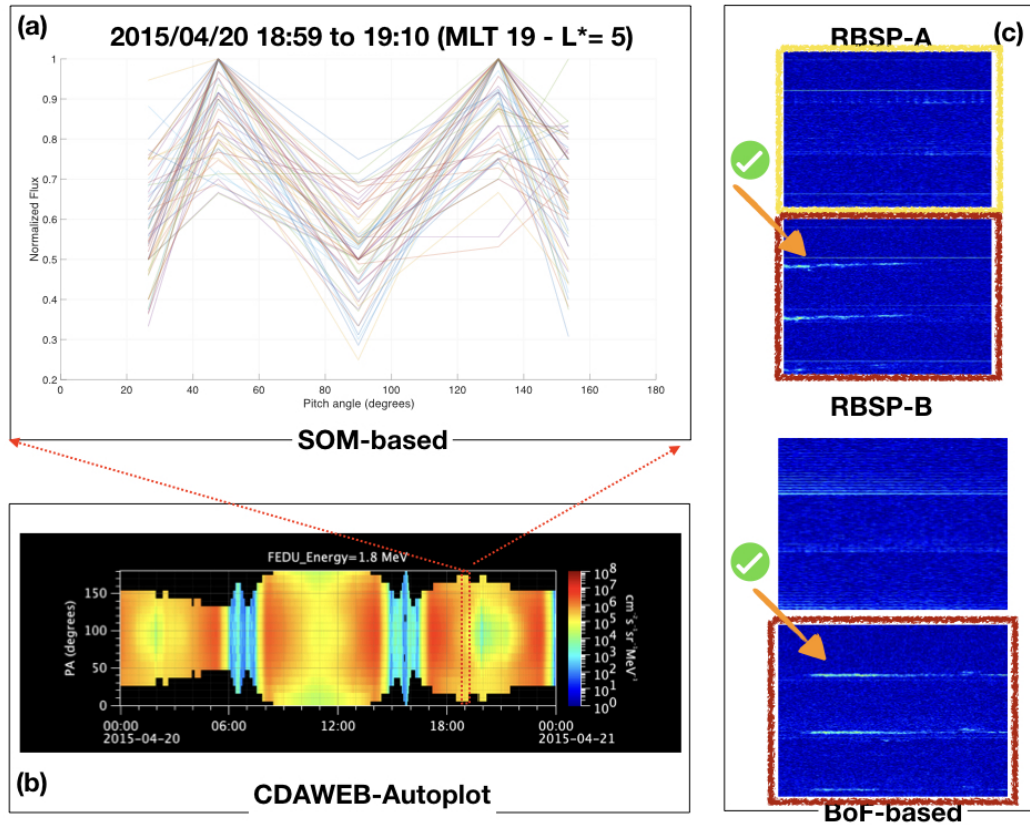
(a) SOM-based classification shown the persistent unusual butterfly PAD shape on April 20, 2015 after 18:59 UT. Van Allen Probe A was in MLT 19 and L-star ~ 5.(b) The relativistic electron at 1.8 MeV channel shown the pitch angle distribution during one day.(c) Bof technique classified 4 (2 by RBSP-A and 2 by RBSP-B) images as EMIC classes. One image (yellow box) shown one region in which the contrast with the background color suggested some wave activities. Two images (red box) presented EMIC-like wave signature (orange arrow).

SOURCE: Author production.

Figure A.19 - Event 19 - May 19, 2015
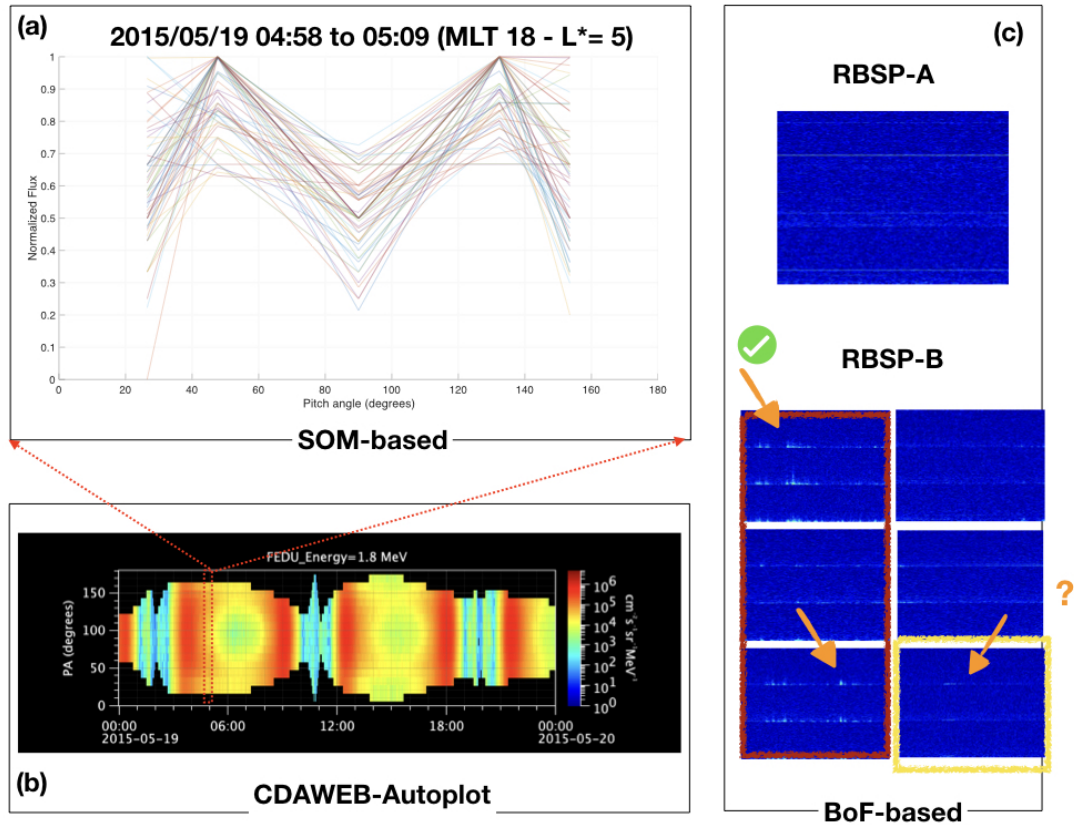
(a) SOM-based classification shown the persistent unusual butterfly PAD shape on May 19, 2015 after 04:58 UT. Van Allen Probe A was between MLT 18 and L-star $\sim$ 5.(b) The relativistic electron at 1.8 MeV channel shown the pitch angle distribution during one day.(c) Bof technique classified 7 (1 by RBSP-A and 6 by RBSP-B) images as EMIC classes. One image (yellow box) shown one region in which the contrast with the background color suggested some wave activities. Three images (red box) presented EMIC-like wave signature (orange arrow).

SOURCE: Author production.

Figure A.20 - Event 20 - August 16, 2015
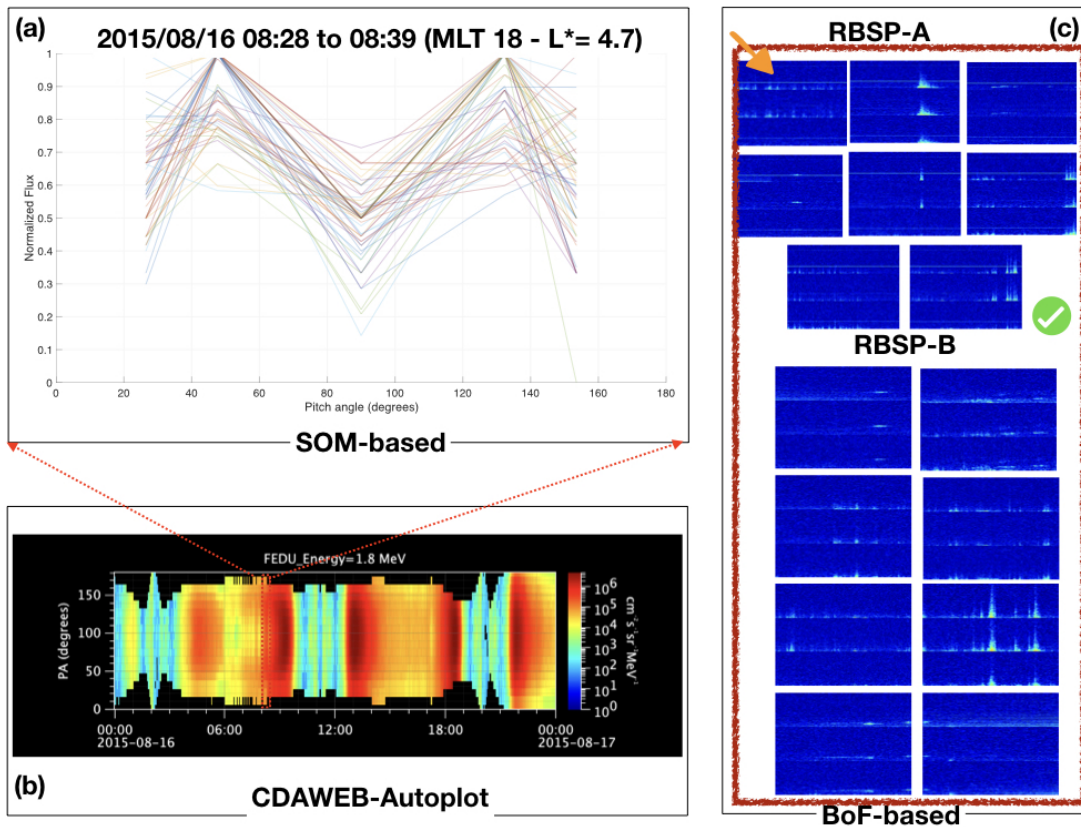
(a) SOM-based classification shown the persistent unusual butterfly PAD shape on August 16, 2015 after 08:28 UT. Van Allen Probe A was in MLT 18 and L-star $\sim$ 4.7.(b) The relativistic electron at 1.8 MeV channel shown the pitch angle distribution during one day.(c) Bof technique classified 16 (8 by RBSP-A and 8 by RBSP-B) images as EMIC classes. All of them (red box) presented EMIC-like wave signature (orange arrow).

SOURCE: Author production.

Figure A.21 - Event 21 - August 19, 2015
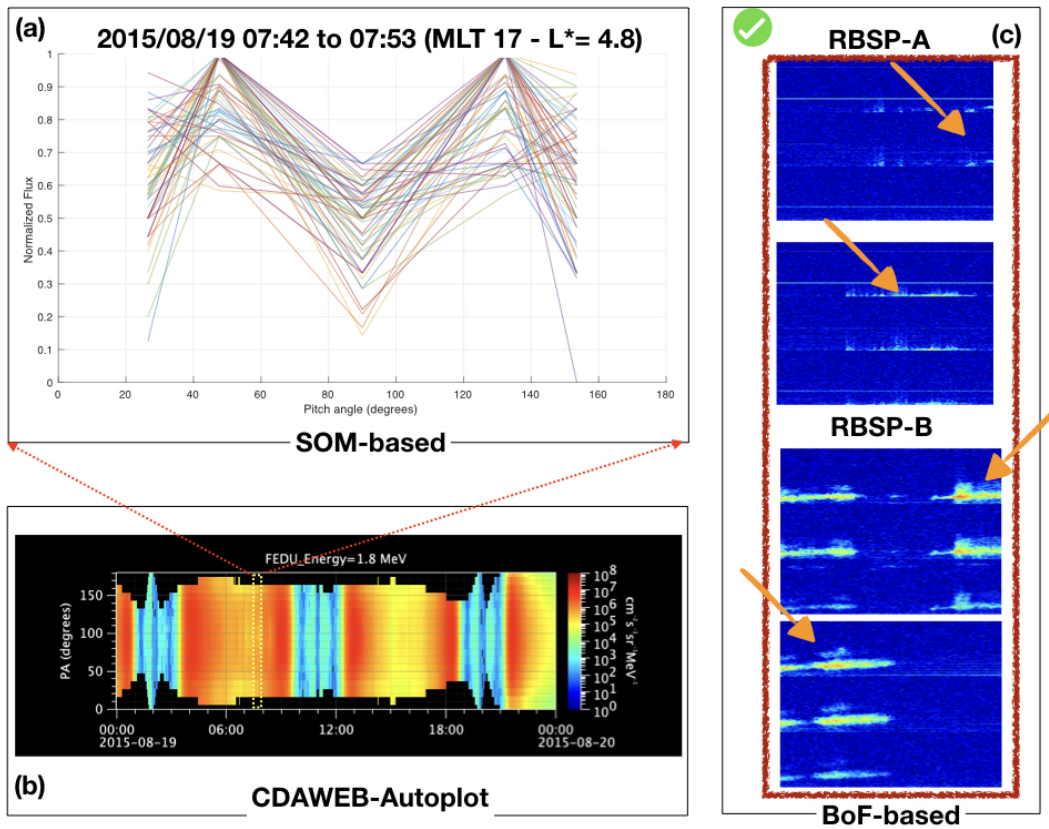
(a) SOM-based classification shown the persistent unusual butterfly PAD shape on August 19, 2015 after 07:42 UT. Van Allen Probe A was between MLT 17 and L-star $\sim$ 4.8.(b) The relativistic electron at 1.8 MeV channel shown the pitch angle distribution during one day.(c) Bof technique classified 4 (2 by RBSP-A and 2 by RBSP-B) images as EMIC classes. All of them (red box) presented EMIC-like wave signature (orange arrow).

SOURCE: Author production.

PUBLICAÇÕES TÉCNICO-CIENTÍFICAS EDITADAS PELO INPE

Teses e Dissertações (TDI)

Teses e Dissertações apresentadas nos Cursos de Pós-Graduação do INPE.

Notas Técnico-Científicas (NTC)

Incluem resultados preliminares de pesquisa, descrição de equipamentos, descrição e ou documentação de programas de computador, descrição de sistemas e experimentos, apresentação de testes, dados, atlas, e documentação de projetos de engenharia.

Propostas e Relatórios de Projetos (PRP)

São propostas de projetos técnico-científicos e relatórios de acompanhamento de projetos, atividades e convênios.

Publicações Seriadas

São os seriados técnico-científicos: boletins, periódicos, anuários e anais de eventos (simpósios e congressos). Constam destas publicações o Internacional Standard Serial Number (ISSN), que é um código único e definitivo para identificação de títulos de seriados.

Pré-publicações (PRE)

Todos os artigos publicados em periódicos, anais e como capítulos de livros.

Manuais Técnicos (MAN)

São publicações de caráter técnico que incluem normas, procedimentos, instruções e orientações.

Relatórios de Pesquisa (RPQ)

Reportam resultados ou progressos de pesquisas tanto de natureza técnica quanto científica, cujo nível seja compatível com o de uma publicação em periódico nacional ou internacional.

Publicações Didáticas (PUD)

Incluem apostilas, notas de aula e manuais didáticos.

Programas de Computador (PDC)

São a seqüência de instruções ou códigos, expressos em uma linguagem de programação compilada ou interpretada, a ser executada por um computador para alcançar um determinado objetivo. Aceitam-se tanto programas fonte quanto os executáveis.